UNIVERSITÀ DEGLI STUDI
DI NAPOLI FEDERICO II

Dipartimento di Scienze Chimiche

Ph.D. Thesis in Chemical Sciences

Theoretical study of time resolved spectroscopy and non-equilibrium processes

Supervisor Prof.
Nadia Rega

Ph.D. Candidate
Alessio Petrone

Accademic Year 2013/2014

Abstract

We developed new theoretical models and computational tools to explore the dynamical behavior of several systems, mostly in the biological field, undergoing non-equilibrium process or time-resolved spectroscopy.

We focused our attention on the cutting edge challenges of the modern theoretical and computational chemistry, without ever neglecting the experimental implications.

In fact, we can easily say that our challenges share the same attention in both the theoretical chemistry and the modern and newest experimental and technological applications, such as the newest time-resolved spectroscopies, the solar cell device design, innovative protein-based bio-sensors. The common, and in our opinion intriguing, factors of our work are the following: the molecular dynamics, the characterization of electronic excited states, and the modeling of complex events. Therefore, in each phase of the project we designed our theory and our computational experiments by studying our cases as a dynamic embedded system, surrounded by its environment, describing its excited electronic states and its temporal evolution. Moreover, the time dependence of our results provided an additional trigger to develop also new, or more accurate, tools of analysis. Three different case studies are presented, facing different experimental issues affecting different and shorter and shorter time scales.

First, the N-methyl-6-oxyquinolinium betaine time resolved Stokes-Shift experiment in water solution was investigated. Nowadays, thanks to the ultra-fast pulsed laser techniques, we are able to freeze the far-from-equilibrium structures during a molecular vibration or a reaction. We proposed a new computational protocol to study the excited state dynamics ruling the non equilibrium relaxation process affecting a fluorescent probe upon the electronic excitation. In this work, we explained how the whole time dependent signal is influenced in a dynamical way by several collective solvent motions.

After we presented several theoretical tools to characterize the behavior of transient excited states within bio-macromolecules. In particular we focused our efforts to study the excited state photo-reactivity and the optical behavior of the Green Fluorescent Protein (GFP). We calculate at the same level of TD-DFT the vertical excitation energy of the anionic GFP chromophore in the protein and in ethanol, dioxane, methanol and water solutions. As result, we reproduced for the first time the experimental trend of the absorption peaks with 0.015 eV as standard deviation of the accuracy. During this work, we also contributed to the tangled debate on the

gas-phase GFP chromophore experimental reference absorption value. Moreover, the Excited State Proton Transfer in the GFP is a complex and fascinating event of a paramount importance in many scientific and technological fields. Therefore, we also proposed an innovative computational protocol to face the simulation of a complex non-equilibrium process, such as the photo-reactivity affecting the GFP, going from easier to more accurate modeling approaches, along with showing the nature of the mechanism and the complex role of the protein matrix on it.

Finally, we explored the exciton dynamics of bulk hetero-junction (BHJ) based polymer solar cells. Therefore, we exploited a computational method that provides the explicit evolution of the electronic density along the time after the photon absorption, on sub-femto time scale. The innovative real-time non-adiabatic non-perturbative TDDFT electronic dynamics was used to better understand the interplay between the photo-excited electron-hole pair and the charge separated state. This work gave us an useful molecular insight for BHJ based polymer solar cell design, showing the crucial role of theoretical chemistry to investigate how small modifications on molecular scale can influence the properties of the whole device.

Contents

Introduction

The main aim of a Ph.D thesis should be to show in a clear and coherent way the project developed by the the Ph.D. candidate and the scientific framework in which she/he worked in. Therefore, in this thesis we tried to describe, in a thorough fashion, how during this Ph.D. program we developed several theoretical models and implemented new computational tools to explore the dynamical behavior of several system, mostly in the biological field.

In recent years chemistry started to observe phenomena on shorter and shorter time scales, and so at higher time resolution. For example, we are now able to monitor the collective atom motions on the picosecond time scale, or to observe the photoinduced-reactivity evolution in femtoseconds. Surprisingly, the attosecond timescale also has been achieved, giving the chance to look at effective electronic motions for the first time. Therefore, we focused our attention on the cutting edge challenges of the modern theoretical and computational chemistry, without ever neglecting the experimental implications. In fact, we can easily say that our challenges get the same attention in both theoretical chemistry and modern experimental and technological applications, such as the newest time-resolved spectroscopies, or the design of solar cell devices, and new protein-based bio-sensors. This community of

interest is not surprising, because the innovative fields in chemistry need an high effort from theoretical and computational research in order to interpret the brand new experimental results, to develop new devices or bio-sensors, fields still lacking of straightforward rational models. Moreover, beside this fundamental role of theory, always more frequently, theoretical chemistry has started to provide ideas to experimental chemists, engineers, start-up.

The common, and in our opinion intriguing, factors of our work were the following: the dynamics, the characterization of electronic excited states, and the modeling of complex events. So in each moment of our project, we designed our theory and our computational experiments by studying our cases as a dynamic embedded system, surrounded by its environment, describing its excited electronic states and its temporal evolution. Moreover, the time dependence of our results provided an additional trigger to develop also new, or more accurate, tools of analysis.

The following thesis was organized by dividing our work according the studied system and showing in each chapter the research interests, our results and the theoretical and computational methods developed.

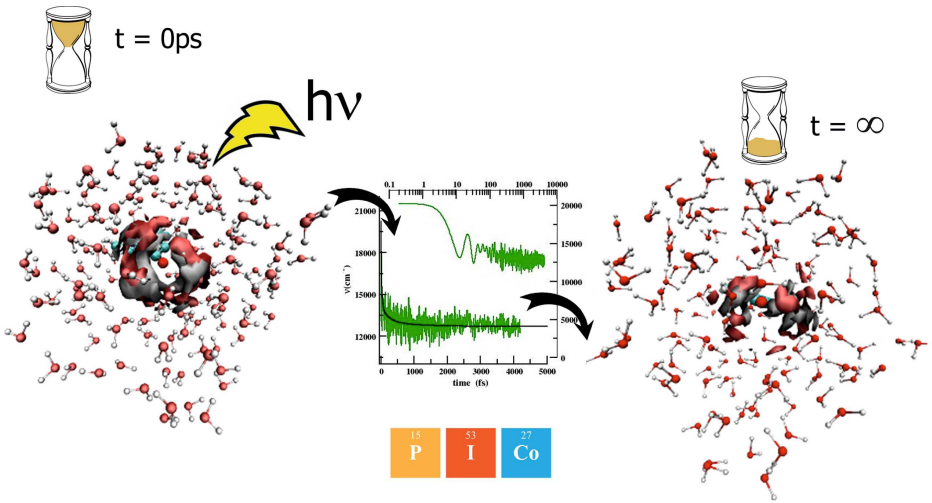

Fig. 1: *N*-methyl-6-oxyquinolinium betaine Stoke shift dynamics case study summary. A pictorial representation of the simulated experiments and results are shown.

In the first chapter the N-methyl-6-oxyquinolinium betaine time resolved Stokes-Shift experiment in water solution [1] was investigated on picosecond time scale (see figure 1 for a graphical summary). Nowadays, thanks to the ultra-fast pulsed laser techniques, we are able to *freeze* the far-from-equilibrium structures during a molecular vibration or a reaction. Therefore we have the possibility to observe several snapshots of a chemical reaction and the solvent re-organization on the time scale of both nuclear and electronic motions. [2] Moreover, advances in the molecular design and bio-sensor applications encouraged the employment of *ad hoc* modeled molecules to probe peculiar properties of the environment. Hence, the development of ultra-short laser pulses gave us also the possibility to study the dynamic process dealing with these probe molecules. The time resolved fluorescence is the experimental technique of choice for these aims and therefore it has received many attentions in these years, also because it is extensively used to investigate charge transfer phenomena and photo re-activity. In recent years, these issues also received attentions by theoretical chemists. In this new scientific area the theoretical-computational approach is essential to enforce new models for the analysis of experimental data. Relating the spectroscopic behavior to the atoms re-organization in a far-from-equilibrium system becomes one of the principal aims of the modern theoretical chemistry. Interest in the molecular motions associated with those photo-chemical phenomena in solution drove the development of the solvation dynamics studies.

Most features underlying solvation dynamics of neat liquids were discovered by ultra-fast spectroscopy and modeled by continuum and microscopic theories. [3–

14] This knowledge is now the foundation for understanding important processes in more complex systems, such as photo-reactivity in liquids and solvent dynamics at the surface of bio- and macro-molecules (micelles, surfaces, DNA, proteins). [15–17]

We proposed a new computational protocol to study the excited state dynamics ruling the non equilibrium relaxation process affecting a fluorescent probe upon the electronic excitation. The linear response (LR) time dependent density functional theory (TD-DFT) provided us the forces ruling the ab initio molecular dynamics. The explicit and implicit solvation effects on this process were also explored by employing the most accurate models that range from the QM\MM partition schemes, thanks to the our own n-layered integrated molecular orbital and molecular mechanics (ONIOM) [18–21], to the non-Periodic Boundary Conditions, to the General Liquid Optimized Boundary (GLOB) model [22–24]. Moreover, we also provided a post processing tools for molecular dynamics analysis proposing many collective solute-solvent structural relaxing functions, and an innovative multi resolution time series analysis based on Wavelet Transform (WT) of these quantities. [25; 26] This analysis allowed us to explain how the whole time dependent fluorescence signal is influenced in a dynamical way by several collective motions of the solvent. Therefore, our protocol proved to be useful for disentangling the dynamical features of these molecular dyes. Therefore, we provided a modeling scheme for time resolved fluorescence experiments and for the solvation dynamics affecting the molecular dyes in water solution. This translation of the time resolved spectroscopic signal in terms of molecular motions is precious and very promising in many innovative applications,

e.g. for the probe design in biochemistry.

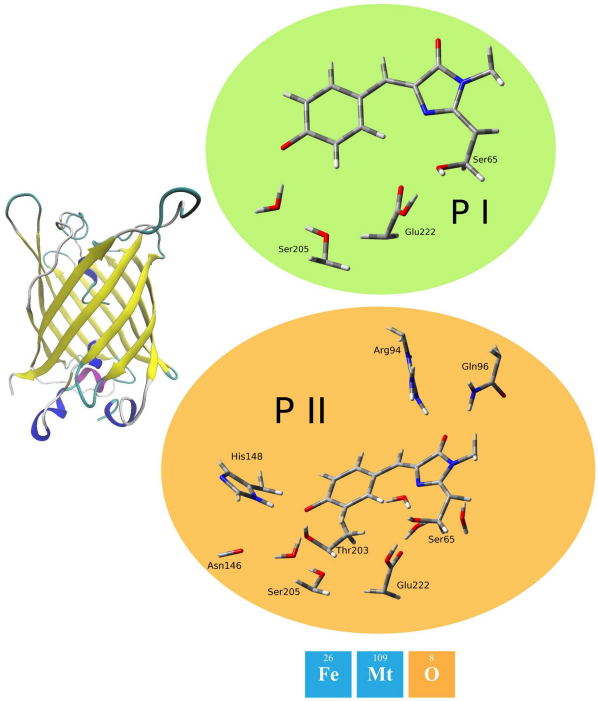

Fig. 2: The green fluorescent protein spectroscopy and excited state proton transfer case study summary. A pictorial representation of the simulated experiments and results is shown.

In the second chapter we performed several theoretical tools for characterizing the behavior of transient excited states within bio-macromolecules. In particular we focused our efforts to study the excited state photo-reactivity and the optical behavior of the Green Fluorescent Protein (GFP) on femtosecond time scale (see figure 2 for a graphical summary). In spite of the large number of experimental and theoretical studies [27–33], the optical absorption trend of the GFP chromophore in several environments was not understood. We calculated at the same level of TD-DFT the vertical excitation energy of the anionic GFP chromophore in the protein and in ethanol, dioxane, methanol and water solutions. As result, we reproduced for the first time the experimental trend of the absorption peaks with 0.015 eV as standard deviation of the accuracy [34]. During this work, we also contributed to the tangled debate on the gas-phase $HBDI^-$ experimental reference absorption value. Moreover, the Excited State Proton Transfer (ESPT) in the GFP is a complex and fascinating event of a paramount importance in many scientific and technological fields. As matter of fact, the proton shuttle triggered by the electronic excitation is the preliminary process leading to the fluorescent state of the protein, widely exploited for bio-imaging techniques in vivo and as genetic marker in cellular biology.[35] Thanks to the employment of the Intrinsic Reaction Coordinate methods [36], we investigated the proton transfer affecting the proton wire along the reaction pathway in both the ground and the excited electronic states, and we revealed that the movement of the protons is attributable to a concerted\synchronous mechanism. All protons move simultaneously with a single energy barrier governing

the kinetics. As matter of fact, in previous studies of Wang and coworkers [37; 38] the mechanism did not present a single barrier. The single barrier process in excited state was already mentioned in high level post Hartree-Fock study of Vendrell et al. [39], but they found a different pathway in the ground state, probably because of their planar constrained geometry in their model compound. We also proposed an innovative computational protocol, based on several TDDFT ab initio excited state dynamics, that proved that the excited state proton transfer mechanism is strongly influenced by the protein environment. The complex interplay between the new excited state potential curvature affecting the chromophore in the excited state and the steric constraint provided by the protein pocket were proved to be crucial to explain the ESPT affecting the chromophore in protein, and at same time could shed light on the competitiveness between the fluorescence and the non radiative pathway in the other environments. Therefore our efforts tested the reliability of the theoretical chemistry in the modeling the equilibrium spectroscopy behavior, analyzing the environmental effects on the optical properties of a complex system. Moreover, we faced the simulation of a complex non-equilibrium process, such as the photo-reactivity affecting the GFP, going from easier to more accurate models, showing the nature of the mechanism and the complex role of the protein matrix on it.

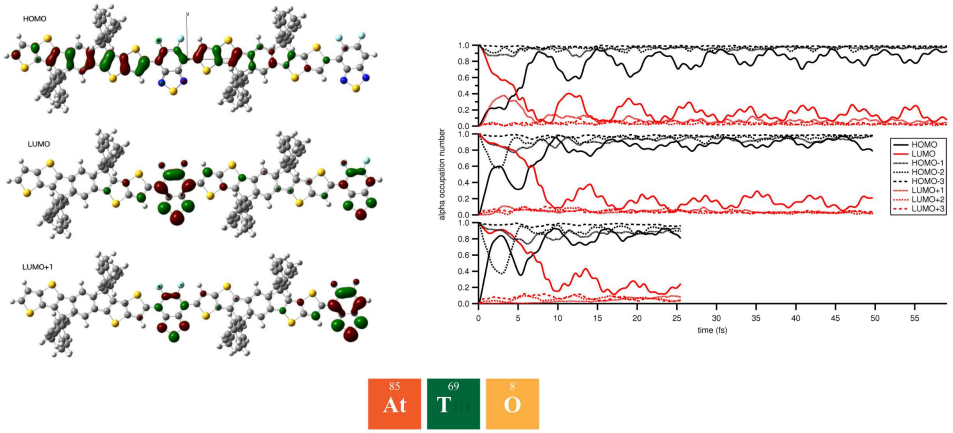

Fig. 3: The exciton dynamics of BHJ based polymer solar cells case study summary. A pictorial representation of the simulated experiments and results is shown.

In the third chapter we explored the exciton dynamics of bulk hetero-junction (BHJ) based polymer solar cells on attosecond time scale (see figure 3 for a graphical summary). In these devices, the conjugated polymers are blended with fullerene derivatives and are very promising for realizing the goal of achieving low-cost and scalable renewable energy [40; 41]. In particular, power conversion efficiency of 8-9 % in a single junction device has been demonstrated [42; 43].

We were interested in the exciton dynamics affecting the indiacenodithieno[3,2-b]thienophene-based solar cell devices and how the dynamics, in turn, was influenced by the incorporation of a π-bridge between the donor and acceptor units. Therefore, we exploited a computational method that provided the explicit evolution of the electronic density along the time after the photon absorption, on sub-femto time scale. The use of real-time (RT) non-adiabatic non-perturbative TDDFT electronic dynamics was been demonstrated useful to a better understanding of the interplay between the photoexcited electron-hole pair and the charge separated state[44; 45]. We used this invaluable and innovative theoretical method to follow the time evolution of the exciton dynamics affecting the first bright singlet electronic excited state of several dimer models of indiacenodithieno[3,2-b]thienophene-based polymer, which is mostly responsible for the absorption band of these materials in the visible range. Therefore, we provided an explicit inspection of the electronic density dynamics and observed how the different π-bridge structure could influence many factors: the molecular scaffold, the molecular orbitals involved in the dynamics, the charge migration upon the excitation which influences, on turn, the different

time constant of the electron-hole migration. Moreover, this work gave us an useful molecular insight for BHJ based polymer solar cell design, showing the important role of theoretical chemistry to investigate how small modifications on molecular scale could influence the properties of the whole device.

Chapter 1

A theoretical protocol for time resolved fluorescence: The N-methyl-6-oxyquinolinium betaine time resolved Stokes-Shift in water solution

The details of motion and structure of the surrounding solvent molecules play a crucial role in the rates and mechanisms of chemical reactions. Theoretically one tries to understand how the solvent affects the properties of a solute, starting from how solvent fluctuations couple to the solute potential energy surface. [46] Those are general issues, but they become more challenging when processes in the excited states are involved. In this case the aim is to understand how the optical properties and the photo-reactivity are influenced by solute-solvent intermolecular forces, and by bulk solvent properties. More in general, the comprehension of photophysics and photochemistry on solvent can be considered a prototype of the influence of other interesting environments, like proteins, DNA, or polymeric matrices.

Central to this study is to understand the dynamical interaction between a solute

and the surrounding solvent molecules, introducing a general computational protocol to simulate the solvent dynamics involving non-equilibrium processes in excited state potential energy surfaces (PES). Hence we have developed an integrated theoretical approach to study the time evolution of solute-solvent interactions, and, more in particular, a protocol to simulate and analyze the time-resolved emission spectroscopy of a solvatochromic dye.

Experimentally one usually monitors the time-evolution of the emission spectrum from a molecular probe (Stokes shift (SS) dynamics), i.e. the time dependent mean frequency $\nu(t)$ of the emission band. A key quantity is the normalized time dependent Stokes shift (TDSS) $S(t) = (\nu(t) - \nu(\infty))/(\nu(0) - \nu(\infty))$. If the Stokes shift originates mainly from solvent rearrangement, and the latter is ruled by a linear response, then the $S(t)$ function may be reconstructed from the solvent polarization $P(t)$. In continuum models $P(t)$ is expressed by the frequency-dependent dielectric permittivity $\epsilon(\omega)$, attainable from experiments or simulations of the pure liquid. In microscopic theories, molecularity is introduced by including a specific dependence of the polarization upon the solvent number density and particle-particle correlation functions, quantities which depend on both time and space. The development of several formalisms took advantage of results obtained from atomistic simulations, but these did not always provide accurate answers about many open issues, since important effects (e.g. the electronic polarization) are missing from the classical energy potentials adopted to perform the molecular dynamics (MD). This is particularly true for the sub-picosecond part of the relaxation, difficult to obtain experimentally.

It is generally acknowledged that high-frequency collective modes of the solvent dominate the relaxation process at short times. [47] Much less is known about the role played by a change of specific solute-solvent interactions, for example when the number of solvation sites changes upon electronic excitation. [48–51] An analysis of such a case at molecular level would be important, to shed light on the capability of the dye to probe its environment. Most of experimental and theoretical procedures introduced so far interpret the $S(t)$ decay signal by adopting ad hoc fitting procedures, without a direct molecular interpretation. Beside the usual multi exponential fitting procedure can provide only an indirect evidence of molecular motion involved in the process, thanks to the general knowledge of characteristic solvent motion times (i.e. librations, collective hydrogen bond stretching, etc.).

We proposed an innovative theoretical protocol to perform excited state non equilibrium simulations in order to reproduce and analyze the decay processes peculiar of the time resolved spectroscopy techniques. In particular, we have analyzed the aqueous solvent relaxation following $S_1 \leftarrow S_0$ excitation of *N*-methyl-6-oxyquinolinium betaine (MQ, see Figure 1.1(a)), a solvatochromic dye. Our protocol can be summarized in the following ingredients: (a) the sampling procedure of equilibrium properties, (b) an ad hoc selection criteria for choosing a Boltzmann packet of trajectories, (c) the simulation of an excited state non equilibrium relaxing process at finite temperature, (d) an accurate multi-level computational approach to include at an ab initio level all the main contributions influencing the dynamics. Moreover, we developed also new post processing tools for MD analysis proposing: (e) many collective

solute-solvent structural relaxing functions and (f) an innovative multi resolution time series analysis based on Wavelet Transform (WT) of this quantities. [25; 26]

Therefore the several contributions affecting the whole Stokes shift evolution of the MQ molecule have been analyzed for the first time extensively on a molecular scale, relying on the accuracy of our non equilibrium trajectory simulation protocol. For what regarding the multi resolution frequency analysis the Wavelet theory provides an unified framework for a number of techniques which have been developed independently for various applications on signal processing, [52] but we proposed for the first time its application on non equilibrium time resolved spectroscopy. The wavelet transform allows for the localization of a signal both in time and frequency domain [53], and this feature is particularly appealing for the simulation of time-resolved spectroscopies [54].

In fact, our main goal is to retain the temporal informations of molecular features involved in time resolved spectroscopy, provided by our protocol for non equilibrium excited state molecular dynamics simulations. To do this aim the wavelet transform of the whole simulated signal and of ad hoc collective solute-solvent structural relaxing functions appeared essential.

This MQ system is very interesting because it includes and enhances all the main characteristic of molecular fluorescent dyes, in spite of peculiar solvation properties of the MQ chromophore. Because of the zwitterionic arrangement of the electronic density in the ground state, we calculate that the microsolvation around the MQ oxygen is similar to that of an anion, with about 3.5 as coordination number. After

excitation this situation is reversed and evolves toward the microsolvation of a carbonyl group (coordination number 1.9) with a net loss of 1.5 water molecules from the first solvation shell. Thus strong change of specific interactions accompanies the solvation dynamics and the evolution of the Stokes shift. On the other hand the relaxation process, as shown by stimulated emission experiments in water, can be well reproduced by a simple continuum model together with the $\epsilon(\omega)$ function from other spectroscopic methods. [1] Moreover this system proved to be very promising as a probe of solvent modes in a mixed water-trehalose solution. [55]

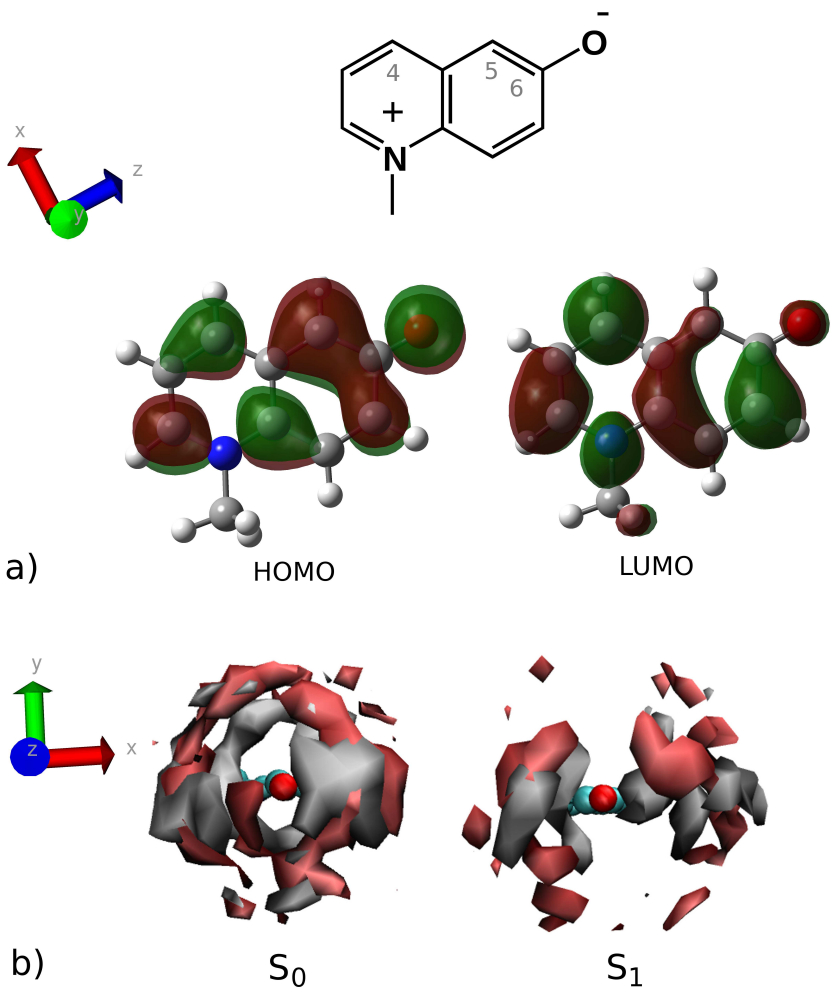

Fig. 1.1: a) *N*-methyl-6-oxyquinolinium betaine (MQ) structural formula and HOMO and LUMO isodensity surfaces calculated at the B3LYP\6-31(d,p) level of theory; b) Spatial distribution functions of water oxygen (red) and hydrogen atoms (gray) belonging to the first solvation shell of the MQ oxygen. The view is directed onto the OC bond. Analysis refers to both the ADMP\GLOB (ground S_0 state, left) and the BOMD\GLOB (excited S_1 state, right) simulations.

1.1 Methods

From the literature regarding time-dependent approaches to simulate spectroscopic signals, more specifically absorption cross sections, we learn that classical simulation at finite temperature are capable to reproduce optical absorption band shapes, although they are not capable, by nature, to account for the fine details of transition between vibronic states. More specifically, the absorption cross section can be obtained by the following informations: 1) a configurational distribution well-representative of the ground state equilibrium of the chromophore under study and 2) corresponding values of the vertical electronic transition energies. Therefore, properly simulating the chromophore in solution at finite temperature in the ground state, and then calculating excitation energies on a rightly chosen number of extracted frames, gives us the way to simulate steady state absorption bands. Following this *classical mechanics* representation of spectroscopical events also for time-resolved signals, we can imagine the time-resolved emission spectrum accounted for by the instantaneous excitation of such ground state representative configurational distribution, and by the subsequent evolution on the excited state potential energy surfaces toward the new equilibrium. Therefore, emission energies of this sample, calculated along the time, bring us a decay signal $S(t)$ which has the TDSS as experimental counterpart. It is worth of noting that the steady state absorption band peak represents the *time zero* of the TDSS simulation, at variance of what happens experimentally, when the time zero depends upon the instrumental resolution. In practise, we operate as follows: first of all we sampled the ground state

PES, throughout a ground state MD. This was important to obtain both the main structural and spectroscopic properties regarding the ground state and to select the starting phase space points for the following non-equilibrium relaxation MD. The starting configurations were chosen in order to reproduce accurately the energetic broadening of the first absorption band, corresponding to the time zero $S_1 \leftarrow S_0$ excitation, responsible of bright MQ fluorescence. We obtained a collection of 24 starting phase space points, and subsequently excited state MDs, that well reproduce the Boltzmann distribution for the whole (or a representative part) ground state PES at room temperature. It is witnessed by the computed vertical excitation energies, structural parameters and momenta distributions of these points that reproduced both the average and the variances of the whole S_0 simulations (see Section 1.3 for a detailed analysis of starting points and the average ground state properties).

1.1.1 Stokes shift dynamics

First, we characterized the equilibrium of the ground (S_0) and the first singlet excited (S_1) states of MQ in aqueous solution by performing atom-centered density matrix propagation (ADMP) [56; 57] and Born-Oppenheimer [58; 59] molecular dynamics (BOMD), respectively.

We refer to the Section 1.3 for the computational details, trajectories on the S_0 and S_1 potential energy surfaces were collected for 15 ps and 7 ps, respectively, after 4 ps of equilibration, with a time step of 0.2 fs.

The MQ\water relaxation dynamics, along with the corresponding evolution of

the $S_1 \rightarrow S_0$ transition energy, was followed for about 4 ps. The MQ Stokes shift dynamics in water was reconstructed by following several trajectories of ab-initio molecular dynamics ruled by S_1 potential energy surface. We choose 24 points from the phase space sampled during the S_0 MD in order to represent the MQ-water system at the starting time of the Stokes shift dynamics, each sampling the relaxation process from a possible Franck Condon nuclear configuration caught up with the electronic excitation. Those starting points were picked up at random, except for the criterium according to which the average and the distribution of the transition energies $\Delta E_{S_1 \leftarrow S_0}$ are very close to the steady state $S_1 \leftarrow S_0$ absorption peak and band width, respectively. Similarly, we ensured that the 24 points nuclear kinetic energies E_{kin} reproduced the S_0 average total linear momentum. (see the the Section 1.3 for a further discussion)

The simulated TDSS, $S(t)$, was computed by averaging the vertical transition energy evaluated on fly for the 24 trajectories:

$$S(t) = \frac{< \nu(t) > - < \nu(\infty) >}{< \nu(0) > - < \nu(\infty) >} \tag{1.1}$$

where at each time step the corresponding S_1 ensemble average $< \nu(t) >$ is the average vertical $\Delta E_{S_1 \leftarrow S_0}$ excitation energy, weighted by the corresponding oscillator strength.

1.1.2 Structural relaxation functions

The time evolution of the microsolvation layout was analyzed. Several structural $C(t)$ relaxation functions have been computed and analyzed:

$$C(t) = \frac{< f(t) > - < f(\infty) >}{< f(0) > - < f(\infty) >}. \tag{1.2}$$

where at each time step the corresponding S_1 ensemble average of the $f(t)$ parameter is evaluated on the 24 excited state trajectories. We analyzed three $f(t)$ parameters representing the structural layout of the MQ first solvation shell. To better characterize the strength and structural features of the hydrogen bond we compute several first shell rearrangement functions. The average number of water hydrogen atoms within 2.7 Å from the MQ oxygen, $f_w(t)$. The average number of hydrogen bonds involving the MQ oxygen $f_{HB}(t)$, this latter calculated with thresholds of 2.7 Å, 3.5 Å and 30° for the O···H distance, the O···O distance and the H-O···O angle, respectively. To better characterize the fast component of first shell hydrogen bond relaxation dynamics, an angular function $f_\theta(t)$ can be calculated by adopting the following expression [60]:

$$f(\theta(t)) = \begin{cases} exp(-(\theta_{S_0eq} - \theta(t))^2/2\sigma_\theta^2, & \text{if } (\theta_{S_0eq} - \theta(t)) < 0 \\ 1, & \text{if } (\theta_{S_0eq} - \theta(t)) \geq 0 \end{cases}. \tag{1.3}$$

Where θ is the before mentioned directional water H-O···O MQ angle, and the value θ_{S_0eq} and σ_θ are extrapolated from the S_0 MQ angular distribution function: θ_{S_0eq} is the angle associated with the first local maximum and σ_θ is its half-width at half-maximum (see Section 1.3). We choose only the first shell water molecules for this last function by analysing the θ values of water molecules within 3.6 Å O···O

distance. The $C_{HB}(t)$, $C_w(t)$ and $C_\theta(t)$ relaxation curves describe the rearrangement of the first solvation shell following the electronic excitation.

1.1.3 Wavelet analysis

In the wavelet analysis the decomposition of the signal is carried out by means of a special function ψ called wavelet mother, localized in time by a translation parameter. Furthermore ψ can be *dilated* or *contracted* by using a scale parameter, a, in order to focus on a given range of oscillations [61]. The wavelets derived from the same mother constitute a family. They represent translated and scaled versions of ψ, obtained by changing the a and b parameters of the mother prototype.

Our analyses have been performed using the *continuous* wavelet transform (WT), which is the appropriate one for our time series analysis [52; 53; 62]. The mathematical expression for the continuous wavelet transform simply replaces the Fourier basis function with a wavelet one:

$$W(a,b) = \int C(t)\psi_{a,b}(t)dt \tag{1.4}$$

where the wavelet function $\psi_{a,b}(t)$ is defined by dilation and translation of the mother wavelet $\psi(t)$ expressed as

$$\psi_{a,b}(t) = |a|^{-\frac{1}{2}}\psi\left(\frac{t\text{-}b}{a}\right)(a,b \in R; a \neq 0) \tag{1.5}$$

where a is the scale (dilation) proportional to the inverse of frequency and b represents the translation (time localization). By changing the wavelet scale and

translation parameters, it is possible to analyze the spectrogram evolution during the time. In particular the frequency is localized in time by changing the b parameter, while the contributions of different frequencies are analysed by changing the a parameter that stretches the time window.

We choose to work with the Morlet wavelet, a plane wave modulated by a Gaussian-type function. The choice has been based on preliminary tests, and it is the most used in chemical applications [54; 63–65]. The Morlet wavelet can be expressed as

$$\psi(t) = \pi^{-1/4} e^{i\omega_0 t} e^{-t^2/2} \tag{1.6}$$

where ω_0 is the non dimensional frequency, whose value is usually set to be ≥ 6 to satisfy the so called admissibility condition [26]. Larger ω_0 values allow for a good frequency resolution at the cost of poor time resolution [63]. To reduce the computational time required to calculate the wavelet transforms, the Equation 1.4 has been solved in the reciprocal space [53].

A correspondence between wavelength and the scale a can be achieved. For a Morlet wavelet with $\omega_0 = 6$, the relation is $\lambda = 1.03a$ where λ is Fourier wavelength, indicating that the scale is almost equal to the Fourier frequency [66].

Because the wavelet function $\psi(t)$ is in general complex, the wavelet transform $W(a,b)$ is also complex. Therefore we report the so called *wavelet power spectra* every 5 fs by plotting the $|W(\tilde{\nu}, t)|^2$, converting the scale factor in wavenumber. Regarding the present application for MQ in water solution, we analyzed the wavelet power

spectra of the time dependent Stokes shift, $S(t)$, and the three MQ micro-solvation structural relaxation functions, $C_{HB}(t)$, $C_w(t)$ and $C_\theta(t)$.

These spectra have been also decomposed in frequency ranges to disentangle the different molecular contribution affecting the whole time-frequency spectra. The slow component (20-75cm^{-1}), the bending (75-150 cm^{-1}) and stretching (150-400 cm^{-1}) of collective hydrogen bonds motions, the collective water libration motions (400-800 cm^{-1}) and the fast component (1000-2000 cm^{-1}) frequency ranges have been analyzed. For each range, the maximum $|W(\tilde{\nu},t)|^2$ value along the time has been extracted and fitted by exponential and gaussian functions to analyze characteristic relaxation times:

$$|W(\tilde{\nu},t)|^2_{Max} = \sum_i \beta_i e^{-(t/\tau_i)^{\alpha_i}} \tag{1.7}$$

In Equation 1.7 the exponent value (α) distinguishes between the exponential ($\alpha = 1$) and the gaussian ($\alpha = 2$) contribution, the β values represent the amplitudes, with relaxation times τ related to characteristic frequencies affecting the whole decay. [16; 17; 67] An identical fitting procedure has been performed on the experimental TDSS signal and the resulting experimental times have been analyzed and compared with the previous fitting procedure.

An ad hoc program to handle chemical stationary and non stationary signals has been designed by us to perform the wavelet analysis using the wavelet program built by Torrence and Compo [53] as a guide line.

1.2 Results

1.2.1 S_0 and S_1 microsolvation analysis

We characterized the ground (S_0) and the first singlet excited (S_1) states of MQ in aqueous solution by performing ADMP and BOMD, respectively.

The S_1 excited state does not show any significant multireference character, and is obtained from S_0 by a HOMO $\rightarrow$ LUMO single excitation. As can be seen from the frontier orbitals isodensity surfaces in Figure 1.1(a), the $S_1 \leftarrow S_0$ transition is characterized by substantial charge transfer from the MQ oxygen toward the quinolone ring and the nitrogen atom. From the microsolvation standpoint, the MQ-solvent interactions radically change upon excitation: in the ground state the oxygen site is able to engage specific solute-solvent interactions through the lone pair orbitals and the HOMO π lobe, while this latter interaction is precluded in the S_1 state. In other words, the carbonyl group behaves as an anion [68] when the molecule is in the ground state, and as a neutral group in the first excited state. This also accounts for the reverse solvatochromism of the molecule: the $S_1 \leftarrow S_0$ transition shifts to the blue when polarity is increased, since the HOMO is more stabilized by polar solvents compared to the LUMO. A blue shift of 0.67 eV was calculated when going from the gas-phase (isolated molecule) to aqueous solution.

In Figure 1.1(b) we plot the isovalue surfaces of the uncorrelated probabilities for water oxygen (red) and hydrogen (gray) atoms, obtained from analysis of the the ab-initio molecular dynamics performed in the two electronic states. These spatial distribution functions cover the region around the MQ oxygen and summarize the

most important features of MQ microsolvation. We observe a doughnut-shaped surface representing the water arrangement around the MQ oxygen in the ground state. Upon electronic excitation, the water spatial distribution reduces to two symmetrical lobes in the proximity of the oxygen lone pairs.

In order to analyze the solvent dynamics from a structural point of view, we first calculated the radial distribution functions (RDFs) involving the MQ oxygen and the water molecules in the S_0 and the S_1 state at equilibrium, respectively. From Figure 1.2 we see that the integration over the first peaks of the oxygen-oxygen RDFs corresponds to 3.6 and 2.2 solvent molecules in the S_0 and S_1 case, respectively. This implies a net loss of 1.4 water molecules in the MQ first solvation shell, as a consequence of the electronic excitation. From the analysis of the steady-state trajectories, the average number of hydrogen bonds is 3.1 and 1.9 for the S_0 and the S_1 state, respectively.

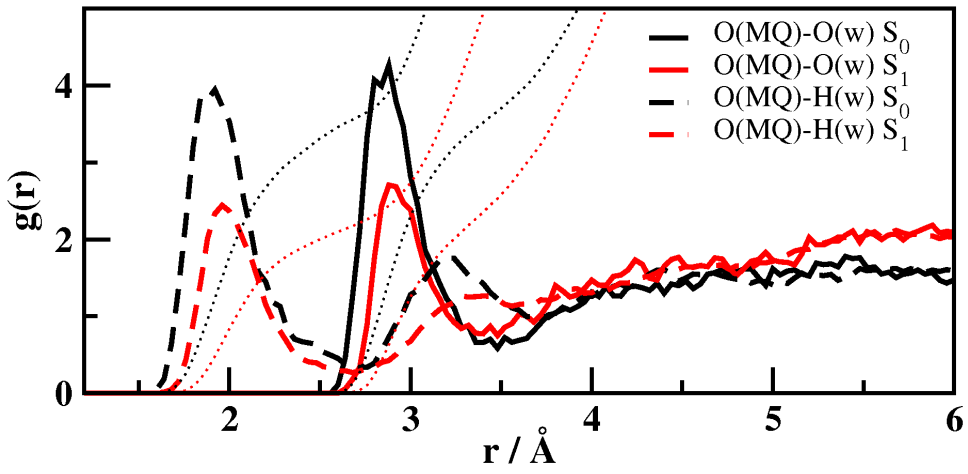

Fig. 1.2: RDF's of MQ in aqueous solution, calculated by analysis of the ADMP\GLOB and BOMD\GLOB trajectories in the ground (black) and the S_1 (red) excited state, respectively. The integration number of the distribution functions is also reported.

1.2.2 Stokes shift and micro-solvation dynamics

The relaxation of the MQ\water system, along with the corresponding evolution of the $S_1 \rightarrow S_0$ transition energy, was followed for about 4 ps. At each time step the emission energies provided by the 24 trajectories were weighted by the corresponding oscillator strength and averaged. The final result is the simulated TDSS, i.e. the emission peak ν(t) evolution toward the emission steady state.

The green line of Figure 1.3 represents the computed TDSS. We observe an ultrafast decay of the ν(t) curve in about 50 fs, with a first recursive event at about 12 fs, followed by large oscillations. These correspond to a strong rearrangement of the quinolone ring, no sensible change in the first solvation shell being recorded during the first 50 fs (see below). This part of the ultrafast relaxation could not be detected experimentally due to limited instrumental resolution. [1]

Important features of the dynamics are in very good agreement with the experiment [1]: a) the simulated full SS ($\nu(\infty)$-$\nu(0)\approx$ 7600 cm^{-1}) agrees with the experimental difference between the absorption and stimulated emission maxima ($\approx$ 7750 cm^{-1}); b) in spite of limited statistics, we observe also a decrease of the ν(t) oscillations by 2.5 ps when the experimental curve reaches a plateau, for an overall relaxation time (4 ps) that is also well reproduced.

The TDSS is empirically described as a superposition of exponential terms and a gaussian term. The experimental TDSS curve is described by a slower Debye relaxation processes [69] (with $\tau \approx 1$ ps), a broad resonance from collective hydrogen bond motion (at 171 cm^{-1} or 195 fs) and one from solvent librations (725 cm^{-1} or 49

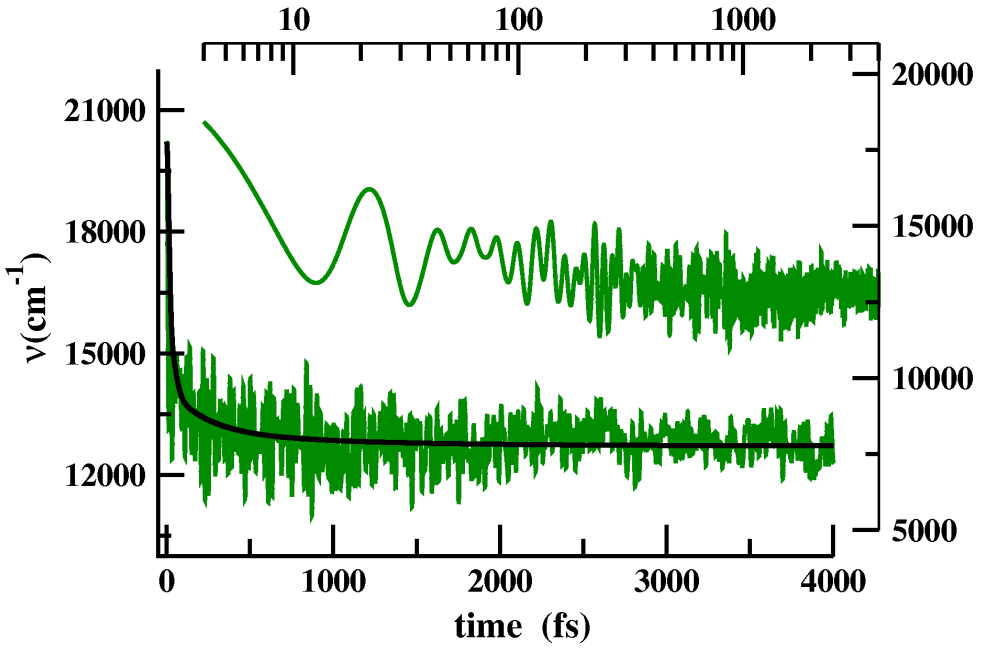

Fig. 1.3: Time-dependent emission peak frequency (cm^{-1}, green) of MQ in aqueous solution, from non-equilibrium BOMD\GLOB trajectories in the S_1 state. A representative curve (black) of stretched exponentials is also shown.

fs). While the former affects the whole decay, the libration contribution influences the process in the ultrafast part only (first 200 fs), and motion of the hydrogen bond network dominates the 200-1500 fs interval.

The simulated TDSS can be represented by the curve drawn in black solid line of Figure 1.3, obtained by the sum of exponential and gaussian time functions. From the comparison with the experiment it is clear that the ultrafast part can not be detected by the instrument (this latter can be fitted in the simulated TDSS by a gaussian contribution with τ=19 fs).

The time evolution of the microsolvation layout was analyzed at this point. Several structural relaxation functions have been computed and analyzed: the average

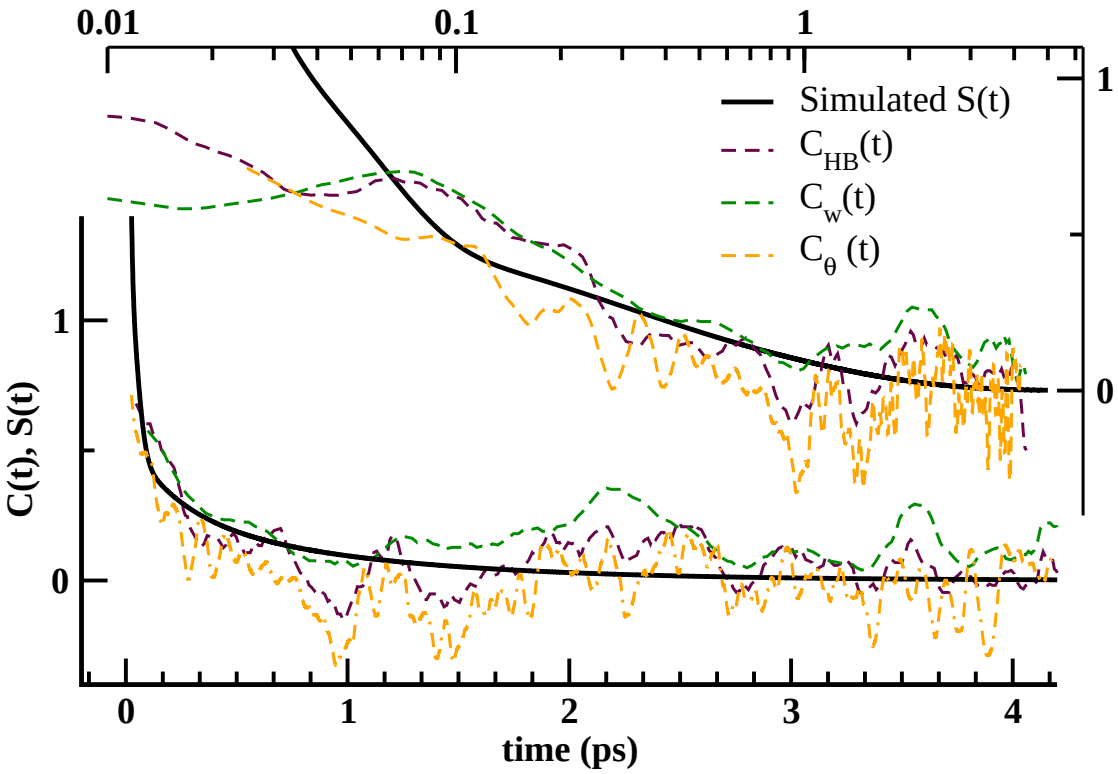

Fig. 1.4: Relaxation functions of MQ solvation dynamics obtained by analysis of non-equilibrium BOMD\GLOB trajectories in the S_1 state: number of water within the first solvation shell, $C_w(t)$ (broken green line), number of MQ\water hydrogen bonds, $C_{HB}(t)$ (broken maroon line), and water orientational relaxation function, $C_\theta(t)$ (broken orange line). The simulated representative curve of MQ TDSS, S(t), is also reported for comparison (black full line).

As most important finding of this work, the $C_i(t)$ and $S(t)$ functions show comparable progress in time. Apparently, the change of specific interactions between the chromophore and solvent molecules ($C_{HB}(t)$) and the first shell re-orientational process ($C_\theta(t)$), along with the migration of molecules from the solute toward the bulk ($C_w(t)$), are ruled by the same processes which are responsible for the collective rearrangement of the pure solvent ($S(t)$).

More in detail, we observe that first part of signal is ruled by the faster collective water libration motions ($C_\theta(t)$) between 100-220 fs. At about 220 fs the slope changes, and in the 220-1200 fs interval the relaxation is dominated by collective bending and stretching involving the hydrogen bond network, ($C_{HB}(t)$ and the $C_w(t)$). During this period we observe the most important rearrangement of the first solvation shell: first the orientational water molecules relax upon the MQ excitation ($C_\theta(t)$), so the number of hydrogen bonds undergoes a strong decrease ($C_{HB}(t)$), finally the total number within the first shell diminishes with a lower slope and with less broad oscillations ($C_w(t)$), resulting in an average trend more similar to the evolution of the experimental emission energy. This suggests that, during this time, the frequencies peculiar of hydrogen bond motion guide the change of hydrogen bonds to the MQ oxygen, while the most part of water molecules of the first shell remains in the solute proximity. At longer times (after $\sim$ 2ps), the curves are dominated by Debye-like relaxation, i.e. by contributions characterized by the longest relaxation time. During this period we observe large rearrangements of the first–shell water molecules, while the average number of hydrogen bonds adjusts with progressively

less broad oscillations, until about 2.5 ps, when small oscillations around the final value are observed. This is approximately the time when the experimental curve reaches a plateau, i.e. the process is almost completed.

1.2.3 Wavelet analysis

We obtained and analyzed the simulated TDSS, $S(t)$, and the three micro-solvation structural relaxation functions, $C(t)$, in terms of *wavelet power spectra* for a deeper molecular analysis of the collective water motion analyzed in the previous section.

The wavelet analysis of the TDSS has been performed in order to investigate in detail the contributions concerning the solvent dynamics affecting the whole signal decay.

A detailed knowledge of the dynamical evolution of the frequencies present in the signal is provided by the wavelet analysis, that allows for an exploration of the frequency contributions to $S(t)$. Such a spectrum is shown in Figure 1.5.

The temporal range is $0 - 3200$ fs, a time long enough for the $S(t)$ signal to reach a plateau and to reproduce the overall relaxation time. The plotted frequency range is $0 - 3000\ cm^{-1}$. This range has been chosen because higher frequency values did not show any significant band. Observing the band intensities, it is evident that the band centered around 1650 cm^{-1}, which is assigned to the C=O vibrational contribution to the relaxation signal, is the most intense at early times, dominating the ultra-fast relaxation (this contribution can not be registered in the experimental signal because of the temporal resolution). This band undergoes also a pronounced red-shift during the relaxation process (about $\sim 800 cm^{-1}$), as we can imagine after

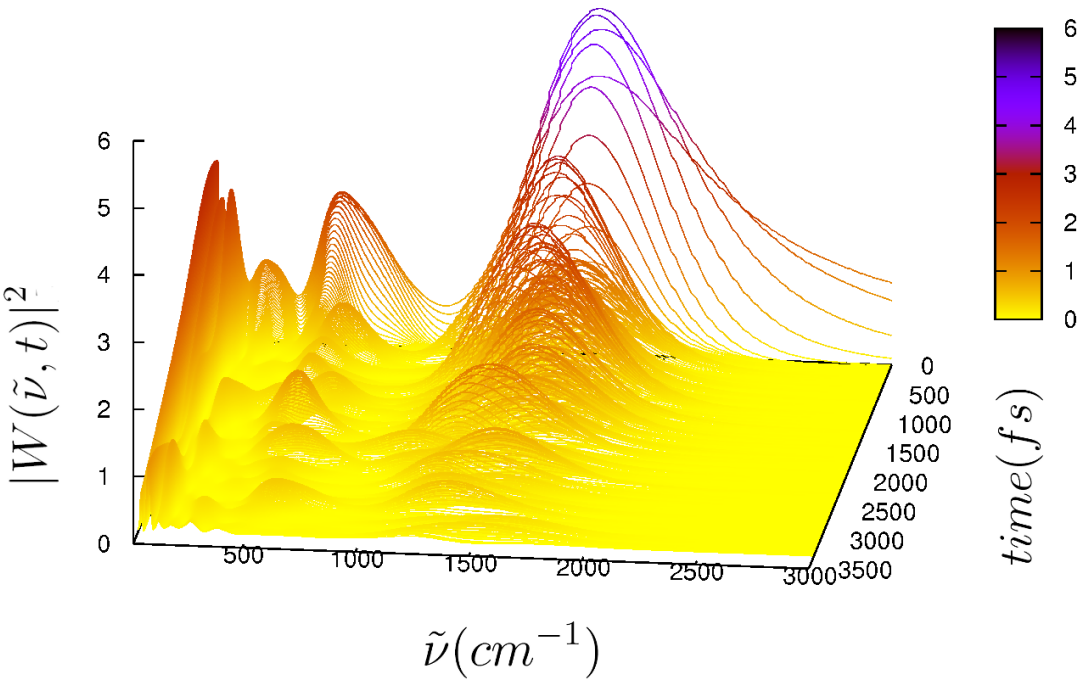

Fig. 1.5: The wavelet power spectra of the simulated MQ TDSS, S(t). The temporal range is reported in fs (x axis), the y axis represents the frequency (cm^{-1}), the z axis is the $|W(\tilde{\nu},t)|^2$ of the wavelet spectrum expressed in arbitrary units.

the C=O bond decreasing order upon the electronic excitation.

The overall $|W(\tilde{\nu},t)|^2$ decreases during the time, although it is possible to observe increasing intensities of some bands also in the middle of the spectrum, showing that the signal is dominated by different frequency contributions in a dynamical way. Beyond the most intense band at about 1650 cm^{-1} affecting the ultra-fast part of the signal, very interesting bands under 1000 cm^{-1}, due to collective solvent motions, appear in the wavelet spectrum. Many peaks are hardly separable making this range very difficult to analyze.

A separation of the spectrum in frequency ranges has been performed in order to define ranges in which the bands can be clearly defined. Frequency ranges were: 1)

$1000 - 2000\ cm^{-1}$, including the C=O stretching relaxation with a band centered, on average, at about 1650 cm^{-1}; 2) $400 - 800\ cm^{-1}$, including the libration modes of water, with band is peaked at about 590 cm^{-1}; 3) $150 - 400\ cm^{-1}$, including collective hydrogen bonds motions of stretching; 4) $75 - 150\ cm^{-1}$, including collective hydrogen bonds motions of bending; and 5) $20 - 75\ cm^{-1}$ including breathing modes of bulk water.

The temporal evolution of the maximum $|W(\tilde{\nu}, t)|^2_{Max}$ for each frequency range has been extracted and shown in Figure 1.7. From this figure we can see that the temporal evolution of the amplitude is very different in the several ranges. An oscillating evolution of the band associated with the frequency range $1000 - 2000\ cm^{-1}$ is found, moreover it shows a stiff decay in the ultra-fast part of the spectrum. Also the dynamical evolution of the band in the $400 - 800$ cm^{-1} range is characterized by an initial fast decay followed by slower oscillations. The relaxation of the remaining bands is slower, especially in the $20 - 75$ cm^{-1} range (line not shown). These relaxation functions have been fitted by exponential and gaussian terms in order to analyze the relaxation times of the characteristic frequencies. Fitting parameters are listed in Table 1.1. Relaxation times for individual processes are in good agreement with the previous interpretation of the experimental $S(t)$ signal and the wavelet spectrum allows for a detailed analysis. For example, relaxation of stretching and bending collective hydrogen bonds motions ($\tau = 101$ and 410 fs, respectively) corresponds to a unique experimental relaxation event with an average value of $\tau = 195$ fs. Most part of the decay regarding the solute (C=O stretching) is below the in-

Table 1.1: Exponential and gaussian fits of the maximum $|W(\tilde{\nu},t)|^2_{Max}$ TDSS, $S(t)$, wavelet power spectra temporal evolution in different frequency ranges. The relaxation times in fs and the correlation coefficients are also shown.

Frequency range (cm^{-1})	τ_0 (fs)(β(%))	τ_1 (fs)(β(%))	R
$1000-2000$	35.1 (74 %)	1481.6 (26 %)	0.78
$400-800$	94.8 (75 %)	1875.4 (25%)	0.89
$150-400$	100.9 (100 %)	/	0.80
$75-150$	409.5 (100 %)	/	0.95
$20-75$	1275.7 (100 %)	/	0.95

strumental resolution, confirming that the interpretation of the Stokes shift only in terms of the solvent reorganization is actually a well founded approximation. From inspection of Table 1.1 we also confirm that collective water librations show a simulated relaxation time overestimated with respect to the experimental fitting ($\tau = 95$ fs vs 46 fs). This apparent discrepancy is explained by the following wavelet analysis of the structural relaxation functions.

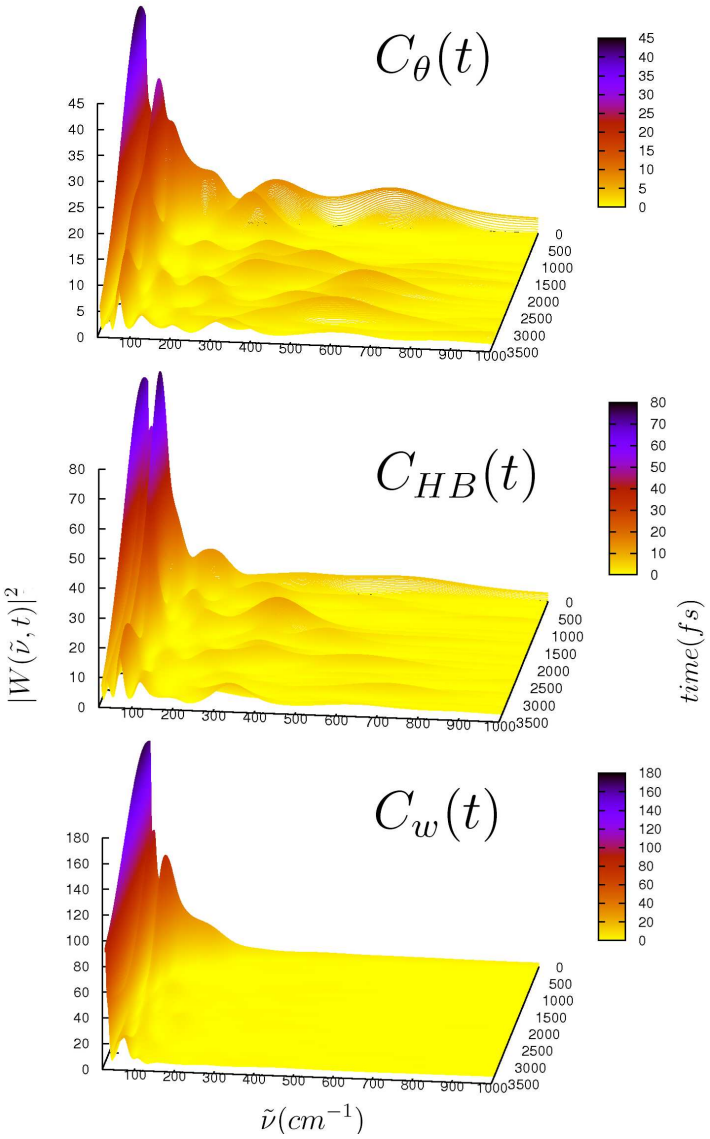

Fig. 1.6: The wavelet power spectra of MQ structural relaxation functions. The corresponding $C_{HB}(t)$, $C_w(t)$, $C_\theta(t)$ wavelet power spectra are shown on upper, middle, lower panel, respectively. The temporal range is reported in fs (x axis), the y axis represents the frequency (cm^{-1}), the z axis is the $|W(\tilde{\nu},t)|^2$ of the wavelet spectrum expressed in arbitrary units.

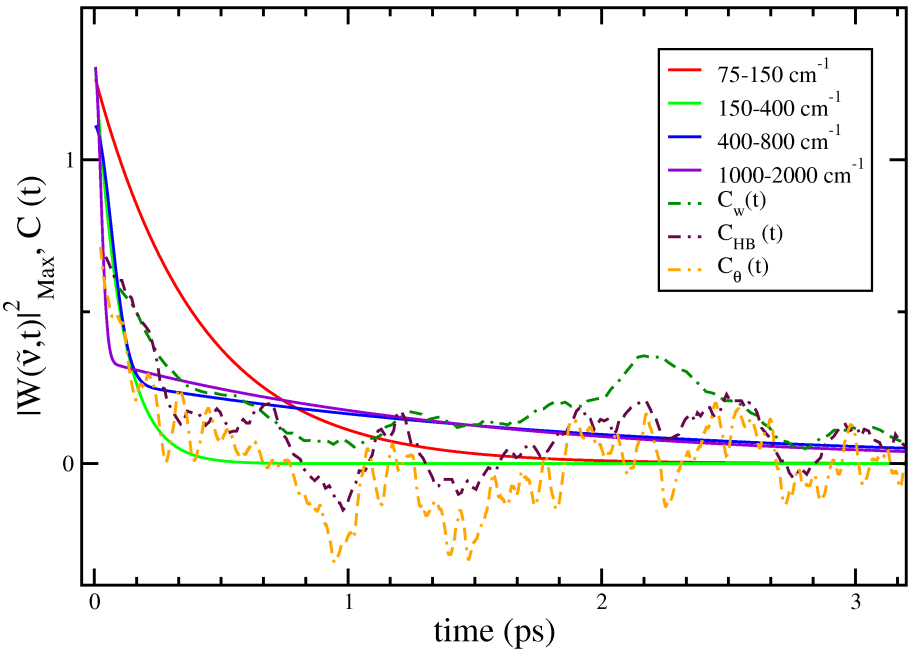

Fig. 1.7: Temporal evolution of the maximum amplitude in several frequency ranges from wavelet spectrum, $|W(\tilde{\nu},t)|^2_{Max}$. Amplitude values are normalized with respect to the corresponding amplitude interval. Relaxation functions of MQ solvation dynamics obtained by analysis of non-equilibrium BOMD\GLOB trajectories in the S_1 state: number of water within the first solvation shell, $C_w(t)$ (broken green line), number of MQ\water hydrogen bonds, $C_{HB}(t)$ (broken maroon line), and water orientational relaxation function, $C_\theta(t)$ (broken orange line) are also reported for comparison.

An inspection of the dynamics affecting the reorganization of MQ micro-solvation is provided by the wavelet power spectra of the MQ structural relaxation functions. The $C_\theta(t)$, $C_{HB}(t)$, $C_w(t)$, wavelet power spectra are shown in Figure 1.6 (upper, middle, and lower panel respectively). The temporal range is the 0-3200 fs (as for simulated TDSS wavelet power spectra). This time the frequency range is 0-1000 cm^{-1}, because higher frequency values did not show any significant band. Therefore no C=O relaxation affects the micro-solvation in a dynamical way and only the collective solvent motions below 1000cm^{-1} affect the first shell dynamics. Observing the band intensity, it is evident that in all spectra are present a rich region below

250 cm^{-1}, proving that the micro-solvation relaxation is strongly influenced by the collective H-bond stretching and bending motions. By an inspection of Figure 1.6 up (WT of $C_\theta(t)$) and middle (WT of $C_{HB}(t)$) panel, we can see a decreasing of the high frequency collective water motions contribution (librations range - 400-800 cm^{-1}) affecting the wavelet power spectrum, leading to the lower (WT of $C_w(t)$) panel where this contribution is completely absent. In fact by an accurate analysis of $C_\theta(t)$ wavelet power spectra is evident that only this function, representing the re-orientational relaxation, is strongly influenced at early time by high frequency water librations motion, in the range between 400-800 cm^{-1}.

Also for this analysis the $|W(\tilde{\nu},t)|^2$ wavelet power spectra intensities decrease during the time, although it is possible to observe different relaxation processes affecting different bands, showing that also these signals are all dominated at longer time by the low frequency collective water motions (breathing modes of bulk water, Debye like relaxation).

In Figure 1.7 we compared the several TDSS frequency relaxation contribution (obtained by the previous $|W(\tilde{\nu},t)|^2_{Max}$ analysis) and the overall trends of the structural relaxation functions. From an accurate inspection of the collective solvent frequency contributions affecting the TDSS decay (< 800 cm^{-1}, therefore the red, the ligh green and blu full lines) we are able to understand the molecularity of the process. In fact the fast librational motions (associated with $C_\theta(t)$ relaxation) mostly resound the slope of the high frequency TDSS contributions (400-800 cm^{-1} and 150-400 cm^{-1}). The H-bond number dynamics affect the middle part of the

TDSS dynamics (150-400 cm^{-1}), finally the first shell water number influences the lower frequency TDSS contribution (75-150cm^{-1}).

This last analysis, beyond the previous relaxation times comparison, explains how the whole TDSS is influenced in a dynamical way by the several collective water motions (librations, H-bond stretching and bending, and breathing modes of bulk water). In fact beyond an initial ultra-fast relaxation of C=O bond order, the TDSS is influenced at early times by the fast re-orientational water dynamics dominated by water librations. After the first picosecond, the TDSS is ruled by collective H-bond stretching and bending. When the signal has reached the equilibrium (after 3.5ps) the low frequency (below 100cm^{-1}) water diffusional breathing modes of bulk dominated the TDSS.

1.3 Computational details

1.3.1 Ground state *ab-initio* dynamics

The ground state molecular dynamics (S_0 MD) of the N-methyl-6-quinolone (MQ) in aqueous solution has been performed exploiting the Atom centered Density Matrix Propagation (ADMP) formalism [56; 57; 70]. The MQ molecule has been treated at DFT level, using the B3LYP [71] functional and the 6-31G(d,p) basis set. The core and valence orbitals were weighted differently during the dynamics with μ valence=0.1 amu bohr^2 for the valence electrons and μ core obtained according to the tensorial fictitious mass scheme described in Ref. [57]. The solute molecule has been fixed at the center of a sphere with radius of 11 Å , including 130 water molecules (which cover about three solvent shells) modeled with the standard TIP3P [72] water model. Non-periodic boundary conditions have been enforced, exploiting the GLOB model [23; 24; 73]. These effective boundaries accounted for interactions between the explicit molecular system and the environment (implicit bulk solvent), considering both short-range dispersion-repulsion and long range electrostatics (from a polarizable dielectric[74; 75]) contributions. An average temperature of 300 K was enforced by a velocity rescaling procedure. The trajectory was collected for 15 ps, after 5 ps of equilibration, and with 0.2 fs as time step.

1.3.2 First singlet excited state *ab-initio* dynamics

The first singlet excited state of the MQ in aqueous solution has been characterized by a Born-Oppenheimer (BO)[76–79] MD. The same QM\MM partition scheme and

level of theory used for the S_0 MD has been adopted, with excited state energies and gradients calculated on the fly by the Time Dependent-DFT formalism [80; 81] (TD-DFT). Non-periodic boundary conditions have been enforced by the GLOB model. The trajectory was collected for 7 ps, after 5 ps of equilibration, and with 0.2 fs as time step.

1.3.3 Stokes shift dynamics

We have chosen 24 points from the phase space sampled during the S_0 MD in order to represent the MQ-water system at the starting time of the Stokes shift dynamics. Those starting points have been picked up at random, except for the criterium according to which the average and the distribution of the transition energes $\Delta E_{S_1 \leftarrow S_0}$ are very close to the steady state $S_1 \leftarrow S_0$ absorption peak and band width, respectively. Similarly, we ensured that the 24 points nuclear kinetic energies E_{kin} reproduced the S_0 average total linear momentum. $\Delta E_{S_1 \leftarrow S_0}$ energy calculated at the TD-B3LYP\6-31G(d,p) level and E_{kin} values of the extracted 24 configurations are reported in Table 1.2.

The starting configurations have been further analysed to ensure the proper representation, on average, of the S_0 structural properties. As concerning the solvent organisation in proximity of the MQ oxygen, we monitored the following parameters involving the MQ oxygen and the water molecules belonging to the first solvation shell: the distance between the water hydrogen and MQ oxygen atoms (H$^{\cdot\cdot}$O), the distance between the water oxygen and MQ oxygen (O$^{\cdot\cdot}$O), and the angle formed by the water hydrogen, the water oxygen and the MQ oxygen (H-O$^{\cdot\cdot}$O). The number

of hydrogen bonds involving the MQ oxygen (N_{HB}) has been considered as well. This latter has been calculated with thresholds of 2.7 Å, 3.5 Å and 30° for the $O_{MQ} - H_{wat}$ distance, the $O_{MQ} - O_{wat}$ distance and the $H_{wat} - O_{wat} - O_{MQ}$ angle, respectively. The structural parameters listed above are reported in Table 1.3. As regards the MQ structure, we monitored the nitrogen-methyl carbon distance (N-C), the oxygen-carbon distance (C-O), and the angle of the quinolone ring subtended by the carbonyl group (C-C(O)-C). Values of these parameters adopted in the extracted configurations are listed in Table 1.4. Finally, in Table 1.5 we compare values of the structural and energetical parameters averaged over the extracted configurations and the whole configurational sampling in the S_0 state.

The 24 configurations constituted the starting points for as many BO\GLOB molecular dynamics followed for about 4 ps and with 0.2 fs as time step. Stokes shift relaxation has been simulated by adopting the same QM\MM partition scheme and level of theory used for the equilibrium excited state MD.

All the calculations have been performed by a locally modified version of Gaussian package [82].

Table 1.2: $S_1 \leftarrow S_0$ transition energies (eV) and nuclear kinetic energies (a.u.) of the Stokes shift starting configurations, labelled by Latin letters.

MD-ID	$\Delta E_{S_1 \leftarrow S_0}$	E_{Kin}	MD-ID	$\Delta E_{S_1 \leftarrow S_0}$	E_{Kin}
A	2.66	0.581744	O	2.56	0.583965
B	2.43	0.584196	P	2.48	0.581949
D	2.71	0.587116	Q	2.37	0.571105
E	2.65	0.585087	R	2.51	0.583391
F	2.54	0.579310	S	2.62	0.578966
G	2.43	0.584196	T	2.40	0.574540
H	2.53	0.579158	U	2.27	0.575237
I	2.38	0.583965	V	2.54	0.573252
J	2.43	0.568866	W	2.29	0.581899
K	2.36	0.586163	X	2.45	0.588840
L	2.36	0.581949	Y	2.51	0.569375
M	2.50	0.581633	Z	2.41	0.572673

Table 1.3: Structural parameters (Å and degrees) and hydrogen bonds number involving the MQ oxygen and the first solvation shell for the MQ\water configurations at the zero time of the Stokes shift dynamics.

MD-ID	H··O	O··O	H-O··O	N_{HB}	MD-ID	H··O	O··O	H-O··O	N_{HB}
A	2.192	3.119	13.48	4	O	2.129	3.065	14.06	3
B	1.860	2.848	6.13	4	P	2.045	2.870	20.77	3
D	1.946	2.895	5.81	4	Q	2.219	3.071	21.14	3
E	2.136	2.998	19.43	3	R	2.280	3.105	21.87	3
F	2.265	3.084	21.54	4	S	2.224	3.116	15.80	3
G	1.860	2.848	6.10	4	T	2.299	3.238	12.39	3
H	2.090	3.005	5.86	4	U	2.312	3.108	23.34	3
I	2.396	3.260	19.23	3	V	2.224	3.104	17.94	3
J	2.213	3.091	19.32	3	W	2.224	3.097	17.08	3
K	2.186	3.042	21.22	3	X	2.223	3.156	14.72	4
L	2.232	3.086	21.41	3	Y	2.304	3.083	25.22	3
M	2.288	3.109	20.71	3	Z	2.260	3.196	10.37	3

Table 1.4: MQ structural parameters (Å and degrees) for the MQ\water configurations at the zero time of the Stokes shift dynamics.

MD-ID	N-C	C-O	C-C(O)-C	MD-ID	N-C	C-O	C-C(O)-C
A	1.492	1.268	114.63	O	1.493	1.268	116.36
B	1.485	1.291	112.43	P	1.473	1.263	114.14
D	1.474	1.276	116.51	Q	1.484	1.289	114.83
E	1.484	1.278	117.48	R	1.494	1.260	113.69
F	1.510	1.273	113.10	S	1.473	1.276	113.58
G	1.485	1.291	112.43	T	1.450	1.253	114.32
H	1.505	1.272	114.45	U	1.466	1.285	115.52
I	1.445	1.269	114.24	V	1.457	1.292	112.89
J	1.478	1.273	118.08	W	1.475	1.263	112.84
K	1.501	1.294	111.34	X	1.479	1.275	115.64
L	1.512	1.268	118.53	Y	1.475	1.291	113.92
M	1.476	1.287	112.16	Z	1.468	1.254	117.53

Table 1.5: Structural (Å and degrees) and energetical (eV and a.u.) parameters for MQ in aqueous solution. Values are averaged over the distribution sampled by MD in the ground state and over the 24 configurations extracted to respresent the $t = 0$ of the Stokes shift dynamics. Standard deviations are also reported in parentheses.

	Starting Configurations	S_0 MD
H··O	2.184 (0.137)	2.211 (0.153)
O··O	3.066 (0.110)	3.057 (0.099)
H-O··O	16.45 (5.98)	28.97 (12.55)
N_{HB}	3.26 (0.45)	3.08 (0.68)
N-C	1.481 (0.017)	1.480 (0.020)
C-O	1.275 (0.012)	1.275 (0.012)
C-C(O)-C	114.61 (1.98)	114.83 (2.05)
$\Delta E_{S_1 \leftarrow S_0}$ (eV)	2.47 (0.11)	2.48 (0.15)
E_{Kin} (a.u.)	0.580598 (0.004478)	0.580772 (0.019105)

Table 1.6: Multi exponential fit parameters. Parameters (times, in ps, and the amplitudes β, in parentheses in %) for the simulated and experimental TDSS.

	Simulation	Experiment
τ_0 $\alpha = 2$	0.019 (58.2 %)	/
τ_1 $\alpha = 2$	0.060 (23 - 55 %)	0.046 (61 %)
τ_2 $\alpha = 1$	0.216 (9 - 23 %)	0.195 (18 %)
τ_3 $\alpha = 1$	0.901 (9 - 22 %)	1.150 (21 %)

1.3.4 Multi exponential fit

The normalized Time Dependent Stokes Shift (TDSS) presented its peculiar bi-phasic behaviour. Therefore it has been disentangled in a superposition of stretched exponentials ($S(t) = \sum_i \beta_i e^{-(t/\tau_i)^{\alpha_i}}$), each characterised by a peculiar relaxation time (τ), affecting the whole decay. The characteristic times, in ps, and amplitudes (β, in %, are reported in Table 1.6. Both the data referred to the simulated and the experimental TDSS are reported for a better comparison. We underline that the ultra-fast component is lost in the experiment because of the experimental time resolution.

Chapter 2

Theoretical tools for characterizing the behavior of transient excited states within bio-macromolecules. The Green Fluorescent Protein case study: optical behavior and excited state photo-reactivity

In this chapter we present our theoretical and computational study to investigate the transient excited states affecting the spectroscopy and reactivity within bio molecules. We have tried to investigate the complex optical behavior of GFP and its chromophore in order to extend the study also at the transient excited states involved in the ESPT responsible of the wild type(wt)-GFP fluorescence.

In the wild type GFP, the chromophore p-hydroxybenzylideneimidazolidinone (HBDI) is present in either the neutral and its deprotonated $HBDI^-$ form, leading to the absorption bands at around 395 and 480 nm (the so called A and B form, see Figure 2.1 A) for the absorption spectra), respectively [83; 85].

In the ground state the wt-GFP presents an equilibrium between the two confor-

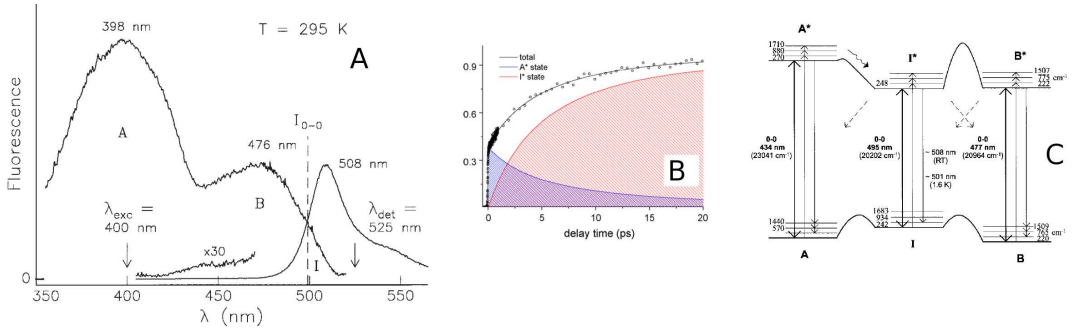

Fig. 2.1: a)Excitation and fluorescent spectra of GFP at 295 K. The neutral (B form) and the anionic (A form) peak are both present. The intersection of red wing of the excitation spectrum and the blue wing of the fluorescence spectrum marks the wavelength of the 0-0 transition of the I form at room temperature, from Ref. [83]. b)Up-converted I* fluorescence fit to a sum of A* and I* emission of wt-GFP, where the I* emission is assumed to rise with decay of A* and then decay with a 3ns lifetime, from Ref. [84]. c) Proposed energy-level scheme of the three photoconvertible forms A, I and B of wt-GFP. The 0-0 and vibronic transition (in $cm^{-}1$) are given, from Ref.[83]

mations, but under physiological condition, the ground-state population of form A is 6 times higher that of form B, suggesting that the ground state is mostly represented by this form.[86]

The anionic chromophore is directly responsible for the bright fluorescence of wt-GFP near 510 nm, with a quantum yield ∼0.8 and a lifetime ∼3 ns [87; 88] (see Figure 2.1 B) for up-conversion time resolved data). The current views on GFP excited state photocycle present a canonical three-state model formulated in Ref[85; 86]. Transformation between the A* and B*, in the excited state, occurs through an intermediate termed I* (see Figure 2.1 C) for the proposed mechanism). Pioneeristic experimental studies observed that the hydroxyl group of Tyr66 of the GFP chromophore transfers a proton through a hydrogen bond network to Glu222, generating an excited state anion responsible of bright fluorescence emission [85; 86] (a process known as excited-state proton transfer; ESPT). Crystallographic and

site-directed mutagenesis experiments identified the connection of hydroxyl group of Tyr66 to the oxygen of Glu222, through the crystallographic wat22 and than the residue of Ser205, at the same time an important role of Ser65 have been inferred for proton transfer even if it not directly involved in the wire [83; 85; 89; 90]. Moreover two different lifetimes have actually been disentangled by a bi-exponential data fit, corresponding to 2.8 ns and 3.3 ns and indicating the existence of two photo-active species in protein [87]. The photochemical characteristics of GFP arise from highly specific protein-chromophore interactions and are very different from the isolated HBDI chromophore in the condensed state, where radiationless decay, probably associated with rapid twisting motions in the excited state, is dominant [91; 92]

Therefore in this chapter, we first test and show the reability of TD-DFT theory, by reproducing the optical absorption of GFP chromophore in several environment, including both the gas-phase and the protein. During this test, we also have part in the completion of the tangled debate on the gas-phase $HBDI^-$ experimental reference absorption value. After we present our minimal model to study the PT reaction mechanism, thanks to a potential energy driven study, showing the concerted fashion of the ESPT mechanism, and how the first neighborhood residues can influence the energetic profile. In the end, we performed an ab intio excited state molecular dynamics (MD) study on the representative A GFP model end we show how, even with the inclusion of full protein matrix effects, the ESPT is still a concerted mechanism and how the subtle balance between the inner vibrational modes dynamics of chromophore and the GFP pocket conformation constrains rules the ESPT and

preserves the fluorescence. In this last study we also present a complete comparison between the ground state and the excited state dynamics, enlightening the crucial role of the several modes affecting the dynamics in different way in the two electronic states.

2.1 The optical absorption of anionic GFP chromophore in gas-phase and in solution

Understanding the photophysics of isolated chromophores is mandatory to control their behaviour in interesting environments (proteins, DNA, solvents). Particularly challenging is the case of 4'-hydroxybenzylidene-2,3-dimethylimidazolinone ($HBDI^-$, see Figure 2.2), the chromophore of the Green Fluorescent Protein (GFP) in the anionic form, which motivated a large number of studies in recent years.[27–33]

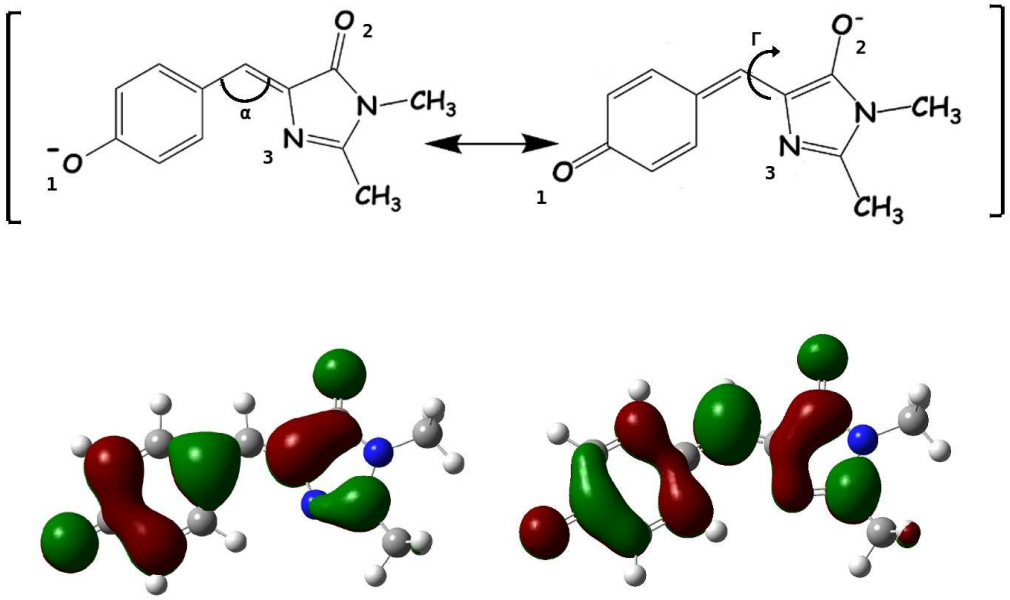

Fig. 2.2: a) Resonance structures and b) HOMO and LUMO contours of $HBDI^-$. Orbitals are obtained at B3LYP\6-31+G(d,p) level of theory.

The isolated $HBDI^-$ shows a value of the photodetachment energy close to the $S_0 \rightarrow S_1$ Vertical Excitation Energy (VEE),[93] peculiarity that makes the absorption measurements in vacuum very difficult to obtain. Action spectroscopy experiments

carried out on $HBDI^-$ in the gas phase by Andersen [94; 95] and Jockusch [96] indicated a maximum in the optical absorption of about 2.59 eV. This value is very close to the absorption band peak of the anionic GFP (2.61 eV),[97] and founds the hypothesis according to which the protein provides a vacuum-like environment to the chromophore for what regards the excitation energy.

On the other hand, the extrapolation from a Kamlet-Taft fit of absorption peaks recorded in several solvents leads to the more energetic gas phase absorption value of 2.84 eV.[98] According to this result, the protein would induce a redshift of about 0.23 eV to the VEE of the chromophore, similarly to other fluorescent proteins like DRONPA.[99] More recently, photodestruction experiments of Zenobi et al. suggested that the gas phase absorption value, promoted by a single-photon, should be above 2.61 eV.[100] In particular, the authors questioned the reliability of action spectroscopy experiments, both in the multiple- or single- photon dissociation regime, to represent the optical absorption spectrum of $HBDI^-$.

Both the hypotheses on the protein effect (near-vacuum or bathochromic environment) are compatible with several computational results presented in literature. Regarding the isolated $HBDI^-$, several VEE values calculated by post-Hartree Fock (post-HF) methods are close to the experimental value of 2.59 eV,[27; 30; 101] while a sophisticated study from Filippi suggested the value of 2.84 eV as a more reliable reference. [32] Regarding the modeling of proteic effects, a vacuum-like environment was hypothesized in post-HF and Time Dependent-Density Functional Theory (TD-DFT) studies.[28; 93; 102; 103] A possible protein-induced hypsochromic shift was

also critically discussed.[33] On the other hand, a bathochromic shift was calculated in two recent works based on coupled cluster [104] and TD-DFT methods.[105]

Unfortunately, the protein effect cannot be settled out by analogy with the absorption of $HBDI^-$ in neat solvents. The optical absorption maximum in several solvents covers a wide range going from 2.57 eV to 2.91 eV,[98; 106] without a clear dependence on the solvent polarity or other properties.[98] $HBDI^-$ was also investigated by implicit and explicit solvent models in water and other solvents.[29; 107–110] However, these studies were not able to reproduce and to explain the experimental trend of the optical absorption.

In this work we simulated the vertical $S_1 \leftarrow S_0$ transition of $HBDI^-$ in gas phase and in environments of dioxane, ethanol, methanol, water, and protein. In all cases we adopted the same TD-DFT [111–114] level of theory for the chromophore and the cybotactic region. The protein environment was modeled recurring to the N-layered integrated molecular orbital and molecular mechanics (ONIOM) scheme,[18–21] while implicit solvent effects were taken into account by a polarizable continuum model [74; 75; 115] in the state specific formalism.[116–121]

We disentangled, for the first time, the observed trend of the $HBDI^-$ absorption peak. According to our results, the peculiar behavior of the chromophore in each case is due to a different combination of steric, electrostatic and specific interactions with the molecular environment. In particular, we obtained a VEE for the anionic GFP which is redshifted of 0.21 eV with respect to the isolated $HBDI^-$. Our analysis also suggests that the optical absorption of the chromophore in the gas phase is close

to 2.84 eV as reported in Ref. [98].

In the following, we describe the modeling of anionic GFP and solvated $HBDI^-$ in Section 2.1.1, and discuss the results in Section 2.1.2. Finally, we give our conclusions in Section 2.1.3.

2.1.1 Methods and models

All the calculations were carried out by using B3LYP [71] and CAM-B3LYP [122] functionals and the 6-31+G(d,p) basis set, in both the time independent and TD-DFT formalism, this latter to evaluate the vertical $S_1 \leftarrow S_0$ transition energy. Implicit solvent effects were taken into account by the Conductor-like Polarizable Continuum Model (C-PCM).[74; 75; 115] When combined with TD-DFT, C-PCM was adopted in the state specific formalism.[116–121] Optimizations for solute-solvent clusters also included the Grimme's dispersion contribution in the electronic potential. [123] The protein environment was modeled by ONIOM,[18–21] in combination with both the TD-DFT [124; 125] and the C-PCM.[126; 127] The Gaussian [82] suite of programs was used for all calculations.

2.1.1.1 Modeling HBDI$^-$ in solvent

The environment effects on the HBDI$^-$ transition energies were analyzed for solvents of different polarity and proticity: 1,4-dioxane (dielectric constant $\varepsilon = 2.21$), ethanol ($\varepsilon = 24.85$), methanol ($\varepsilon = 32.61$) and water ($\varepsilon = 78.35$). Hereafter, HBDI$_s$ indicates the chromophore embedded in a solvent s fully accounted for by the continuum model, with s= d, e, m, and w for dioxane, ethanol, methanol and water, respectively. Explicit solute-solvent interactions were also analyzed by the study of HBDI$^-$-solvent clusters embedded in a self consistent solvent reaction field for ethanol, methanol and water solutions. More specifically, we monitored explicit interactions with three solvation sites of the HBDI$^-$ molecule: the phenolic oxygen

(O1 of Figure 2.2), the imidazolinone oxygen (O2) and one of the imidazolinone nitrogens (N3). $HBDI^-$ shows indeed a complex topology of the solvation sites. The hydrogen bonds network retrieved from the anionic GFP structure (vide infra) shows O1 and O2 involved in three and two hydrogen bonds, respectively, with the protein residues and a crystallographic water. Three specific interactions for O1 are compatible with the negative charge partially located on the phenolic group, the O1 π electronic density acting as hydrogen bond acceptor. natural population analysis (NPA, Ref. [128]) charges calculated in the gas phase for phenolic and imidazolinone oxygens show similar values (-0.697 for O1 and -0.694 for O2, please see Figure 2.3), indicating a similar weight of the two resonance structures shown in Figure 2.2.

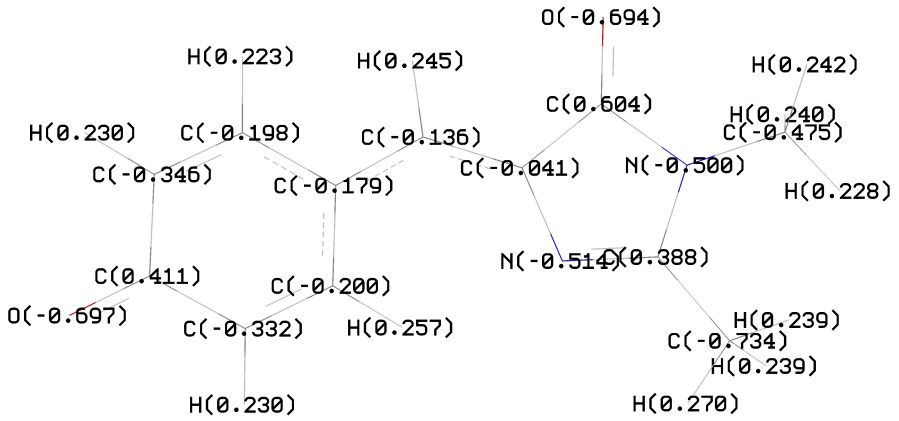

Fig. 2.3: NPA of $HBDI^-$ in the gas phase at B3LYP\6-31+G(d,p) level of theory.

In the isotropic solvent we can therefore expect also the imidazolinone oxygen possibly involved in three specific interactions. Moreover, the imidazolinone nitrogen (NPA charge value of -0.514) can be engaged in specific interactions directed both above and below the molecular plane. Radial distribution functions calculated by

MonteCarlo simulations of the trans $HBDI^-$ in water showed indeed a coordination number of about three for O1 and of about two for N3.[29] An accurate prediction of the specific interactions distribution would require proper simulations with an explicit representation of the solvent. On the other hand, a representative cluster should take into account the effect that the cybotactic region has on both the chromophore structure and the absorption spectrum. In the following, we assume that a fully solvated chromophore may represent, on average, the drift of the electronic transition when going from the gas phase to the solution. In summary, we can hypothesize a cluster to fully saturate the solvation sites of the molecule which involves 3, 3, and 2 solvent molecules specifically interacting with O1, O2 and N3, respectively. We considered such clusters hereafter indicated as $HBDI_{s,clus}$, with s= e, m, and w for ethanol, methanol and water, respectively. A summary of $HBDI^-$-solvent systems considered in the present work is reported in table 2.1.

system	explicit molecules on sites O1,O2	explicit molecules on site N	solvent	short name
$HBDI^-$	0	0	dioxane	$HBDI_d$
$HBDI^-$	0	0	ethanol	$HBDI_e$
$HBDI^-$	0	0	methanol	$HBDI_m$
$HBDI^-$	0	0	water	$HBDI_w$
$HBDI(CH_3CH_2OH)_8^-$	3	2	ethanol	$HBDI_{e,clus}$
$HBDI(CH_3OH)_8^-$	3	2	methanol	$HBDI_{m,clus}$
$HBDI(H_2O)_8^-$	3	2	water	$HBDI_{w,clus}$

Table 2.1: Summary of $HBDI^-$-solvent models analyzed in this work. For each case the solvent, the number of explicit solvent molecules on different solvation sites, and abbreviation name are reported.

2.1.1.2 Modeling the anionic Green Fluorescent Protein

According to the classification of fluorescent proteins given by Tsien,[35] the structure of the GFP mutant S65T (1EMA as PDB ID) [90] belongs to the class 2 (EGFP's), and is often considered as a starting model for the anionic GFP.[93] Coordinates of 1EMA structure were augmented with hydrogen atoms located at positions optimized by the Amber force field.[129] The side chain of the residue 65 was set to Ser as in the wild type GFP. We considered the majority of residues neutral, while Arg, Lis, Asp and Glu have been treated as charged. The histidine showed a fine equilibrium of the possible protonation states: we protonated six histidines in both δ and ϵ positions, three in ϵ and only H148 in δ.

Following the ONIOM extrapolative scheme, the GFP has been then portioned into two layers, where a *model* region was treated at DFT or TD-DFT *high* level, while the whole molecular system, referred to as *real*, was represented at *low* level by the Amber force field,[129] including the parameters specifically developed for the chromophore by Reuter.[130]

We considered two ONIOM *models*. The first (hereafter PI, see Figure 2.4b) includes the anionic chromophore, the side chains of Ser65, Ser205, Glu222, and the crystallographic water molecule hydrogen bonded to the chromophore phenolic oxygen. The second *model*, (hereafter PII, see Figure 2.4c) includes PI, His148, Asn146, Thr203, Arg96, Gln94, and the crystallographic water molecules in close proximity of the chromophore, namely within 5 Å from the carbon at the center of the HBDI methine bridge. In this way, the hydrogen bond network surrounding the

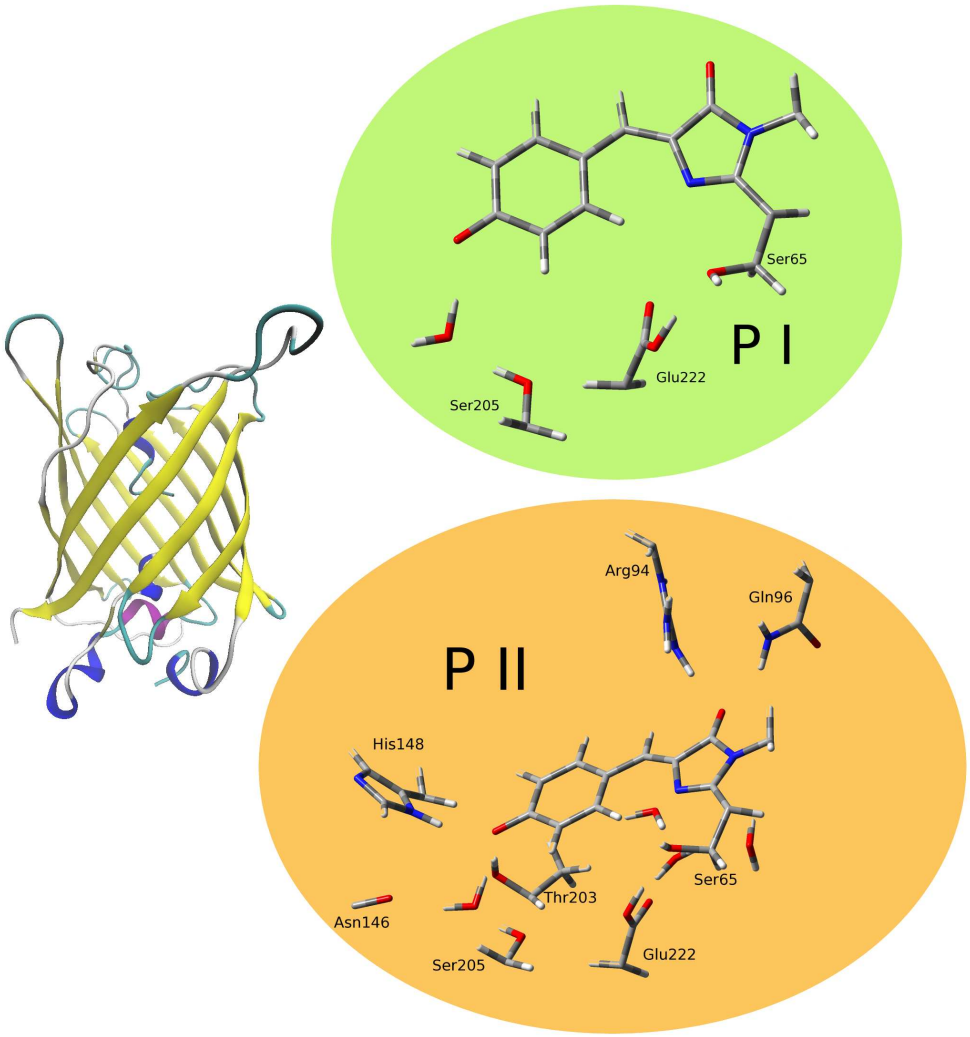

Fig. 2.4: Anionic GFP structure in a ribbon representation (left) optimized at ONIOM TD-B3LYP\6-31+G(d,p)\Amber\C-PCM-X level. ONIOM PI *model* includes the anionic chromophore, side chains of Ser65, Ser205, Glu222, and the crystallographic water hydrogen bonded to the phenolic oxygen of the chromophore (upper panel); ONIOM PII *model* includes PI, His148, Asn146, Thr203, Arg96, Gln94, and the crystallographic water molecules within a radius of 5 Å of a sphere centered on the methine bridge of the chromophore (lower panel).

chromophore is fully accounted for at the quantum mechanical level.

In order to preserve the chemical nature of peptide bonds for the residues belonging to the DFT\molecular mechanics interface, the cuts have been chosen along single bonds, and, in general, at nonpolar or slightly polar bonds, preferably C-C

ones. The dandling valence have been capped by link hydrogen atoms. The electrostatic interaction between the two levels were accounted by an electronic embedding scheme.[19; 131]

Structure optimization for PII partition and VEE calculations for both PI and PII partitions were performed at the ONIOM (TD)-B3LYP\6-31+G(d,p)\Amber level. In all cases the aqueous solvent was treated implicitly by the so-called ONIOM\C-PCM-X [126; 127] scheme, where a solvent reaction field is computed separately in each ONIOM sub-calculation on the PCM cavity of the *real* system. In particular, the protein solvent accessible surface was adopted to define the PCM cavity.

In order to disentangle different effects on the VEE, we also considered calculations on the isolated chromophore arranged in a protein-like structure, with methyl-terminated side groups of the imidazolidone ring, thus reproducing the $HDBI^-$ molecule.

2.1.1.3 VEE shift of $HBDI^-$ in protein and solution

The $S_1 \leftarrow S_0$ excitation energy of the chromophore calculated in a given environment (neat solvent or solvated protein) can be indicated by G^{01}_{env}, including in all cases the free energy contribution from the implicit treatment of the solvent. [116–119] The total shift of the VEE due to the environment, ΔG^{01}_{tot}, can be therefore obtained as the difference between G^{01}_{env} and the excitation energy in the gas phase, E^{01}_{vac}:

$$\Delta G^{01}_{tot} = G^{01}_{env}(R_{env}) - E^{01}_{vac}(R_{vac}) \tag{2.1}$$

where R_{vac} and R_{env} collect the structural coordinates of the chromophore optimized in gas phase and in the environment, respectively. The subscript *vac* in the energy symbol indicates an excitation energy calculated for the electronic density of the unperturbed chromophore. The subscript *env*, on the other hand, refers to excitation energies obtained from the chromophore electronic density which is polarized by both the continuum solvent and the molecular surroundings (protein or explicit solvent molecules, when present).

The total solvent shift can be further decomposed in the following contributes

$$\Delta G^{01}_{tot} = \Delta E^{01}_{ind} + \Delta E^{01}_{pol/int} + \Delta G^{01} \tag{2.2}$$

where the first term, ΔE^{01}_{ind}, accounts for the indirect effect due to chromophore structural change induced by the environment, and is evaluated as the difference of the excitation energies calculated in the gas phase at the R_{env} and R_{vac} geometries, respectively:

$$\Delta E^{01}_{ind} = E^{01}_{vac}(R_{env}) - E^{01}_{vac}(R_{vac}) \tag{2.3}$$

The second term in Eq. 2.2, $\Delta E^{01}_{pol/int}$, is the transition energy shift due to the electronic density polarization in presence of both the bulk (implicit solvent reaction field) and the molecular environment (protein or explicit solvent), and to the specific interactions involving the chromophore. It can be evaluated as

$$\Delta E^{01}_{pol/int} = E^{01}_{env}(R_{env}) - E^{01}_{vac}(R_{env}) \tag{2.4}$$

In absence of specific interactions ($HBDI_s$ systems), this term can be also indicated as ΔE^{01}_{pol}. The last term of Eq. 2.2, ΔG^{01}, is the variation in the solvation free energy

due to the electronic excitation and can be evaluated as

$$\Delta G^{01} = G^{01}_{env}(R_{env}) - E^{01}_{env}(R_{env}) \tag{2.5}$$

The excitation energy calculated including the implicit solvent, G^{01}_{env}, is intended in the so-called non equilibrium regime, according to which fast coordinates of the solvent instantaneously adjust to the electronic excitation, while slow coordinates remain equilibrated to the solute electrostatic potential in the ground state.

2.1.2 Results and discussion

2.1.2.1 HBDI$^-$ in solution

2.1.2.1.1 Implicit treatment of the solvent

In the upper panel of Table 2.2 we report the energetic analysis discussed in Section 2.1.1.3 for HBDI$^-$ in solution within a full continuum representation of the solvent (HBDI$_s$ systems). Experimental VEE shifts are reported considering 2.84 eV [98] as the reference in the gas phase. VEE and VEE shifts were calculated at the TD-B3LYP \6-31+G(d,p)\C-PCM level of theory for corresponding minimum energy structures in the ground state.

	HBDI$_d$	HBDI$_e$	HBDI$_m$	HBDI$_w$
VEE	3.09	3.18	3.18	3.18
ΔE^{01}_{ind}	-0.04	-0.04	-0.04	-0.04
ΔE^{01}_{pol}	0.03	0.07	0.07	0.07
ΔG^{01}	0.04	0.09	0.09	0.09
ΔG^{01}_{tot}	0.03	0.12	0.12	0.12
		HBDI$_{e,clus}$	HBDI$_{m,clus}$	HBDI$_{w,clus}$
VEE		3.07	3.12	3.14
ΔE^{01}_{ind}		-0.08	-0.06	-0.06
$\Delta E^{01}_{pol/int}$		0.01	0.03	0.07
ΔG^{01}		0.08	0.09	0.07
ΔG^{01}_{tot}		0.01	0.06	0.08
Exp.[a] ΔG^{01}_{tot}	0.03	-0.02	0.06	0.07

a) Variations with respect to the experimental absorption value of 2.84 eV in the gas phase of Ref. [98]

Table 2.2: VEE and VEE shifts values (eV) for HBDI$^-$ in neat solvents (HBDI$_s$ and HBDI$_{s,clus}$ systems) calculated at the TD-B3LYP\6-31+G(d,p)\C-PCM level of theory.

From Table 2.2 we observe that dioxane leads to a total shift ΔG^{01}_{tot} of 0.03 eV in the vertical excitation energy. The solvent effect can be disentangled in a red shift due to a structural indirect effect (ΔE^{01}_{ind}= -0.04 eV), which is mostly compensated by

a blue shift of 0.03 eV due to the solute polarization (ΔE^{pol}). On inspection of energy levels (data not shown), we observe that the structural distortion slightly stabilizes the S_1 state. On the other hand the solute polarization works against the solvation process, thus de-stabilizing both the ground and the excited states. However, S_1 is characterized by a larger polarization energy, thus leading to a blueshift in the VEE with respect to the vacuum. Finally, the free energy contribution ΔG^{01} is a blue shift of 0.04 eV. The bulk solvent has indeed more favorable interactions with the chromophore in the ground state, characterized by a dipole moment larger than in the excited state of about 1.5 D.

The analysis of $HBDI_s$ in ethanol, methanol and water shows mostly equivalent results, namely a total blue shift ΔG^{01}_{tot} of 0.12 eV. While the structural indirect shift is similar to that evaluated in dioxane (ΔE^{01}_{ind}= -0.04 eV), the polarization effect is larger (ΔE^{01}_{pol} = 0.07 eV). The free energy contributions is also more consistent (blue shift ΔG^{01} of 0.09 eV), in agreement with the polar nature of the solvents.

2.1.2.1.2 Solute-solvent clusters in solution

In the lower panel of Table 2.2 we report the VEE analysis for $HBDI^-$-solvent clusters in ethanol, methanol and water solutions ($HBDI_{s,clust}$ systems). VEE and VEE shifts were calculated at the TD-B3LYP\6-31+G(d,p)\C-PCM level of theory for corresponding minimum energy structures in the ground state.

All the clusters show a similar structural effect on the VEE, namely a significant redshift (ΔE^{01}_{ind} equals -0.08 eV in ethanol and -0.06 eV in methanol and water). Therefore, the structural effect is enhanced by the presence of explicit solvent

molecules. However, as it happens for $HBDI_s$ systems (full continuum representation of the solvent), the amount of ΔE^{01}_{ind} is not helpful to discriminate the solvent nature.

On the other hand, contributions due to the explicit solvation and to the polarization effect are different, going from a nearly nihil effect in the ethanol ($\Delta E^{01}_{pol,int}$ = 0.01 eV), to a more sensible variation in the methanol ($\Delta E^{01}_{pol,int}$ = 0.03 eV) and water ($\Delta E^{01}_{pol,int}$ = 0.07 eV) solutions, respectively. We evaluated VEE shifts also for isolated HBDI-solvent clusters, i.e. by TD-B3LYP\6-31+G(d,p) calculations not including the treatment of the implicit solvent bulk. In this case we obtained $\Delta E^{01}_{pol,int}$ values of -0.04 eV, -0.02 eV and 0.03 eV for ethanol, methanol and water, respectively. This result suggests a compensation of effects due to specific interactions and to the polarization from the bulk solvent. Finally, the free energy contribution ΔG^{01} is similar (about 0.08 eV) in all cases.

$HBDI^-$ shows an experimental trend not correlated to the solvent polarity. For example, the absorption maximum in ethanol is redshifted with respect to the apolar dioxane, while methanol and water are blueshifted.[98] It is worthy to compare in more detail our VEE analysis performed in dioxane ($HBDI_d$) and in ethanol ($HBDI_{e,clus}$). According to the present study, absolute values of ΔE^{01}_{ind} and ΔG^{01} are larger in ethanol because of the larger polarity, but in the two solvents they compensate in a similar way. Dioxane and ethanol are similar also for what regards the $\Delta E^{01}_{pol/int}$ term. In the first case we observe a small polarization of an apolar solvent, while in the second case we have a compensation of polarization and ex-

plicit interactions effects. As a consequence, $HBDI^-$ shows a VEE value in ethanol redshifted with respect to dioxane, in nice agreement with the experiment.

Regarding methanol and water, the larger polarity leads to greater $\Delta E^{01}_{pol/int}$ terms. These solvents show indeed a similar total shift ΔG^{01}_{tot} (0.06 eV and 0.08 eV for methanol and water, respectively), again in excellent agreement with the experimental values (0.06 eV and 0.07 eV [98]).

2.1.2.1.3 Structural effect on VEE

In Table 2.3 we list geometrical parameters of isolated $HBDI^-$ and $HBDI^-$-solvent systems optimized at the B3LYP\6-31+G(d,p) and B3LYP\6-31+G(d,p)\C-PCM levels, respectively. Minimum energy structures of $HBDI_d$ and $HBDI_{s,clus}$ are also reported in Figure 2.5.

	CO1	CO2	α	Γ
$HBDI^-$ (isolated)	1.259	1.243	132.22	0.01
$HBDI_d$	1.276	1.245	131.44	0.00
$HBDI_e$	1.276	1.245	131.44	0.00
$HBDI_m$	1.276	1.245	131.42	0.00
$HBDI_w$	1.276	1.245	131.32	0.01
$HBDI_{e,clus}$	1.300	1.265	130.59	1.84
$HBDI_{m,clus}$	1.302	1.265	131.66	1.66
$HBDI_{w,clus}$	1.299	1.265	131.54	1.53

Table 2.3: Structural parameters (Å and degrees) of $HBDI^-$ optimized in vacuum and in several solvents at B3LYP\6-31G+G(d,p) and B3LYP\6-31+G(d,p)\C-PCM levels, respectively.

The dependence of VEE on the structure of the GFP chromophore has been already analyzed. For instance, a correlation has been discussed between the excitation energy and an alternate-bond parameter of the chromophore, representing the equilibrium of two resonant structures in the protein.[28] Here, we focus on those pa-

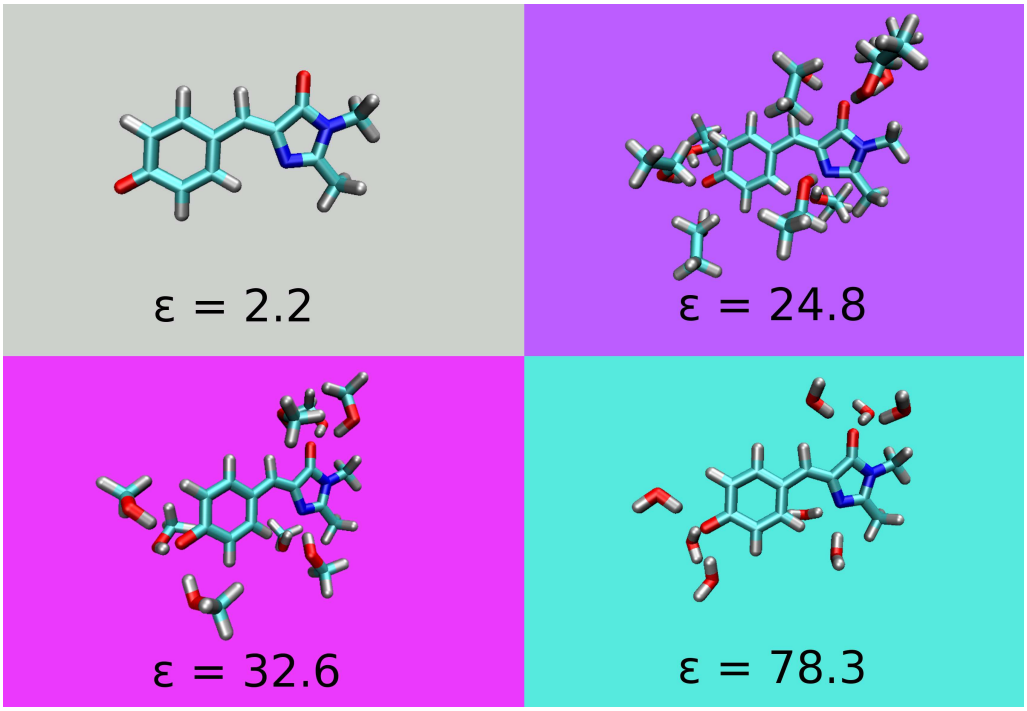

Fig. 2.5: HBDI$^-$ and HBDI$^-$-solvent clusters optimized at the B3LYP\6-31+G(d,p)\C-PCM level in dioxane (upper left panel), ethanol (upper right panel), methanol (lower left panel), and water (lower right panel)

rameters more sensitive upon the optimization in solvent, namely the CO distances (CO1 and CO2 indicating the phenolic and imidazolinone CO groups, respectively), the CCC angle representing the bending of the methine bridge (α in Figure 2.2), and the NCCC dihedral representing the relative torsion of the two rings in the molecule (Γ angle of Figure 2.2). From Table 2.3 we observe the elongation of the CO bonds when going from the isolated to the solvated HBDI anion. The angle α slightly decreases, while the Γ angle is different from zero in HBDI$_{s,clus}$ systems. To further analyze the structural effect on the excitation energy, we performed VEE calculations in both the gas phase and water solution for several values of CO1, CO2, α and Γ parameters, starting from the HBDI$^-$ structure optimized in vacuum.

We obtained trends drawn in Figure 2.6.

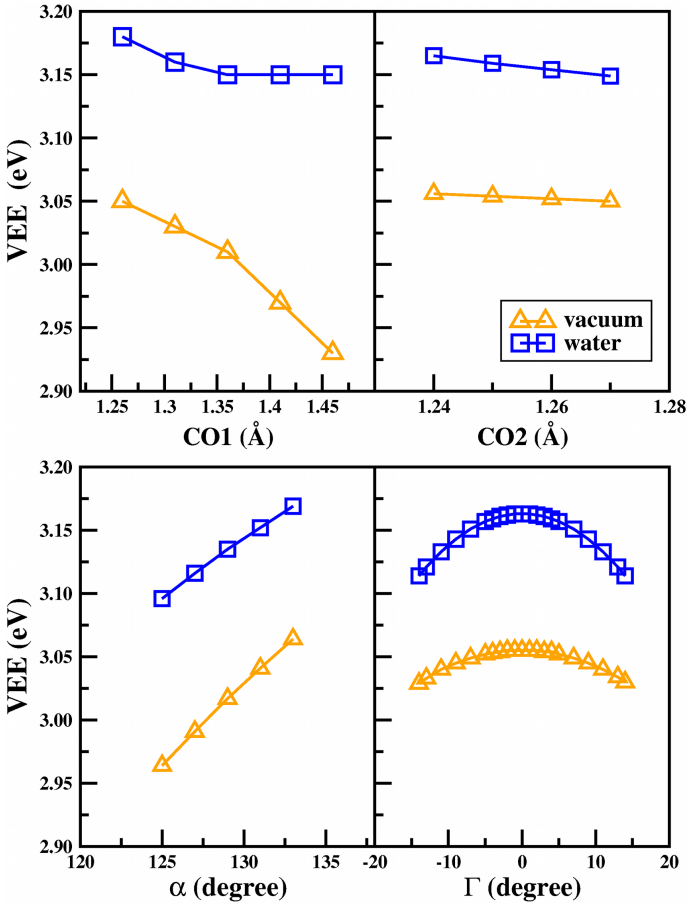

Fig. 2.6: Trends of vertical excitation energies (eV) with respect to $HBDI^-$ structural parameters (Å and degrees) calculated at the TD-B3LYP\6-31+G(d,p) level of theory.

We note that increasing the phenolic CO bond length results into a redshift of the VEE (Figure 2.6, upper left panel). The electronic density located on the O1 oxygen is larger in the ground S_0 than in the excited S_1 state, as it can be observed by inspection of HOMO and LUMO contours in Figure2.2. This difference, however, is sensibly reduced on the CO1 bond elongation, with a consequent redshift of the VEE. This effect is partly compensated when the water environment is included in the calculation. VEE is less dependent on the imidazolinone CO elongation, both in

the vacuum and the water environment, at least for the considered range of values (Figure 2.6, upper right panel). Moderate torsions of the Γ angle (up to 6 degree in absolute value) also scarcely affect the VEE (Figure 2.6, lower right panel). On the other hand, the α angle shows a significant influence on the VEE transition (Figure 2.6, lower left panel). By comparison of HOMO and LUMO contours, we observe a shift of the electronic density from the CC bonds of the methine bridge toward the central carbon upon the excitation. It can be expected that a larger bending of the bridge (increasing of the α angle) affects the S_1 more than the S_0 state, leading to a de-stabilization of the S_1 level and a a blueshift of the electronic transition.

2.1.2.2 Green Fluorescent Protein

CO1	CO2	α	Γ
1.317	1.252	128.16	13.48

Table 2.4: Structural parameters (Å and degrees) for anionic GFP optimized at the ONIOM B3LYP\6-31+G(d,p)\Amber\C-PCM-X level of theory considering PII of Figure 2.4 as the *model*.

In Table 2.4 we list structural parameters for the anionic GFP optimized at the ONIOM B3LYP\6-31+G(d,p)\Amber\C-PCM-X level of theory in the PII partition (see Figure2.4 and Section 2.1.1.2), while energy contributions to the VEE calculated for PI and PII partitions are reported in Table 2.5.

Structural change of the chromophore with respect to the arrangement in the gas phase can be summarized in the elongation of CO bonds and a shrinkage of the α angle, along with a sensible increasing of the Γ torsion. Variations of the

	GFP
VEE	2.85
ΔE^{01}_{ind}	-0.22
$\Delta E^{01}_{pol/int}(PI)$	0.12
$\Delta E^{01}_{pol/int}(PII)$	0.01
ΔG^{01}	0.00
$\Delta^{a} G^{01}_{tot}$	-0.21
Exp.$^{b}\Delta G^{01}_{tot}$	-0.23

a) Value calculated for PII ONIOM partition: $\Delta G^{01}_{tot} = \Delta E^{01}_{ind} + \Delta E^{01}_{pol/int}(PII)$;
b) Variation with respect to the experimental VEE in the gas phase reported in Ref. [98] (2.84 eV);

Table 2.5: VEE and VEE shifts values (eV) for anionic GFP calculated at the ONIOM TD-B3LYP\6-31+G(d,p)\Amber\C-PCM-X level of theory.

phenolic CO and the α angle are responsible of the indirect effect on VEE, ΔE^{01}_{ind}, consisting of about 0.22 eV toward the red. This interpretation is compatible with the analysis previously discussed (see Figure 2.6). Variation of VEE calculated on the GFP in the PI partition, $\Delta E^{01}_{pol/int}(PI)$, is a blueshift of 0.12 eV. Here, the proteic environment is mostly represented by the Amber force field, affecting the TD-DFT calculation through atomic charges in the Kohn Sham equations of the PI model. This contribution appears similar to the polarization effect in the full continuum representation of the solvent (see the ΔE^{01}_{pol} in the fourth row of Table 2.2). That means, the protein represented at MM level gives an electrostatic perturbation stabilizing the dipole in the ground state, leading to a blueshift of the transition. On the other hand, when the TD-DFT involves the larger PII partition, the drift in VEE is strongly reduced to a $\Delta E^{01}_{pol/int}(PII)$ of 0.01 eV. This suggests that the blushifting electrostatic environment in PI is now mostly compensated. In this case the effect is similar to the $\Delta E^{01}_{pol/int}$ induced by the embedding with

explicit solvent of medium polarity (see $\Delta E^{01}_{pol/int}$ for ethanol and methanol, tenth row of Table 2.2). This suggests that the close environment of HBDI (PII partition in the protein, or solvent clusters in solution) provides complex effects on VEE not inferable from the electrostatics (electronic embedding of MM charges in the protein, or of the polarizable isotropic medium in the solution). On the contrary, those effects need to be accounted for specifically at quantum mechanical level. The solvent surrounding the protein does not contribute to the VEE (nihil ΔG^{01}), and an overall redshift of 0.21 eV is the calculated total proteic effect on the HBDI optical absorption.

2.1.2.3 HBDI anion in the gas phase

Sophisticated post-HF methods provided several VEE values for $HBDI^-$. [91; 132–136] CASPT2 (2.67 eV),[27] State-Averaged CASSCF (2.69),[101] and MRMP2 (2.61),[30] results were compared to the experimental value of 2.59 eV, [94–96] while the CASPT2 result from Filippi (2.92 eV) [32] indicated the value of 2.84 eV [98] as reference. Regarding TD-DFT, several studies proposed excitation energies in a range of 2.94-3.10 eV.[32; 33; 108] Our calculated value for $HBDI^-$ in the gas phase (3.06 eV) is in agreement with these previous studies.

In Figure 2.7 we report a summary of the calculated VEE in several environments. We reproduced the experimental trend of the optical absorption of $HBDI^-$ in GFP, dioxane, ethanol, methanol, and water, with an average error of 0.23 eV and a standard deviation of 0.015 eV. The calculated VEE value of isolated $HBDI^-$ enters this systematic error when compared to the experimental value of 2.84 eV,[98] while

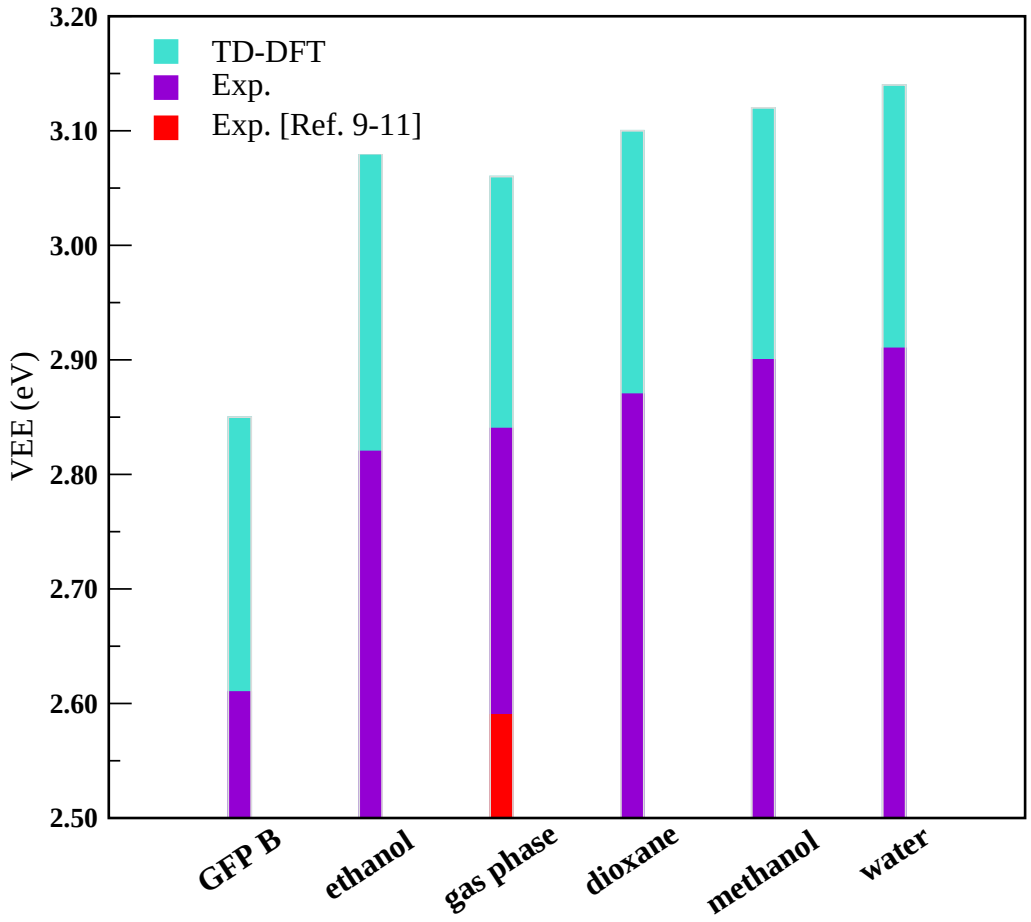

Fig. 2.7: Experimental optical absorption maxima and calculated VEE (eV) for the anionic HBDI chromophore in vacuum, several solvents and GFP. The theoretical values are obtained at TD-B3LYP\6-31+G(d,p), TD-B3LYP\6-31+G(d,p)\C-PCM and ONIOM TD-B3LYP\6-31+G(d,p)\Amber\C-PCM-X levels of theory respectively for the gas phase, solutions, and the protein. The red bar indicates the experimental optical absorption value in the gas phase reported by Andersen [94; 95] and Jockusch [96]. All the other experimental values for the gas phase and solutions are reported by Dong et al.[98], while for the anionic GFP the value is taken from Refs. [137] and [83]

it would correspond to an error of 0.48 eV if the reference value of 2.58 eV is considered. Therefore, this latter case would imply an important discontinuity in the TD-DFT accuracy when passing from the gas phase to the solution treatment. This hypothesis could be justified by the metastability of the S_1 state of the isolated $HBDI^-$, and by the inadequacy of density functionals such B3LYP to reproduce the

correct distribution of the excited electronic levels. In order to verify this possibility we considered VEE calculations for $HBDI^-$ in the gas phase, solvent clusters and the protein by adopting the CAM-B3LYP functional, which asymptotic behavior allows for a more reliable sequence and relative spacing of the TD-DFT roots (excited state levels). Continuum solvent contributions, however, were not considered in these calculations. Results, reported in Table 2.1.2.3, show an average error and standard deviation of 0.24 eV and 0.06 eV, respectively, for VEE values of solvated $HBDI^-$. The CAM-B3LYP VEE for the isolated $HBDI^-$ corresponds to an error of 0.28 eV and 0.54 eV when compared to the experimental values of 2.84 eV and 2.59 eV, respectively. Again, the calculation enters the accuracy assessed by the level of theory only in the first case. Other arguments are in favor of 2.84 eV as a reliable value of the isolated $HBDI^-$ optical absorption. The value of 2.84 eV is closer to the $HBDI^-$ absorption recorded in dioxane solution (2.87 eV).[98] This similarity between dioxane and vacuum environment is what one could expect on the basis of the low polarity of dioxane and the absence of solute solvent specific interactions, and is actually validated by our analysis. Finally, the experimental value from Ref. [98] corresponds to a red shift induced by the proteic environment of 0.23 eV, as our analysis also confirms.

	VEE	exp
vacuum	3.12	2.84 [98]
$HBDI_d$	3.10	2.87 [98]
$HBDI_{e,clus}$	3.05	2.82 [98]
$HBDI_{m,clus}$	3.06	2.90 [98]
$HBDI_{w,clus}$	3.10	2.91 [98]
GFP (PII)	2.96	2.61 [97]

Table 2.6: VEE (eV) analysis performed by TD-CAM-B3LYP for $HBDI^-$, $HBDI_d$, $HBDI_{s,clus}$, and anionic GFP structures in the gas phase.

2.1.3 Conclusions

We simulated with a systematic error the trend of the optical absorption band for the GFP anionic chromophore in several environments, including protein, dioxane, ethanol, methanol and water. Distortion of the chomophore structure induced by the environment leads to a redshift of the VEE in all the cases. This effect is mainly due to the elongation of carbonyl groups in the two rings of the molecule, and to a straining of the bridge region, represented by the increasing of the angle subtended at the bridge center. Polarization of the chromophore and electrostatic interactions with the environment lead to a blueshift of the electronic transition, due to the synergy of a larger de-stabilizing polarization energy in the excited state and greater stabilizing solute-solvent interactions in the ground state, which is characterized by a larger dipole. However, these effects are dominant only in the case of the high polar aqueous solvent. In the other cases they are modulated by redshifting specific interactions of $HBDI^-$ with the cybotactic region that are accurately accounted for only when treated at quantum mechanical level. Trends not correlated with the solvent polarity, like the increasing absorption energy when passing from ethanol

to dioxane and to methanol are therefore explained with a fine balance of different steric and electronic effects on the $HBDI^-$ photophysics, resulting in a peculiar VEE in each environment.

Regarding the gas phase, the calculated VEE enters the systematic error assessed by the level of theory only if the value of 2.84 eV[98] is considered as the experimental reference. This result is compatible with the conclusions of Zenobi, who suggested that the $HBDI^-$ optical absorption in the gas phase should be above 2.61 eV.[100] As a consequence, the protein environment would affect the chromophore absorption with a bathochromic shift of 0.23 eV, in nice agreement with our calculated VEE redshift of 0.21 eV.

2.2 Modeling the GFP excited state proton transfer

The advancement in time-resolved spectroscopic techniques allowed for enlightening many aspects of the GFP ESPT in recent years.[138–143]

Time resolved GFP IR experiments proposed a concerted proton motion along the wire, during the ESPT mechanism, with no intermediate states. Meech and coworkers have shown that upon excitation the time dependent increasing amplitude in the bleach of the band around 1565 cm^{-1} and the rise of the transient at 1712 cm $^{-1}$ are observed and associated to Glu222 protonation process in wt-GFP ESPT [139; 140].

Femtosecond Raman spectroscopy showed a strong anharmonic coupling between the high frequency C-O and C=N stretching modes at opposite ends of the conjugated chromophore and the coherent low frequency HBDI rings modes. This suggested a double role of GFP in the ESPT: the inhibition of the radiationless deactivation through the free rotation around chromophore bridging bond and the induction of a preferential and low barrier de-activation ESPT based on a well-defined hydrogen bond system [141]. Recently VIS\midIR pump probe experiments also suggested that the excitation could favor the proton transfer not for an increased HBDI photo-acidity. Rather the photo-excitation induces conformational proton wire changes that modify the interaction between the chromophore and the protein pocket. Indeed after the photo-excitation, changes in the position of protons in the H-bond network lead to a partial initial protonation of Glu222, creating at

same time a low barrier hydrogen bonded system [142]. In conclusion the novel time resolved spectroscopy experiments suggested that the GFP environment provides a directional coordinate for the ultra-fast proton transfer reaction in contrast with disordered liquids, showing that absorption of light by GFP induces in ∼3 ps a partial protonation of Glu222 giving rise to dual emission at 475 and 508 nm [142; 143], although the radiationless relaxation in protein and solutions have not yet been completely understood.

The ESPT of HBDI have also been investigated by theoretical methods in order to understand the mechanism ruling the proton loss and the subsequently $HBDI^-$ fluorescence. The main issue of all theoretical works has been to find an accurate theory level suitable for a realistic model, because of the multitude of effects affecting the reaction: describing protein environment effects on electronic density and including the sterical constrains on conformational degrees of freedom are both mandatory to describe the ESPT.

The studies based on DFT have chosen a minimal partition for describing the hydrogen bond network, showing that also in the ground state the proton-transfer process is concerted and fast, with a single potential barrier along the reaction coordinate and no stable intermediates [37; 38]. The proton-wire have been also studied by CASPT2\\CASSCF quality reference energies according to fitted empirical valence bond PES, functions that used a planar constrained hydrogen bond wire and HBDI geometry, as a reference model [39]. The above described fitted PES has been characterized in static terms, characterizing its stationary points, finding only a po-

tential energy minimum in the region of reactants in the ground state. Moreover in that work, they showed that the first singlet excited state has a deep minimum in the region of photo-products and a shallow minimum in the area of reactants, with an effective energy barrier value of only 0.8 kcal mol^{-1}. Their study provided a very accurate theory level, but, because of the expensive computational cost required, they could not provide the dynamical protein effects on a geometrical constrained system, that can be very important.

Dealing with non-equilibrium processes triggered by photoexcitation should be very complex, above all after an excitation into a π π^* state that could be coupled with thermal motions. I.e. the out-of-plane chromophore modes may dramatically modify the electronic states layout, with subsequent effects on PES and (de)activation pathways that have to be taken into account [144]. To find a balanced, accurate, and less expensive theory level for the electronic description and preserve the realistic modeling of the dynamical process is mandatory.

For the previous mentioned reasons, we simulated first the intrinsic reaction path of the GFP proton transfer in both the ground S_0 and first singlet excited S_1 state, and after an ab initio MD on a complete protein model, both by using the density functional theory. We first adopted a convenient, and still computational affordable, model of GFP including most of energetic and conformational effects of the protein on the proton transfer reaction. On this model the Intrinsic Reaction Coordinate (IRC) [145; 146] was integrated from transition states to reactants and products by the Dumped Velocity Verlet (DVV) integration algorithm.[36] The reaction path

has been investigated both in the ground and in first singlet excited electronic state, difining the PES by (TD)-DFT. In the Section 2.1, we demonstrated that a given level the TD-DFT describes at the same accuracy (systematic error) the S_1 PES of the $HBDI^-$ in several environments.[34]

At variance of what previously predicted,[39] we found a finite barrier of the PT in both the ground and the excited state. In particular, in both the electronic states the reactants correspond to well-defined minima of corresponding PES. The two structures significantly differ in both the chromophore and the molecular surrounding, suggesting that after the excitation the system can partly re-arrange moving from the Franck Condon region toward a stable minimum. Therefore, we support the experimental evidence of an important intermediate preceding the appearance of the proton transfer product in VIS\midIR pum probe records. [142] As expected, the process is favored in the excited state. Morover, it follows a concerted but asynchronous mechanism starting in proximity of the Glu222 residue rather than of the chromophore. Thus, we confirm that the excitation favors the proton transfer mostly for changes in the position of protons in the H-bond network rather than for an increased HBDI photo-acidity. The excitation converts a short ionic to a low barrier hydrogen bond network. However, this conversion is strongly modulated by the residues (His148, Ser65) surrounding the chromophore.

Because our minimal PT models still lack of the complete protein matrix effects on the energetic and dynamics, we also performed an ab initio molecular dynamics study. This time we chose and modeled a starting configuration representing the A

GFP form. This is very important to have a fair comparison with the experiments, because the previous minimal model can hardly distinguish between the different protein conformations, even if it still described the two different protonation states. So we followed the evolution of the system in both the ground and the excited state, thanks to an accurate MD study. The dynamics results have been also reproduced by using another starting reference structure, proving the two main results: the out-of-plane chromophore modes may dramatically modify the electronic states layout and the GFP environment provides a directional coordinate for the ultra-fast proton transfer reaction. In the end, an energetic scan and a normal modes analysis (on two smallest and more computational affordable models) have been shown to sustain further our hypothesis.

2.2.1 Methods and models

All the calculations, when not differently specified, were carried out by using the B3LYP [71] density functional and the 6-31+G(d,p) basis set, in both the time independent and TD-DFT formalism [111–113; 147], this latter to model the vertical $S_1 \leftarrow S_0$ transition energy. The Gaussian [82] suite of programs was used for all calculations.

2.2.1.1 Minimal PT model

As preliminary step of our study we considered the GFP model of the protein optimized by ONIOM [124; 125] at DFT and TD-DFT for the characterization of the S_0 and S_1 electronic states, respectively. Details of the obtained protein minimum are given in the previous Section 2.1.1. From this structure, we extracted a minimal PT protein model, hereafter referred to as A (See Figure 2.8). This includes the chromophore, the water25, and the residues Ser65, Ser205 (modelled by a methanol molecule), and Glu222 (modelled by an acetate ion). We considered two others models for an energetic analysis of the stationary points. The first, hereafter referred to as B, can be obtained from A by including also the His148 residue in the protein-like arrangement. The second, hereafter referred to as C, can be obtained from A by eliminating the Ser65. A TS structure was fully optimized for the model A in the S_0 state. In order to check the nature of the stationary points and the effective reaction vector involving the proton transfer, all force constants and the resulting vibrational frequencies have been evaluated (data not shown). In particular a nega-

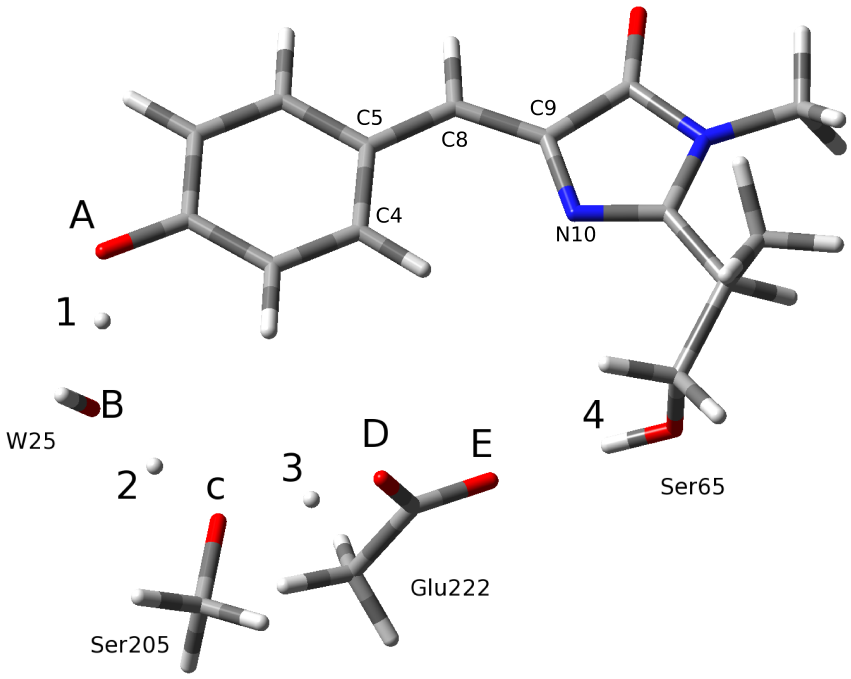

Fig. 2.8: Schematic proton transfer model compound A, representation consisting of the chromophore, water25, Ser205 and Glu222 and Ser65.

tive frequency of -276.6 cm^{-1} was found, corresponding to a collective stretching of all protons of the wire, as shown in Figure 2.10. No chromophore twisting or ring modes are involved in this coordinate, while a partial contribution of the side chain of Ser65 seems to be important. Further details regarding the TS of model A in the ground state are given in Section 2.2.2.2.

Regarding the PES of the first excited state, S_1, a full optimisation of TS for model A could not be possible, because a full relaxing of the structure leads to a twisting motion of the two rings in the HBDI molecule and a consequent interconversion to a dark state. Therefore, we first performed a given number of cycles of

the TS full optimization in order to obtain a partial relaxation of the model coordinates. Then, this job was stopped and re-started by introducing constraints in the structure. More specifically, all atoms were frozen except the oxygen and hydrogen atoms directly involved in the proton transfer and the Ser65 side chain atoms. The adopted constraints are graphically shown in Figure 2.9, where the fixed atoms are red colored, while the unconstrained ones are in green. The TS optimized structure was analyzed by calculation of all the force constants and the vibrational frequencies (data not shown). In particular a negative frequency of -619.04 cm^{-1} was found, corresponding to a collective stretching of all protons of the wire, as shown in Figure 2.11. Starting from the calculated TS structures, an intrinsic reaction coordinate was integrated in both the forward and the backward directions for both the ground and excited electronic states. As integrator, we adopted the DVV algorithm.[36] By controlling the magnitude of the velocity vector at every step along the path, it is possible to make the DVV trajectory approach the IRC path within a chosen tolerance. Each DVV step is composed of three part: the propagation of atomic positions and momenta, the momenta magnitude dumping (in order to avoid huge oscillations orthogonal the path) and finally the updating of the magnitude step. In this latter step the discrepancy between the DVV and the IRC path is evaluated and kept within an error tolerance criterium.

As limits of the two paths calculated in the S_0 and S_1 states, we obtained structures corresponding to the reactant (R) configuration, characterized by a neutral chromophore, and to the product (P) configuration, characterized by an anionic

Fig. 2.9: S_1 schematic proton transfer constrained scheme for the model compound A. The atom in red are completely frozen during the optimisation, while the green one are full free.

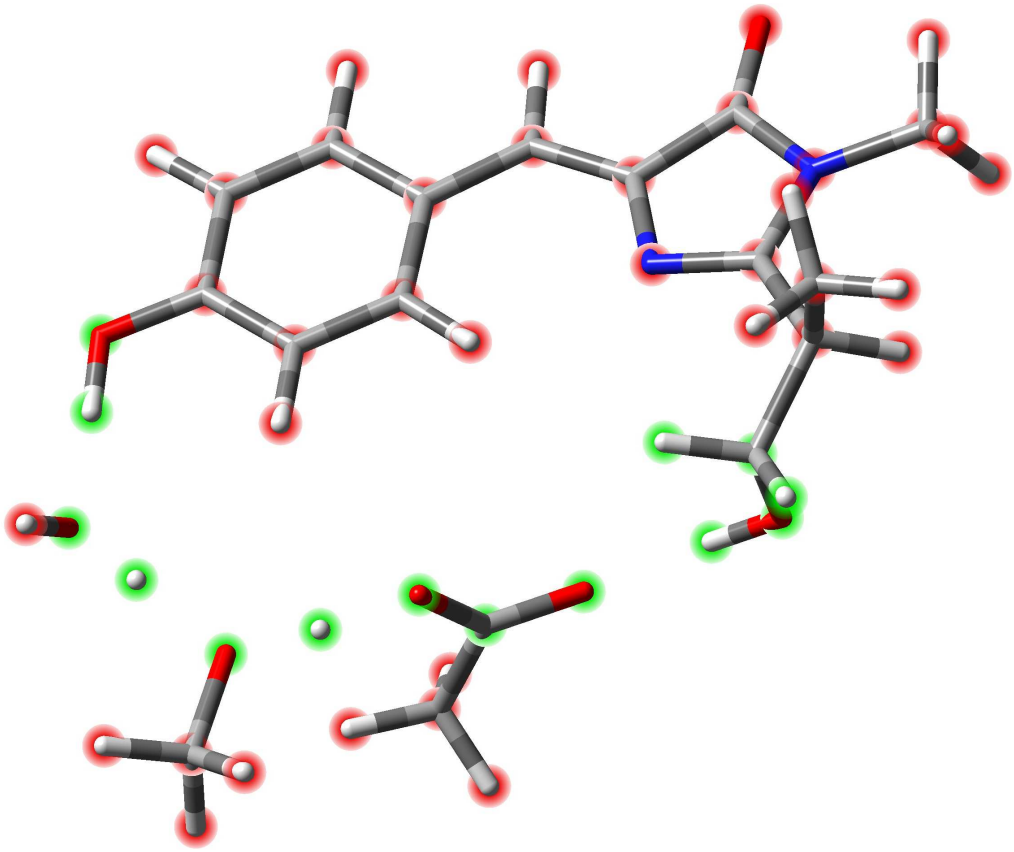

chromophore. In both the electronic states, the R and P structures were considered for a further optimization in order to locate the stationary points on the corresponding PES. It is important to underline that both the S_0 and S_1 IRC calculations have been performed without any constraints, following only the reaction vectors from the corresponding TS structure. Energetic analyses, including a NPA charges, were performed on the stationary points obtained for the GFP model A, and for corresponding structures of models B and C.

2.2.1.2 Ab initio molecular dynamics and wt-GFP A form model

The PT reaction has been studied by choosing a reliable model for the neutral starting wt-GFP A form to be followed during the reaction in both the electronic states. We started from the crystallographic structure of wild type GFP of jellyfish *Aequorea Victoria* (PDB code 1GFL) [148] for the modeling. The same procedure presented in Section 2.1.1.2 has been used for the protonation procedure and for the ONIOM PI partition scheme (the smallest one). The starting conformation (namely A_1^P), used for MD, has been obtained by several optimization steps. First the aqueous solvent was treated implicitly by the so-called ONIOM\C-PCM-X [126; 127] scheme, and after we relaxed the system by neglecting the implicit solvation effects in order to save time for the subsequently MD study. This approximation is valid, because we ensured that the implicit solvation did not affect to much the vertical excitation energy and also because our MD simulations were not long enough the inclusion of the volume preserving effects of implicit solvation to be needed.

Ab-initio molecular dynamics simulations, employing the Born-Oppenhaimer approximation (BO)[76–79] MD, have been performed in order to characterize the system in the ground state. We collected a trajectory on the S_0 potential energy surface for 3 ps, employing a time step of 0.5 fs. The starting configuration has been previous described as A_1^P and starting randomly chosen momenta have been used, by preserving a starting average temperature of 298 K.

The first singlet excited state ab-initio BO MDs simulations (S_1) have been performed extracting both starting points from the ground state simulation (namely

A_2^P, with the respective momenta) and also from the gas phase optimization (the previous described A_1^P, with the randomly chosen momenta). The excited state energies and gradients were calculated on the fly by the linear response TD-DFT formalism [80; 81]. We collected both dynamics for less then 1ps, but both are long enough to observe the ESPT process, employing a time step of 0.5 fs. The excited state MD have been performed employing the CAM-B3LYP [122] functional with 6-31+G(d,p) basis set.

2.2.1.3 Energetic analysis

Rigid scans of the gas-phase minimum $HBDI^-$ chromophore in both ground and excited states have been performed by changing the choromphore N-C-C-C dihedral angle in order to explore a range from -30 to +30 degrees. The scans have been performed at B3LYP and TD-CAM-B3LYP, with 6-31+G(d,p) basis set, for S_0 and S_1, respectively.

2.2.2 Results and discussion

2.2.2.1 PT models structural analysis

In our reference cluster model has been also included the effect of the Ser65, that is not directly involved in the proton transfer. In order to monitor the degree of asynchronicity, we define the position asymmetry coordinate δ_i (as in Ref. [39]) for each event i of the whole reaction, more precisely for the HBDI-Wat25 (i=1), the Wat25-Ser205 (i=2), and the Ser205-Glu222 (i=3) proton transfer, respectively. The δ_i coordinate can be expressed as follows:

$$\delta_1 = R_{A1} - R_{1B}$$
$$\delta_2 = R_{B2} - R_{2C}$$
$$\delta_3 = R_{C3} - R_{3D}$$

where Rs are hydrogen bond distances indicated according to labels of Figure 2.8. Please note that when δ_i is equal to zero the ith proton is exactly in the middle of the hydrogen bond. When the δ_i value is negative the ith proton is closer to the hydrogen bond donor (proton transfer reactant-like). Finally, when δ_i is positive,the ith proton is closer to the hydrogen bond acceptor (proton transfer product-like).

In Figure 2.7 all the the δ_i values relative to all stationary structures have been reported. By the inspection of these δ_i values is clear how the TS structure represents an intermediate structure between the R and the P states for both the electronic states. It also clear that the mechanism appears concerted and there is a neat shortening of whole H-bond distances in the TS structures. In the Figure 2.8 the distances between the three oxygen-Donor and the oxygen-Acceptor atoms have been reported for all three proton chain involved in the proton transfer reaction.

The S_1-R presents a ~ 0.1 Å shortening for all the oxygen-oxygen distances respect to S_0-R (see the Figure 2.8). Moreover the S_1-R δ_i values are less negative respect to the corresponding S_0-R one. These data supported the possible scenario suggested in the study of Di Donato et al. [142] in which the GFP proton transfer pathway presents an excited state intermediate in which the proton distances are partially adjusted respect to the S_0-R ones.

Table 2.7: Structural parameters (Å) for the stationary points of the GFP model A

	R_{A1}	R_{1B}	R_{B2}	R_{2C}	R_{C3}	R_{3D}	δ_1	δ_2	δ_3
S_0-R	0.992	1.729	1.005	1.630	1.035	1.502	-0.737	-0.625	-0.467
S_0-TS	1.074	1.406	1.295	1.135	1.470	1.047	-0.332	0.160	0.423
S_0-P	1.483	1.045	1.627	1.005	1.651	1.003	0.438	0.622	0.648
S_1-R	1.004	1.602	1.017	1.522	1.068	1.399	-0.598	-0.505	-0.331
S_1-TS	1.078	1.391	1.214	1.200	1.407	1.066	-0.313	0.014	0.341
S_1-P	1.462	1.048	1.552	1.014	1.592	1.005	0.414	0.538	0.587

Table 2.8: $HBDI^-$ Structural parameters of the GFP model A stationary points (Å and Degree)

	R_{AB}	R_{BC}	R_{CD}	ω_{ABCD}	α_{C5C8C9}
S_0-R	2.720	2.634	2.535	-47.71	128.91
S_0-TS	2.480	2.429	2.515	-27.65	129.84
S_0-P	2.525	2.628	2.643	-12.05	130.66
S_1-R	2.600	2.530	2.466	8.14	128.79
S_1-TS	2.466	2.413	2.472	12.86	128.95
S_1-P	2.501	2.566	2.597	6.81	128.11

All the three structures in the S_1 state seem to be more shrunk in order to facilitate the proton transfer, as it can be observed by narrower values of α_{C5C8C9} angle assumed in all the S_1 structures. Furthermore, the oxygen atoms involved in the proton transfer are more planar in the excited state, as it can be observed by the ω_{ABCD} dihedral value.

In the Figure 2.9 we also monitor other structural parameters not directly involved in the proton transfer. These are the distance between the Glu222 oxygen atom (O-E) and the Ser65 hydrogen atom, R_{E4}, the C-O distance of the Tyr66 (R_{COph}) and of imidazole (R_{COim}), and the dihedral angles accounting for the planarity of the chromophore ($\tau_{N10C9C8C5}$ and $\phi_{C9C8C5C4}$, see Figure 2.8 for labels). The explicit evaluation of the Ser65 effects on the structures are mandatory. By

Table 2.9: $HBDI^-$ Structural parameters of the stationary points (Å and Degree)

	R_{E4}	R_{COph}	R_{COim}	$\tau_{N10C9C8C5}$	$\phi_{C9C8C5C4}$
S_0-R	1.708	1.352	1.232	-3.39	-7.66
S_0-TS	1.835	1.325	1.233	-2.22	-1.10
S_0-P	1.873	1.289	1.237	-0.97	2.18
S_1-R	1.695	1.344	1.244	-1.61	-2.98
S_1-TS	1.785	1.326	1.245	-0.65	-3.62
S_1-P	1.820	1.294	1.244	-0.01	-3.45

the inspection of the R_{E4} distances in all structures emerged that the electrostatic interactions of this residue on the Glu222 are very important as witnessed by the elongation of this distance during the proton transfer in order to easier accommodate the less negative charge localised on Glu222 in the products respect to the reactants (see the first column of Table 2.9).

From Table 2.8 and 2.9 we observe that in both the electronic states, the proton transfer affects the R_{COph} distance in a similar manner. On the contrary, the imidazole group is more involved by the electronic excitation, as we can infer by the longer R_{COim} distances in all the S_1 structures. Moreover, by the inspection of the $\tau_{N10C9C8C5}$ and $\phi_{C9C8C5C4}$ dihedrals we note that the electronic excitation affects the the so-called bridge region of the chromophore (C5-C8-C9 group) in a significant

way. This result suggests an important role played by the protein as a structural constraint on these degrees of freedom in both the energetic and the mechanism of the proton transfer.

2.2.2.2 The PT model transition state

Fig. 2.10: S_0 TS reaction vector representing proton transfer reaction in the electronic ground state. Relative frequency are obtained at B3LYP\6-31+G(d,p) level.

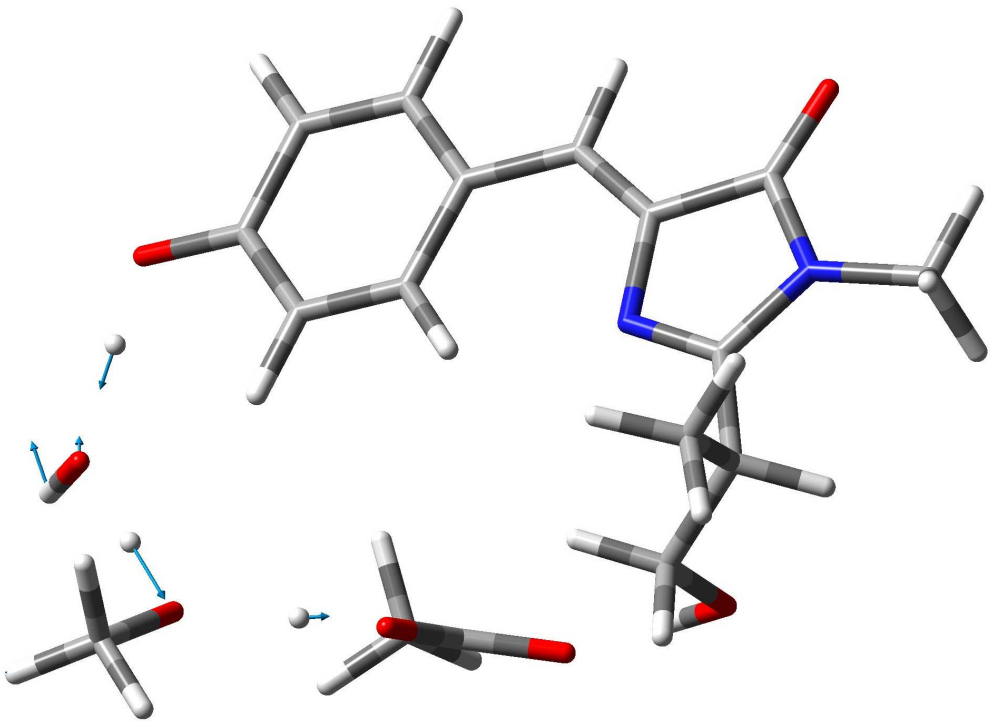

Regarding the TS of the PES in the ground state, S_0, we report it in Figure 2.10. The TS structure seems to prepare the hydrogen shuttle. All the oxygen distances involved in the wire are shrunk in respect to the reactants and products (see Table 2.8), in order to make easier the hydrogen hopping. At same time the wire is not so

symmetric. By the inspection of the δ_i values is clear that the TS looks like more similar to the products, even if the first hydrogen atom in the wire (Cro-Wat) is still attached in a reactants like arrangement. By the inspection of the δ_2 (Wat25-Ser205), and the δ_3 (Ser205-Glu222) the positive values witness the products like shape. The negative frequency of -276.6 cm^{-1} is found corresponding to the S_0 IRC. The main contribution to reaction coordinate is due to a collective and concerted stretching of all protons of the wire, as can be seen by the vectors belonging to hydrogen atoms of the wire (Cro-Wat25-Ser205-Glu222). Another contribution of a water25 libration like mode seems to affect also the reaction coordinates. Neither twisting and rings chromophore modes are involved. By a magnification of the displacement reaction vectors starts to appear a contribution of the Ser65 side-chain in the reaction coordinate. Regarding the TS of the PES in the excited state, S_1, we report it in Figure 2.11. As in the S_0, the TS structure seems to prepare the hydrogen shuttle. All the oxygen distances involved in the wire are shrunk in respect to the reactants and products (see Figure 2.8), but also respect to the corresponding S_0 TS structure. Moreover this time all the wire network is in a very planar arrangement as we can see by the inspection of the ω_{ABCD} dihedral value in Table 2.8. The wire seems also to be more symmetric by the inspection of absolute δ_1 and δ_3 values and the near zero δ_2 value. On this final structure all force constants and the resulting vibrational frequencies have been evaluated (data not shown). In particular a negative frequency of -619.04 cm^{-1} was found, corresponding to a collective stretching of all protons of the wire, as shown in Figure 2.11. The main contribution to reaction coordinate,

Fig. 2.11: S_1 TS reaction vector representing proton transfer reaction in the first singlet electronic state. Relative frequency are obtained at TD-B3LYP\6-31+G(d,p) level.

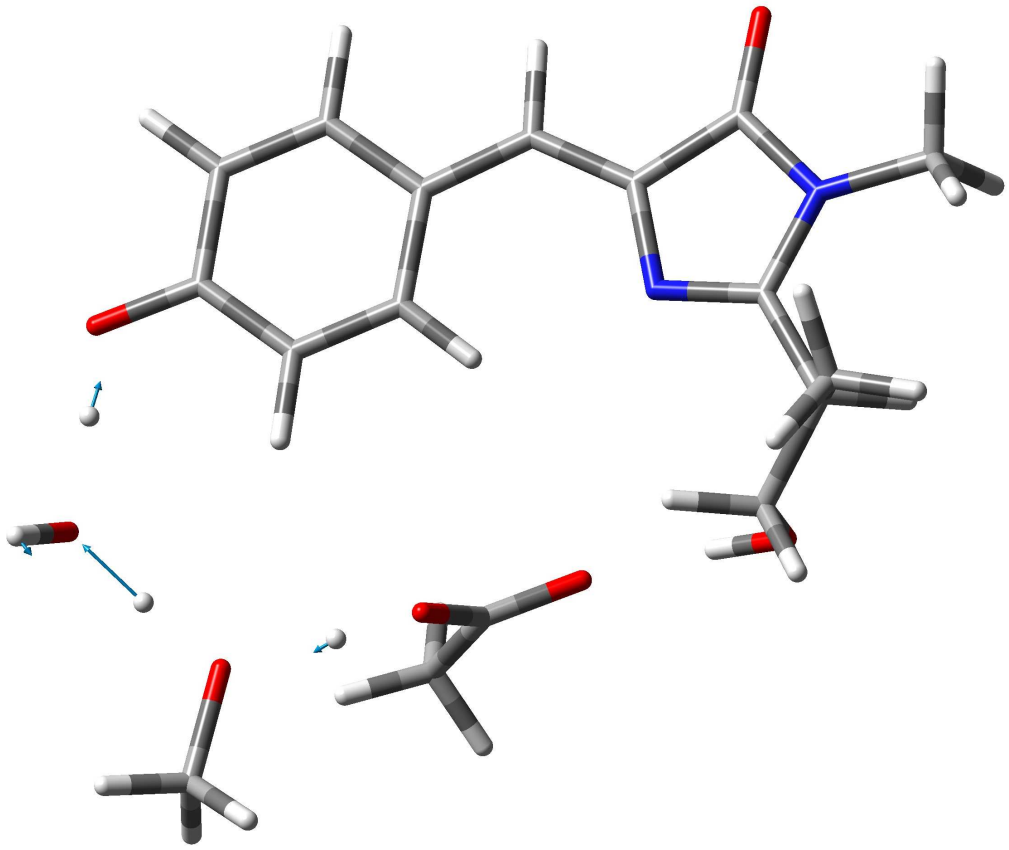

as before, is due to a collective and concerted stretching of all protons of the wire, as can be seen by the vectors belonging to hydrogen atoms of the wire (Cro-Wat25-Ser205-Glu222). Another contribution of a water25 libration like modes seems to affect also the reaction coordinates. By the inspection of other weaker negative frequencies, twisting and rings motions appear, leading to the interconversion to a dark state.

Even if the two IRC vectors seems to be very similar each other, the excited

state shrunk oxygen wire distances and their more planar arrangement, combined to a more symmetric proton distribution in S_1 TS, explain the low barrier activation energy in the S_1 rather then in S_0; see next section for further discussion.

2.2.2.3 The IRC proton shuttle mechanism

Fig. 2.12: IRC Energy profile (full black line) representing proton transfer reaction in the electronic ground state, The reactants and products energies are also reported (x symbols). Relative energies in kcal\mol are obtained at B3LYP\6-31+G(d,p) level.

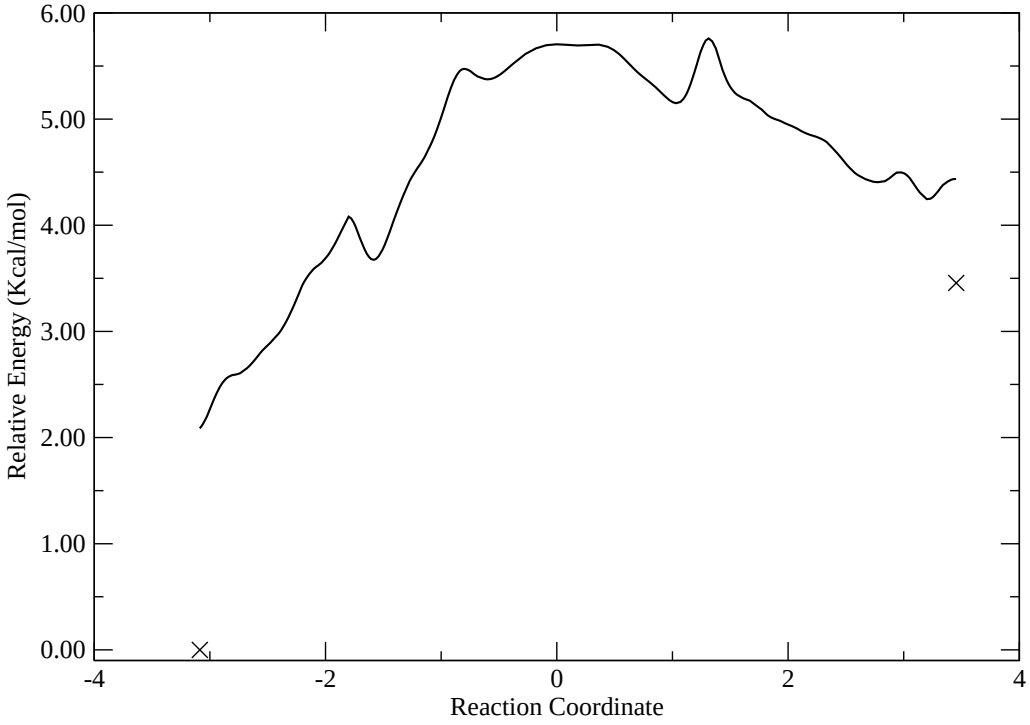

We followed the proton transfer reaction by integrating the intrinsic reaction coordinate for the GFP model A, on both the S_0 and S_1 potential energy surfaces. The initial geometry has been that of the optimized transition state, and the path has been integrated in both directions from that point. In Figure 2.12 we present the IRC

Fig. 2.13: IRC position asymmetry coordinate δ_i evolution representing proton transfer path in the electronic ground state (upper panel) and normalised one (lower panel). The δ_1 (Cro-Wat), δ_2 (Wat-Ser), and δ_3 (Ser-Glu) are plotted in full , dashed, and dotted lines respectively. The reactants and products δ_1 (Cro-Wat), δ_2 (Wat-Ser), and δ_3 (Ser-Glu) are also reported (x, circle, and star symbols respectively)

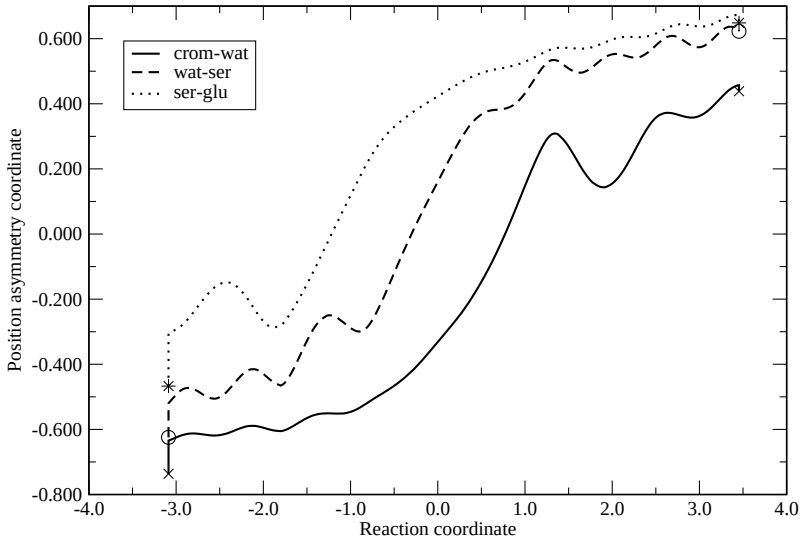

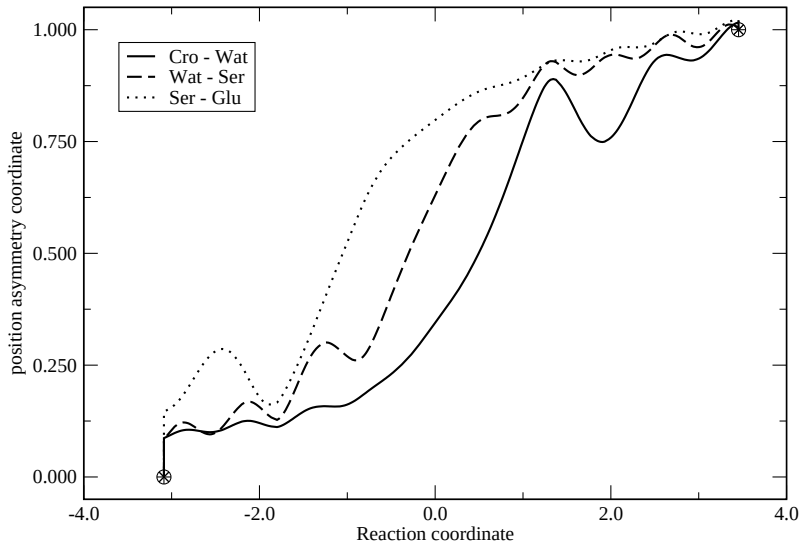

energy profile relative to the reactant energy in the electronic ground state. It can be observed a smooth energy profile, characterized by one maximum located at TS (reaction coordinate= 0), with an activation energy of 5.70 kcal\mol. The product is 3.5 kcal\mol higher in respect to the reactant (see Figure 2.10). In Figure 2.13 we plot the evolution of the three position asymmetry coordinates δ_i during the IRC. The coordinates have been also normalized, going from 0 (the reactant) to 1 (the product), and represent in percentage the progress of the proton transfer. In spite of different oxygen-oxygen distances for each proton transfer event (see Figure 2.8), the evolution of the three δ_i values suggests a synchronous and concerted mechanism. In fact, the three values of δ_i change simultaneously and become positive in proximity of the TS structure (Reaction coordinate= 0). In Figure 2.14 we present the IRC

Table 2.10: $HBDI^-$ (TD)-B3LYP\6-31+G(d,p) electronic activation energy (Ea) and electronic energetic difference between the products and reactants ($\Delta E(P-R)$). The values are in kcal\mol.

	Ea	$\Delta E(P-R)$
$E_{elect}(S_0)$ A	5.704	3.456
$E_{elect}(S_0)$ B	2.990	-1.308
$E_{elect}(S_0)$ C	0.878	-2.529
$E_{elect}(S_1)$ A	4.081	-0.051
$E_{elect}(S_1)$ B	2.968	-3.208
$E_{elect}(S_1)$ C	0.355	-4.504

energy profile relative to the reactant in the first singlet electronic excited state. In Figure 2.15 we plot the evolution of the three position asymmetry coordinates δ_i during the IRC. In S_1 we observe an energy profile rougher than the corresponding in S_0, characterized by the maximum located at TS, and an activation energy of 4.08 kcal\mol ($\sim$ 1.5 kcal\mol lower than Ea found in S_0). At variance with the ground

Fig. 2.14: IRC Energy profile representing proton transfer reaction in the first singlet excited electronic state. The reactants and products energies are also reported (x symbols). Relative energies in kcal\mol are obtained at TD-B3LYP\6-31+G(d,p) level.

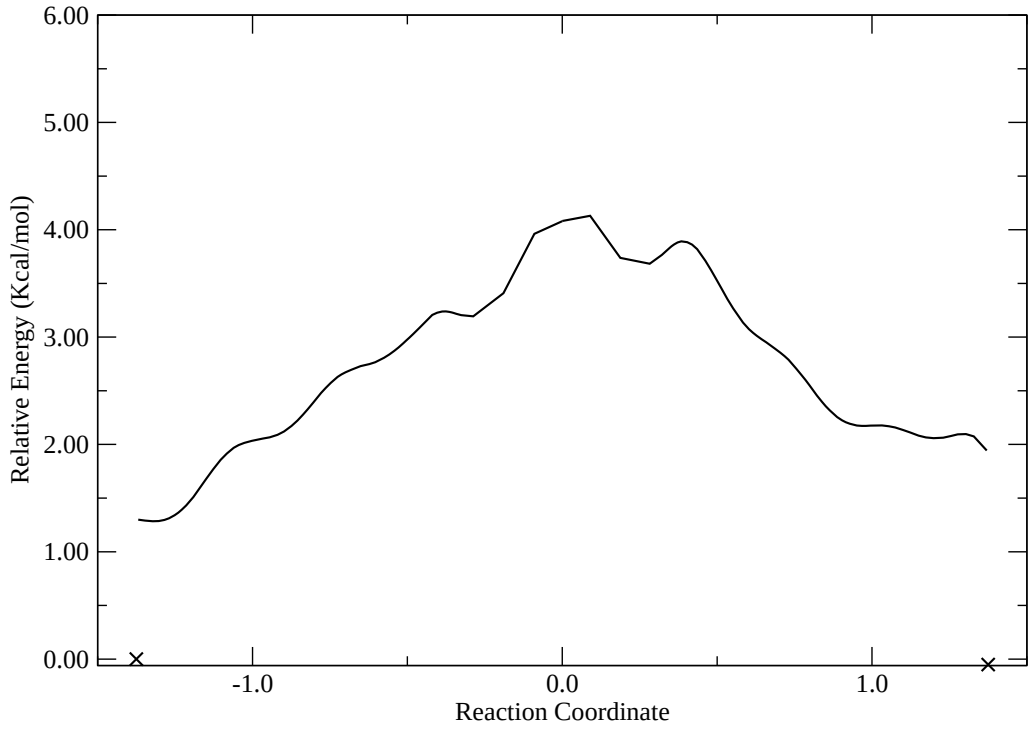

state reaction, the product is about iso-energetic with the reactant in S_1. Therefore, the whole reaction is more favored in the excited state. The ESPT reaction seems to start from an initial configuration in which the network is already arranged for the proton movements, more than in the ground state. In fact from Figure 2.15 we observe that the reaction appears to be concerted, but the three proton movements are asynchronous, unlike the reaction in S_0. For example the value of δ_3, associated with the proton transfer from Ser205 to Glu222, is the first to become positive, while the other two values remain negative until the proximity of the TS structure. The S_1-

Fig. 2.15: IRC position asymmetry coordinate δ_i evolution representing proton transfer path in the first singlet excited electronic state (upper panel) and normalised one (lower panel). The δ_1 (Cro-Wat), δ_2 (Wat-Ser), and δ_3 (Ser-Glu) are plotted in full , dashed, and dotted lines respectively. The reactants and products δ_1 (Cro-Wat), δ_2 (Wat-Ser), and δ_3 (Ser-Glu) are also reported (x, circle, and star symbols respectively)

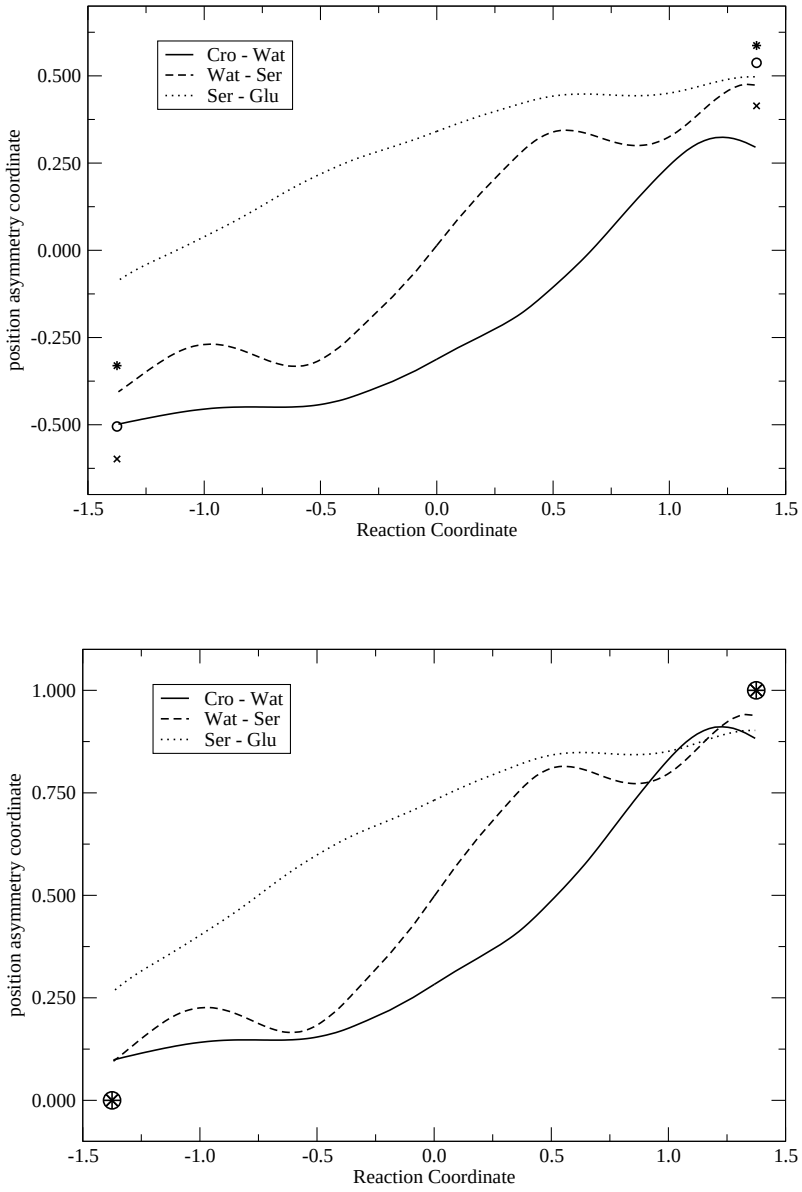

R δ_i values can suggest that the first event after the excitation is the reorganization of the hydrogen network, instead of the de-protonation of the chromophore. So after the intitial network adjustment, the new S_1-R could favour the proton release, as witnessed by the lower energy barrier for ESPT. This means that the excited state proton transfer mechanism is driven by the intitial network re-organization in spite of the idea that the driving force has been represented by a suddenly proton detachment from the chromophore upon the excitation.

Moreover, the analysis of the position asymmetry coordinate parameter for each of the three protons in the proton wire along the reaction pathway in both the electronics states reveals that the movement of the protons is attributable to a concerted\synchronous mechanism. All protons move simultaneously with just a single barrier (or, transition state) governing the kinetics. In previous studies of Wang and coworkers [37; 38] the mechanism does not present a single barrier. The single barrier process in excited state has been already mentioned in high level post Hartree-Fock study of Vendrell et al. [39], but they found a different pathway in the ground state, probably because of their planar constrained HBDI geometry of their model compound.

2.2.2.4 The IRC PT Energy analysis

In Figure 2.10 we reported the electronic activation energy (Ea) in kcal\mol for the proton transfer in the gas phase. The relative energies for all models in the ground and excited electronic states are also represented in Figure 2.16 . By the inspection of Figure 2.10 we note that the barrier is higher for model A (5.70 and 4.08 kcal\mol

Fig. 2.16: Schematic energy profiles representing proton transfer reaction. Relative energies in kcal\mol are obtained at B3LYP\6-31+G(d,p) level.

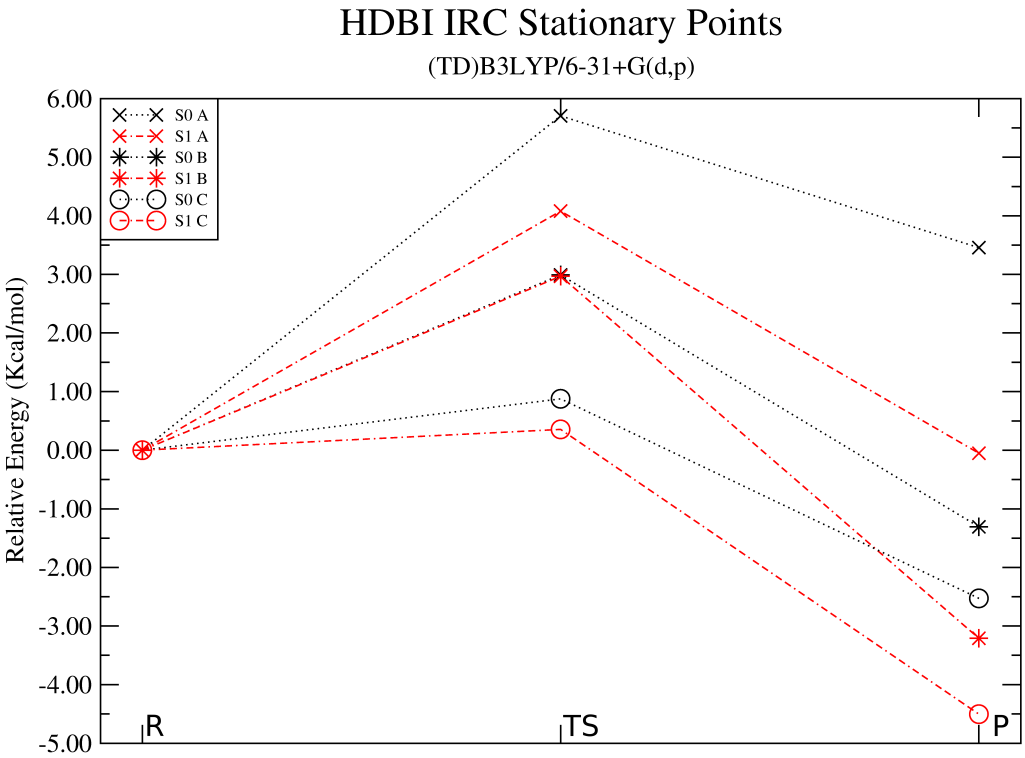

in the S_0 and S_1 state, respectively), while the process is favored by including the effects of His145 (2.99 and 2.97 kcal\mol), or by eliminating the electrostatic effects of Ser65 (0.88 and 0.35 kcal\mol). It is noteworthy that the model B model shows the same activation energy in both the electronic states, while the barrier is lower in the S_1 electronic state for model A and model C systems. In the second column of Table 2.10 the difference between the products and reactants energy ($\Delta E(P-R)$) is reported in kcal\mol. In particular for the model A system, in S_0 the product is less favored of 3.5 kcal\mol, while in S_1 the product and reactant become iso-energetic (ΔE =-0.05 kcal\mol). In Table 2.11 the stationary points energies relative to the ground state reactants one are also reported for each model system in eV.

Table 2.11: $HBDI^-$ (TD)-B3LYP\6-31+G(d,p) stationary points relative energies for each model system. The values are in Kcal\mol.

	A	B	C
S_0-R	0.00	0.000	0.000
S_0-TS	5.70	2.99	0.88
S_0-P	3.46	-1.31	-2.53
S_1-R	80.55	80.57	76.88
S_1-TS	84.63	83.52	77.23
S_1-P	80.50	77.37	72.36

2.2.2.5 The PT molecular dynamics

Analysis of structural quantities belonging to the chromophore and to the hydrogen bond network in both ground and excited state trajectories is performed in order to investigate the protein matrix role in the ESPT reaction.

In spite of the short time of sampling, collective modes involving the chromophore and the hydrogen bond network are monitored as values adopting periodic oscillations around well defined minima.

In Figure 2.17 (left panel) we show the distributions of inter-molecular distances of oxygens belonging to the hydrogen bond network obtained from a 3 ps ground state *ab-initio* molecular dynamics simulation. The Otyr-Owat, Owat-Oser205, Oser205-Oglu222 normalized pair distances distribution are shown, along with the relative averages made every 50 points (colored curves).

By an inspection of these distributions, it is evident that the pair Oser205-Oglu222 distance present the most regular shape. During the simulation Oser205-Oglu222 distance oscillations explore a range of values extending from a minimum of 2.313 Å to a maximum of 2.761 Å, reached only once in the whole simulation. The

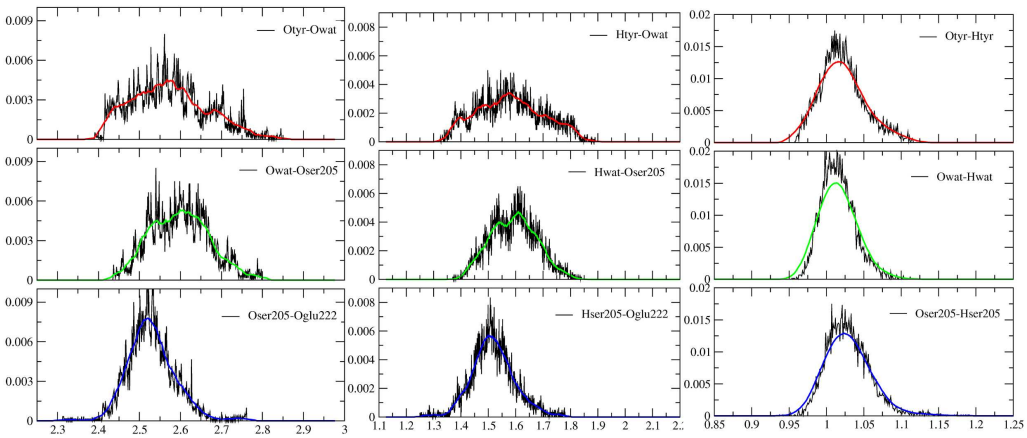

Fig. 2.17: Normalized distributions of network distances (Å) involved in the PT network obtained from S_0 BOMD simulation at B3LYP\6-31+g(d,p) level of theory. Left, Oxygen-Oxygen distances:Otyr-Owat (up), Owat-Oser205 (middle), Oser-Oglu(down). Middle, Proton-Acceptor units distances: Htyr-Owat (up), Hwat-Oser205 (middle), Hser-Oglu(down). Right, Proton-Donor units distances: Otyr-Htyr (up), Owat-Hwat (middle), Oser205-Hser205 (down). The relative average values, made every 50 points, are shown by different colored curves.

average distance value is around 2.530 Å with a standard deviation of 0.059. This average distance value extracted from the simulation is so close to the maximum value of the distribution that is indeed peaked around 2.522 Å. The distribution in terms of both shape and maximum peak confirms an almost regular oscillation trend. For the whole trajectory this oxygen pairs generally maintain the same distances range. A more complex behavior is observed for Otyr-Owat, indeed these oxygens explore wider distance ranges and less regular, compared to the Oser205-Oglu222 pair. Oscillations reach distances ranging from 2.391 to 2.845 Å, the average distance value is 2.574 Å with a standard deviation of 0.092. This trend is also supported by the corresponding shape, that is wide, and the actual main peak cannot be defined. The Owat-Oser205 pair explores values ranging between 2.436 and 2.797 Å , the average distance value is around 2.599 Å with a standard deviation of 0.071. As observed

in the Otyr-Owat distribution, an irregular shape is found, although it explores a shorter range of values. The peculiar differences shown in the distributions are in perfect agreement with the relative distance oscillation trends. These ones reflect a major rigidity of the Oser205-Oglu222 interaction that is not observed in the other two cases. This fact could be related to a major mobility freedom of the water molecule in both the Otyr-Owat and Owat-Oser205 pairs and in particular in the Otyr-Owat case. In Figure 2.17 (middle panel) we show the proton acceptor distance distributions obtained from the 3 ps ground state simulations. The acceptor pairs include Htyr-Owat, Hwat-Oser205 and Hser205-Oglu222 distances. Observing the distributions it is evident a similarity with the oxygens distributions shown before. From our analysis, we see that Htyr-Owat ground state oscillations are pent to values higher that 1.4 Å. The maximum value is 1.890 Å , the minimum one is 1.324 Å, and the average distance value is 1.581 Å, with a standard deviation of 0.120. The distribution reflects a trend with no regular oscillations and with a wide range of explored values. It appears spread and without a well-defined maximum peak. In the Hwat-Oser205 case generally a more regular trend is observed during the simulation with oscillations on average around 1.593 Å and a standard deviation of 0.084. The maximum distance value is 1.840 Å, while the minimum one is 1.370 Å. The relative distribution appears narrower than the previous one confirming a more regular oscillation trend, although also this time it is not trivial to define a main peak in the distribution. The last monitored distance, Hser205-Oglu222, confirms the stiff nature of these residues interaction. It spans from 1.253 to 1.780 Å values,

with an average around 1.518 Å, and shows a standard deviation of 0.078. The distribution is well-centered around a distance value (1.507 Å) that is not so different from the calculated average value from the simulation. Moreover the shape is the most regular among the three distributions.

From these results it is evident that the residues Ser205 and Glu222 are closer than the other two pairs, as shown by the shift toward shorter distances of their distribution in respect to the others. The well-defined structural arrangement of Ser205 and Glu222 is almost preserved during the simulation, confirming in this way a retained rigidity between these residues that is not present in the other two cases, as already observed for the oxygens analysis.

In Figure 2.17 (right), we report the distributions of the proton donor distances from the 3 ps ground state simulation. The investigated intramolecular distances are: Otyr-Htyr, Owat-Hwat and Oser205-Hser205. Really tight oscillations and values typical of bond distances are observed in the ground state. These regular trends are in agreement with the fact that these are bond distances and again it suggests that we are dealing with a system that has no driving forces to react. For the intramolecular bond distance Otyr-Htyr, we have a maximum value of 1.116 Å and a minimum one of 0.958 Å. The average distance value is 1.021 Å with a standard deviation of 0.030. The bonded nature is confirmed by a regular shape of the distribution with a maximum peak around 1.015 Å. Regarding the Owat-Hwat distance, we obtain a trend that shows a maximum distance value of 1.112 Å, a minimum value of 0.954 Å, and an average value 1.016 Å, with a standard deviation

of 0.022. Also this time the distribution reflects an almost regular oscillation trend. It shows a regular gaussian shape with a maximum at about 1.012 Å, also this time not so different from the average distance value. The pair Oser205-Hser205 explores ranges between a maximum at 1.190 Å and a minimum at 0.937 Å. The average distance value is 1.029 Å with a standard deviation of 0.030. A regular distribution is observed also this time in agreement with the bond nature of the examinated distances.

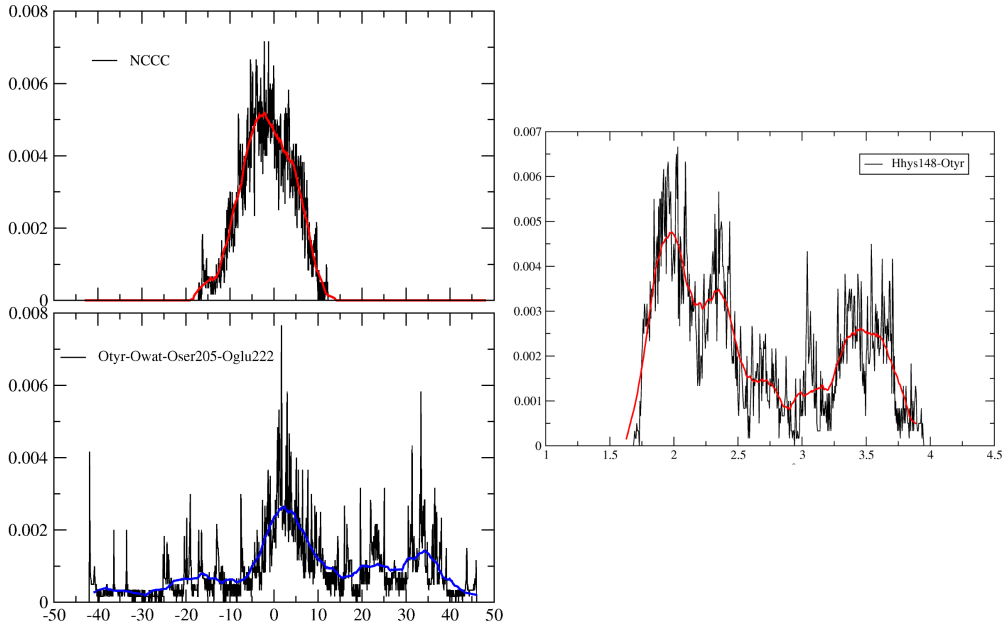

Fig. 2.18: Normalized distributions of distances (Å) and dihedral (degree) angles obtained from S_0 BOMD simulation at B3LYP\6-31+g(d,p) level of theory. The chromophore N-C-C-C dihedral angle (upper left) and the dihedral angle of oxygen atoms involved in the hydrogen bond network Otyr-Owat-Oser205-Oglu222 (lower left) are shown, respectively. The histidine148 Proton-OTyr pair distance distribution (right) is also shown. The relative average values, made every 50 points (and every 100 for the oxigens dihedral), are shown by different colored curves.

The chromophore N-C-C-C dihedral angle distribution is shown in Figure 2.18 (upper left). The dihedral angle values range from 12.19 to -17.06 degrees with an average value of -1.55 degrees and a standard deviation of 5.76. By an inspection of distribution, it is evident the small range of explored values and also a rather regular oscillation trend. These results suggest that in the ground state the preferred chromophore conformation predicts an average planar N-C-C-C dihedral angle conformation. Also the distribution of the dihedral angle concerning the oxygen atoms involved in the hydrogen bond network (Otyr-Owat-Oser205-Oglu222) is shown in Figure 2.18 (lower left). A generally not regular distribution is obtained. Although

the dihedral angle values are almost focused around 2.5 degrees, other populated regions are observed between -20 and -10 degrees and 20 and 40 degrees. These results show a general mobility of this dihedral angle in the ground state. This fact suggests that no peculiar behavior can be associated to this structural parameter. We will see how this behavior changes in the excited state and its probable crucial role in the ESPT reaction. A key residue although not directly involved in the PT network is histidine 148. We show in Figure 2.18 (righ), the distribution of the distance values between the histidine hydrogen, nearest to the tyrosine oxygen (the N_δ one), in the S_0 MD. The explored range of values is included between 1.692 and 3.943 Å, the average value is around 2.615 Å, with a standard deviation of 0.648. The distribution shows three mainly poulated regions: around 1.995, 2.358 and 3.476 Å. Among these, the first one is the most important thus suggesting that the interaction with the chromophore is quantitatively present during the simulation. However the not negligible presence of other populated regions at higher distance values let us think that the interaction is not constant during the simulation.

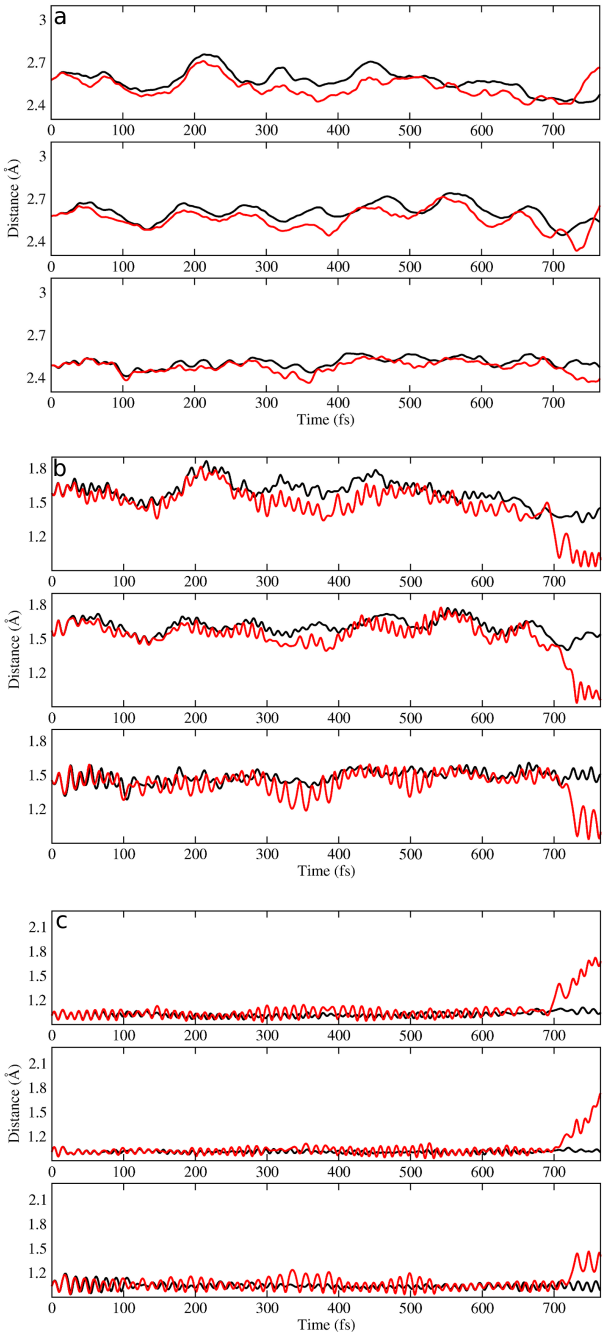

Fig. 2.19: Comparison of network distances (Å) evolution involved in the PT network obtained from B3LYP\6-31+g(d,p) S_0 BOMD (black) and TD-CAM-B3LYP\6-31+g(d,p) A_1^P S_1 BOMD (red). a)Oxygen-Oxygen distances:Otyr-Owat (up), Owat-Oser205 (middle), Oser-Oglu(down). b)Proton-Acceptor units distances: Htyr-Owat (up), Hwat-Oser205 (middle), Hser-Oglu (down). c)Proton-Donor units distances: Otyr-Htyr (up), Owat-Hwat (middle), Oser205-Hser205 (down).

We have monitored the evolution in the S_1 state of two different starting points,

according the procedure described in Section 2.2.1.2. Important rearrangement of the structural parameters are observed in both simulations, leading to the excited state proton in both cases with a concerted and almost synchronous mechanism. We first analyzed the A_1^P S_1 MD results, making a comparison with the first ps of the ground state simulation, in order to appreciate the trend differences. In Figure 2.19 a), we show the inter-molecular oxygen distances Otyr-Owat, Owat-Oser205 and Oser205-Oglu222. Irregular oscillations in the Otyr-Owat pair are observed and shorter distances (up to about 2.4 Å) are already explored during the simulation before the ESPT reaction. A different behavior compared to the ground state is observed on the S_1 PES for Owat-Oser205. Indeed, in this case the oscillation range is on average shifted to shorter distances with only a maximum reached value of 2.7 Å around 550 fs. Regarding the Oser205-Oglu222 pair dynamics, we observe some steps of the trajectory in which the two oxygen atoms approach closer, in particular around 100 and 350 fs. These results suggest that forces between the inter-molecular oxygen pairs are different and this fact influences the relative trends. Moreover in the excited state the inter-molecular distances are generally shorter than the ones in the ground state, suggesting that the system can be more suitable for the ESPT reaction.

In Figure 2.19 b), we show the acceptor distances, i.e. Htyr-Owat, Hwat-Oser205 and Hser205-Oglu222, in the excited state simulation in comparison with the ones from the first 1 ps of the ground state trajectory. A broad nature of oscillations is observed in all three cases and it is especially evident for Hser205-Oglu222 distance.

Regarding the Htyr-Owat dynamics, we observe a discrepancy between the S_1 and S_0 MD since 300fs. In the S_1, this distance seems to be shifted to shorter values, distances shorter than 1.4 Å are observed during the simulation indeed. The Hwat-Oser205 oscillation range is almost similar to the ground state one, but the intrinsic different nature of oscillations is evident. When we observe the Hser205-Oglu222 trend it is possible to clearly recognize an intrinsic broad oscillation nature that is mainly emphasized in 300-400 fs range and at 500 fs, with no correspondence in the ground state. This proton acceptor pair distances in the other A_2^P S_1 MD, (see Figure 2.21) still present different oscillations compared to S_0. It is especially evident that Htyr-Owat distance oscillates differently from the ground state one, oscillating around 1.6 Å distance value and then decreasing toward shorter values until the proton transfer event. The Hser205-Oglu222 trend shows oscillations similar to the ones observed in the previous A_1^P S_1 simulation.

In Figure 2.19 c), we show the proton donor distances S_0 and A_1^P S_1 comparison. As already done in the previous analysis, the investigated molecular distances are Otyr-Htyr, Owat-Hwat and Oser205-Hser205. Although in this case we deal with bond distances in the excited state, these seem less rigid. Therefore this weaker bond nature can help the ESPT reaction, as the other structural parameters. In conclusion, we observe broader oscillations exploring wider distance ranges in the excited state, while really tight oscillations and smaller ranges in the ground state. The explored distance ranges during the excited state MD are approximately twice wider than the ones explored in the ground state. This is especially evident in

the Owat-Hwat and Oser205-Hser205 trends. These broad oscillations are not so standard for bond distances and suggest an actual different strength of the bonds in the two electronic states.

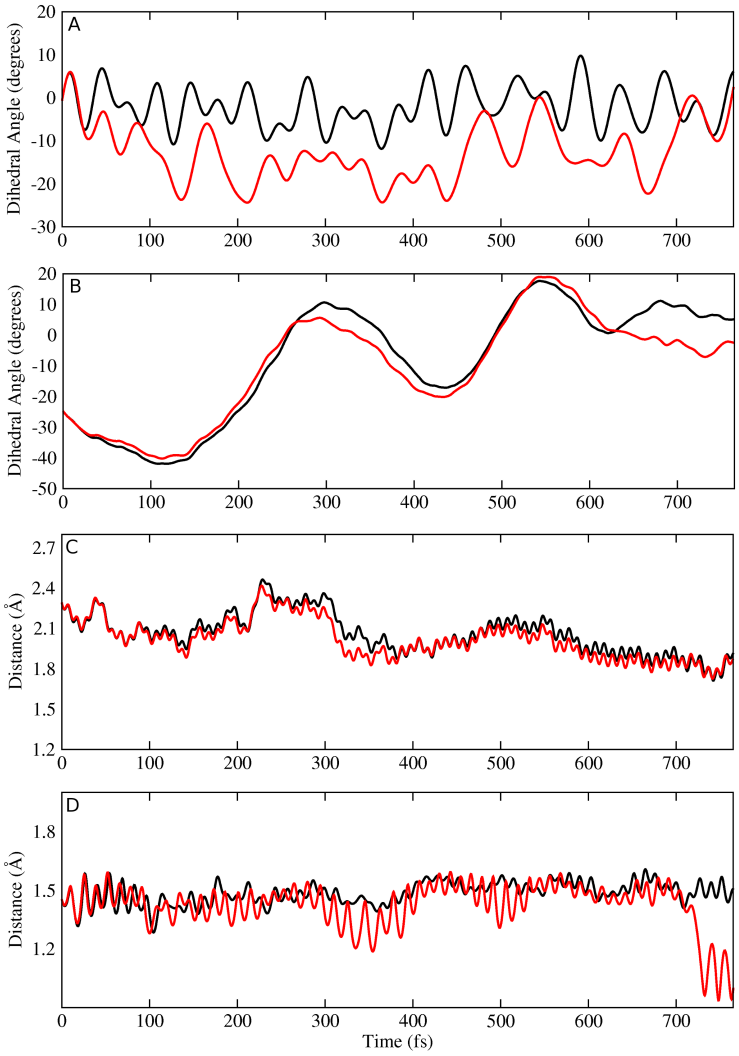

Fig. 2.20: Comparison of distances (Å) and dihedral (degree) angles dynamics, obtained from B3LYP\6-31+g(d,p) S_0 BOMD (black) simulation and TD-CAM-B3LYP\6-31+g(d,p) A_1^P S_1 BOMD (red). The chromophore N-C-C-C dihedral angle (A) and the dihedral angle of oxygen atoms involved in the hydrogen bond network Otyr-Owat-Oser205-Oglu222 (B) dynamics are shown, respectively. The histidine148 Proton-OTyr pair distance dynamics (C) is also shown. The previous presented Hser-Oglu pair distance dynamics is also reported (D), in order to follow the ESPT event.

We also analyze other structural parameters that can further support our thesis that the structural rearrangement, affecting differently the electronic states, influences in a different way the PT reaction in the ground and in the excited state. First, in Figure 2.20 A) the chromophore N-C-C-C dihedral angle S_0 and A_1^P S_1

comparison is shown. A wide range of values is explored by the dihedral angle from about 15 to -25 degrees. The oscillations of this dihedral angle are broader and more irregular respect to the first 1 ps of the ground state trajectory. A sort of depression is described by the dihedral angle from the beginning of the trajectory until about 750 fs. This peculiar behavior seems to be a sort of preparation procedure, before the actual proton transfer event. This connection with the ESPT event can be easily appreciate observing the Hser205-Oglu222 distance evolution that is representative parameter of the reaction. It is evident that the singular trend shown by this dihedral angle has a crucial role in the reaction. This result is clearly confirmed by the dihedral oscillations analyzed in the A_{12}^P S_1 trajectory. By the inspection of Figure 2.21 (upper panel) is clear that this structural parameter presents the same dynamical evolution in both the A_1^P and A_2^P. Large range oscillations until values of -30 degrees are observed. This trend is retained until the proton transfer event, during the other A_2^P S_1 simulation. Moreover after the ESPT, both the trends shift toward an higher range of values i.e. they start oscillating around 0 and upper values. The evident deviation from a regular oscillation trend, and the wide range of values explored in both the simulations, suggests that it is really plausible that the ESPT is promoted by a significant conformation freedom of the chromophore reached in the excited state.

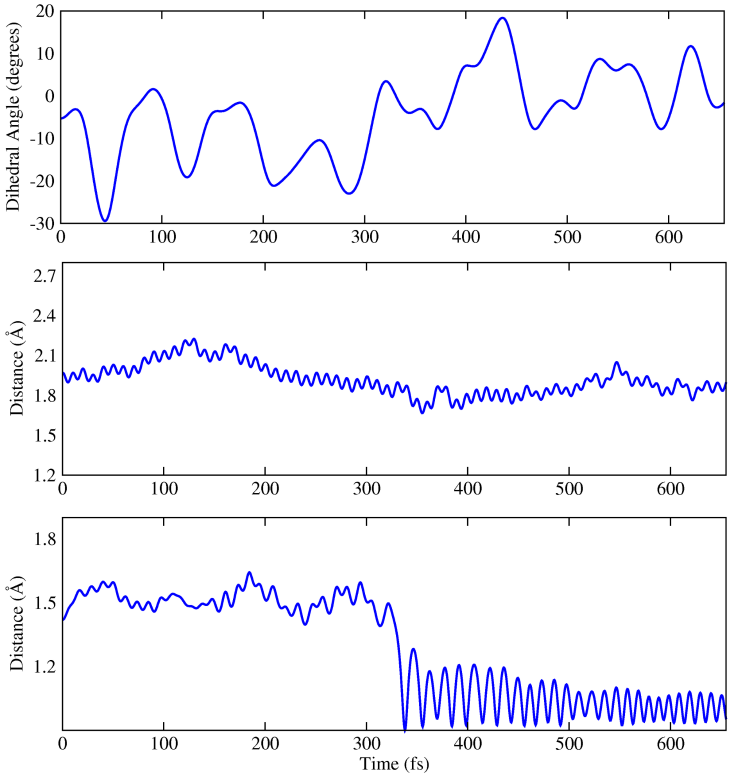

Fig. 2.21: Distances (Å) and dihedral (degree) angles dynamics, obtained from TD-CAM-B3LYP\6-31+g(d,p) A_2^P S_1 BOMD (blue). The chromophore N-C-C-C dihedral angle (upper panel) and the histidine148 Proton-OTyr pair distance (middle panel) dynamics are reported, respectively. The Hser-Oglu pair distance dynamics is also reported (lower panel), in order to follow the ESPT event.

After in Figure 2.20 B) we analyse the dihedral angle involving the oxygens of the hydrogen bond network (Otyr-Owat-Oser205-Oglu222). The trend is not so different in respect to the one observed in the ground state. This dihedral angle reaches values up to -40 degrees and then shows two peaks around 0 (the same one is shifted to higher values in the ground state) and 18 degrees, showing a dynamics similar to S_0 one, until around 550 fs. Later the dihedral angle value starts to decrease until about 710 fs and and, in concurrence with the ESPT reaction, it reaches a sort of plateau around -10 degrees. This plateau is not observed in the ground state. This

different behavior in the two electronic states suggests an active role played by this dihedral angle in the ESPT reaction. It is plausible that the peculiar values assumed in the excited state dynamics at the same time of the proton transfer event promote the reaction and then values around -10 degrees stabilise the product structure.

In the end, in Figure 2.20 C) the distance between the histidine hydrogen nearest to the tyrosine oxygen (the one bonded to N_δ) is shown for 1 ps of both the ground and excited state simulation. Also this time the Hser205-Oglu222 distance is shown for comparison as evidence of the ESPT reaction. Shorter distance values are reached up to 1.8 Å and this trend is similar to the one of the ground state. In the A_2^P S_1 trajectory (see Figure 2.21, middle panel) the role of histidine is more clear. In this case it is more evident that the histidine residue approaches to the chromophore until values around 1.65 Å in concurrence of the ESPT event. This fact suggests an important role of this residue for the PT. Moreover, more in general for both the electronic states, the histidine-chromophore interactions stabilize the anionic product form, as also observed in the energetic analysis of IRC results, presented in Section 2.2.2.4.

2.2.2.6 Energetic Analysis

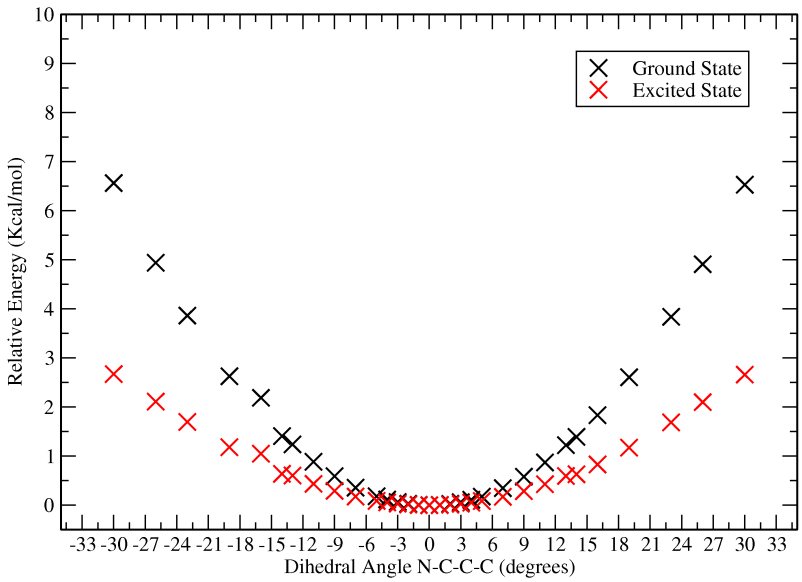

Fig. 2.22: Rigid energy scan of $HBDI^-$ gas phase model along the chrompohore N-C-C-C dihedral angle at TD-CAM-B3LYP\6-31+g(d,p) S_1 (red) and B3LYP\6-31+g(d,p) S_0 (black) theory level. The relative energy corresponding to the reference different minima for both electronic state are reported (in Kcal\mol), the used dihedral value range includes values between -30 and 30 degrees in order to cover the widest range of values explored during the MD.

In Figure 2.22 we show rigid energy scans of the $HBDI^-$ GFP anionic model chromophore for both the ground and excited states at different values of the chromophore N-C-C-C dihedral angle. The chosen range includes values between -30 and 30 degrees in order to cover the widest range of values explored in the excited state protein simulation. Concerning the dihedral angle values from -5 to 5 degrees mostly same energy profile has been observed. For values ranging from -14 to -7 and from 7 to 14 the energy difference grows from 0.18 to 0.78 Kcal\mol and from 0.18 to 0.76 Kcal\mol respectively. This is more emphasized when we move from -16 to -30 and from 16 to 30 degrees indeed in the first case the energy difference increases from 1.14 to 3.89 Kcal\mol and in the second case from 1.83 up to 3.87 Kcal\mol.

These results clearly suggest that in the excited state a wider range of dihedral

angle values is energetically more accessible to the chromophore. It is also qualitatively expressed by the shapes of the curves, according to the steeper S_0 slope compered to S_1. This result is in excellent agreement with the results obtained from our molecular dynamics simulations. During the simulation, as shown in Figure 2.20 A), the chromophore N-C-C-C dihedral angle explores a range of values larger than in the ground state, suggesting that a major conformational freedom is reached by the chromophore after the excitation.

Chapter 3

Beyond the femto second time scale: Modeling the charge-transfer excitons in donor-acceptor polymer solar cells

Bulk heterojunction (BHJ) based polymer solar cells, in which conjugated polymers are blended with fullerene derivatives, are very promising for realizing the goal of achieving low-cost and scalable renewable energy [40; 41]. In particular, power conversion efficiency of 8-9 % in a single junction device has been demonstrated [42; 43].

One of the most important developments for conjugated polymers is the rational design of narrow band gap polymers to better match the solar spectrum [149]. In general, these polymers are copolymers based on an electron-rich donor (D) and an electron-deficient acceptor (A) on the polymer backbone to facilitate the intramolecular charge transfer between D and A. Among various materials developed for BHJ devices, the multifused-ring conjugated polymers are particularly interest-

ing due to their superior optical and electrical properties. The highly fused aromatic\heteroaromatic unit enhances effective conjugation of the polymer backbone to facilitate electron delocalization [150; 151]. Moreover, the covalently rigidified adjacent units could prevent rotational disorder to reduce reorganization energy, which results in enhanced charge mobilities [152; 153].

Several fused-ring ladder type donor systems have been developed, based on the modification of thiophene-phenylene-thiophene (also called indacenodi thiophene (IDT)) skeleton. From the literature, the introduction of fluorine(F) substituents on D-A conjugated polymers has minor effect on their optical properties but affects significantly their energy levels due to its strong electronegativity. From the systematic study of Jen at al. of F-substituted PIDT based polymer, a new ladder-type D-A alternating copolymer poly- [(indacenodithioeno[3,2-b] thiophene) -alt-difluorobenzothiadiazole] (PIDTT-DFBT) (see figure 3.1) has been presented which gave power conversion efficiency in device of 7% without using any solvent additives or post processing techniques [154]. PIDTT-DFBT possesses also a low-lying HOMO, giving an high V_{OC} of nearly 1 V to devices made from it, while its high extinction coefficient and hole mobility result in a photocurrent of 12.2 mA cm^{-2} [155].

It has also been demonstrated that incorporating alkyl thiophene and alkyl thieno[3,2-b] thiophene into PIDTT-DFBT as π-bridges would improve the properties, solubility, and performance of PIDTT-DFBT [155]. We report also the results on two new polymers based on PIDTT-DFBT studied by Jen and coworkers

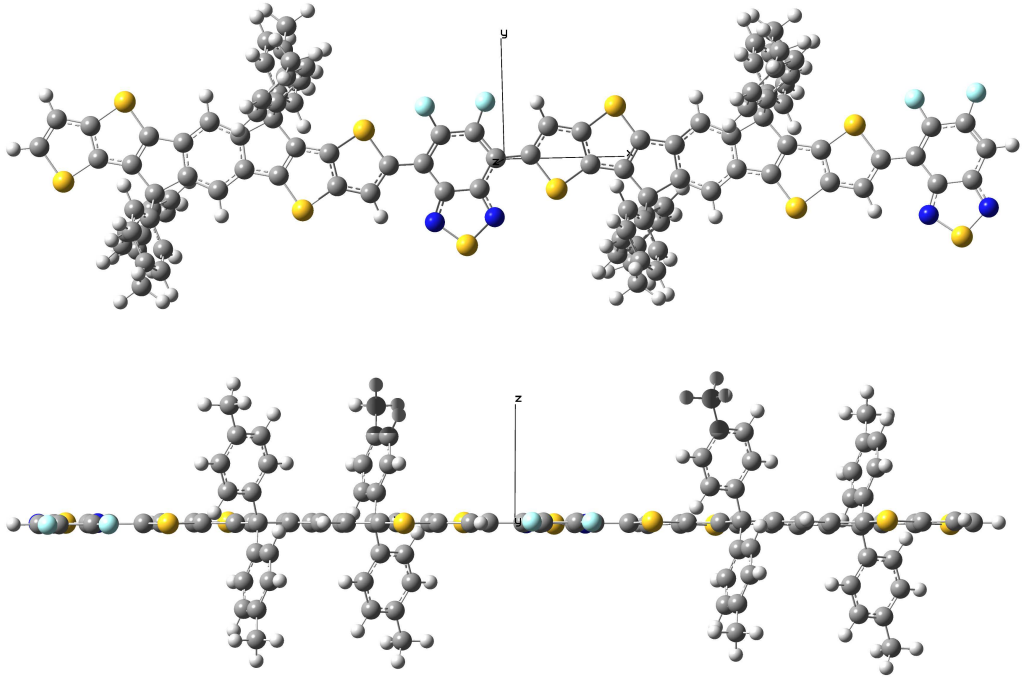

Fig. 3.1: DFT calculated (B3LYP\6-31G(d)) optimized geometry of PIDTT-DFBT dimer unit

[155], integrating 3-hexyl thiophene and 3-octylthieno[3,2-b] thiophene as π-bridges, namely, poly [indacenodithieno[3,2-b] thiophene-alt-(4,7-bis(4-hexylthiophen-2-yl) -5,6-difluoro-[3,1,2] benzothiadiazole)] (PIDTT-DFBT-T) and poly [indacenodithieno[3,2-b] thiophene-alt-94,7-bis (6-octylthieno[3,2-b]thiophen-2-yl) -5,6-difluoro- [3,1,2] benzothiadiazole] (PIDTT-DFBT-TT) (see figure 3.2).

In this work we are interested to study molecular parameters that can influence the charge transport ability of these ladder type polymers to improve their efficiency. DeLongchamp et al. reported that charge transport in amorphous ladder type polymer films occurs primarily along polymer backbone, with a minimum of intermolecular charge-hopping [156]. There is no systematic study about the molecular determinants that can influence the capability of these molecules to transport

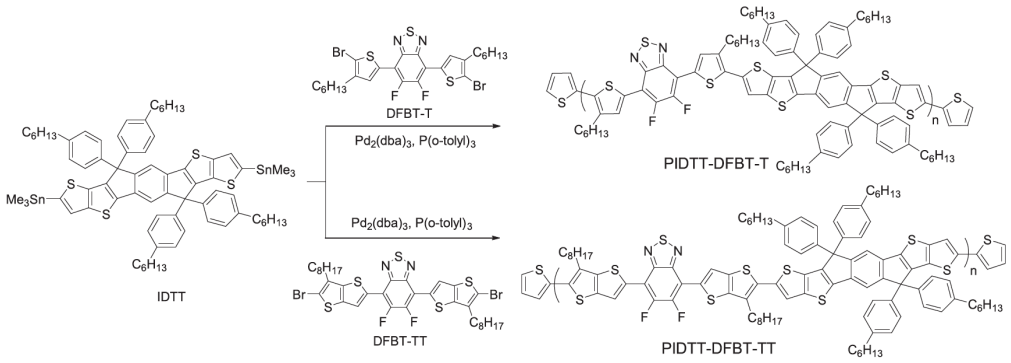

Fig. 3.2: Synthesis scheme of PIDTT-DFBT-T and PIDTT-DFBT-TT from ref.[155]

the charge or how it can diffuse after the excitation process.

In this framework it seems very promising the employment of theoretical tools to study the excitons diffusion process in these polymers. The use of real-time non-adiabatic non-perturbative TDDFT electronic dynamics has been demonstrated useful to a better understanding of the interplay between the photoexcited electron-hole pair and the charge separated state[44; 45]. To elucidate the mechanisms of electron and hole transport following excitation to electronic excited states with significant charge-transfer character, we use quantum electronic dynamics in the TDDFT formalism to explicitly track the density evolution following electronic excitation. From the resulting charge dynamics, p and n type conductivity can be distinguished. By preparing the excited state density as a coherent superposition of formal electronic states, the ensuing charge dynamics are those of an electronic wave packet oscillating between electron rich (donor) and poor (acceptor) domains.

3.1 Methods

We are interested in the exciton dynamics affecting the indiacenodithieno[3,2-b] thienophene-based solar cell devices and how the dynamics, in turn, is influenced by the incorporation of a π-bridge between the donor and acceptor units. Therefore, we need a computational method that provides the explicit evolution of the electronic density along the time after the photon absorption. Thanks to the Real Time Time Dependent Density Functional Theory (RT-TDDFT), we have for the first time an invaluable and innovative computational tool to follow the time evolution of the exciton dynamics affecting the first bright singlet electronic excited state (S1) which is mostly responsible for the absorption band of these materials in the visible range.

Our computational protocol is based on the following steps. First, the electronic density corresponding to the excited state of interest is prepared by promoting an electron from a selected occupied to an unoccupied molecular orbital (Koopman excitation). In all the cases, we perform an HOMO to LUMO swap for an alpha electron. This is due to a previous inspection of the nature of the first bright electronic transition in the visible range, thanks to linear response (LR) TDDFT screening calculations. After, the coherent state is propagated using the RT nonadiabatic nonperturbative TDDFT electronic dynamics. We present a brief summary of method in the following. During the electronic dynamics, the total electron density is projected on the fly into the space of the ground state Kohn-Sham (KS) orbitals as a way to understand its time evolution. The natural population analysis (NPA, Ref. [128]) and the time dependent dipole moment are also computed at selected

time points along the dynamics.

The electronic density matrix is propagated using a modified midpoint unitary transformation (MMUT) algorithm, according to which the TDDFT equation, in the orthonormal basis,

$$i\frac{d\mathbf{P}}{dt} = [\mathbf{K}, \mathbf{P}] \tag{3.1}$$

is implemented as

$$\mathbf{P}(t_{k+1}) = \mathbf{U}(t_k) \cdot \mathbf{P}(t_{k-1}) \cdot \mathbf{U}^{\dagger}(t_k) \tag{3.2}$$

where $\mathbf{P}$ is the electronic density matrix, $\mathbf{K}$ is the Kohn-Sham matrix, and the unitary propagator $\mathbf{U}$ is constructed from the eigenvalues and the eigenvectors of the KS matrix $\mathbf{C}^{\dagger}(t_k) \cdot \mathbf{K}(t_k) \cdot \mathbf{C}(t_k) = \epsilon(t_k)$ as

$$\mathbf{U}(t_k) = \mathbf{C}(t_k) exp[i2\Delta t \epsilon(t_k)] \mathbf{C}^{\dagger}(t_k) \tag{3.3}$$

with $\Delta t = t_{k+1} - t_k$.

The computational time is significantly reduced using a dynamical active space screening for the electronic density, based on incremental Fock builds in the time domain wherein only the contribution to two-electron integrals of portion of the electronic density that are perturbed above a predetermined threshold are recalculated at each time step.[157]

Due to the computational cost, only the electronic dynamics have been evaluated, and we have neglected the effect of nuclear motion on the exciton diffusion. This is a good approximation, because the general trend is still largely unaffected, at least for the short times of our simulations ($\sim$ 50fs), even by the high frequency nuclear

vibration motions.[45]

3.2 Results and Discussion

The polymers involved in the indiacenodithieno[3,2-b]thienophene-based solar cell devices have been modeled in this study as dimers. This approximation is reasonable to achieve a good compromise between the computational cost and the accuracy to analyze the effects of the incorporation of a π-bridge between the donor and acceptor units on the exciton diffusion in these polymers. The dimer is the minimal accurate model suitable for the exciton dynamics of these systems, that still preserves the possibility to investigate the conjugation and long range effects along the polymer chain. Moreover, all the dimer units have been modeled by replacing the hexyl chains appended to the conjugated backbone with methyl groups, to save additional computational time.

The real-time TDDFT electronic dynamics simulation were carried out at the ground state B3LYP\6-31g(d)[71; 158] equilibrium geometries for all the systems from Ref.[155]. The hybrid PBE0 DFT functional[159] has been used to perform the following TDDFT (both LR and RT) calculations. To afford the computational costs of these huge systems, in all the Real-Time TDDFT calculations we additionally reduced the number of basis functions by employing the Stuttgart\Dresden electron-core pseudo-potential[160] for all the core electrons (SDDAll keyword in the *Gaussian* suite of programs). The reliability of this last approximation has been ensured by comparing the LR-TDDFT excitation energies and oscillator strengths calculated by using the SDDAll basis to corresponding 6-31g(d) all electrons LR-TDDFT PBE0 results (see Table 3.1).

	PBE0\6-31g(d)	PBE0\SDDAll
PIDTT-DFBT	1.774 (2.12)	1.736 (1.99)
PIDTT-DFBT-T	1.727 (2.24)	1.672 (1.98)
PIDTT-DFBT-TT	1.758 (2.57)	1.715 (2.24)

Table 3.1: LR-TDDFT excitation energies (eV) for the first electronic transition. The corresponding oscillator strengths are also reported in parenthesis.

A 0.002 fs time step has been used for all real time dynamics, while the NPA charges and dipole magnitude have been evaluated on the fly every 10 steps. The charges have been collected, according to the following definition of acceptor (A) and donor (D) units on each monomer. For all systems in each monomer the acceptor is represented by the 5,6-difluoro-[3,1,2]benzothiadiazole unit, while the remaining part is considered belonging to donor unit, including also the 3-hexylthiophene (-T) and 3-octylthieno[3,2-b] thiophene (-TT) π bridges, when those are present. This partition seems reasonable after the inspection of spatial representations of the frontier molecular orbitals. Moreover, thanks to this partition the polymers still preserve their peculiar alternating sequence of units (A1-D1-A2-D2). For the sake of simplicity we neglected the charge contributions coming from the phenyl side chains. Cross correlation functions involving A1-A2 and D1-D2 units have been also evaluated to study the electron and\or hole diffusion affecting these polymers. All relevant calculations were performed using a modified development version of the *Gaussian* series of program[161] with the addition of the MMUT-TDDFT algorithm.

Analysis

In order to quantify changes in the prepared excitonic state as it evolves under the KS Hamiltonian, the density is projected into the space of the canonical, ground state KS orbitals. Since these orbitals are the eigenfunctions of a Hermitian operator, they form a complete orthonormal set in which the time evolving density can be expanded. Then, an orbital's expansion coefficient can (in an informal sense) be considered the time-evolving fractional occupation number associated with that orbital. The results of applying this projective technique to the propagated α spin density of PIDTT-DFBT and its π-bridged analogues are plotted in figure 3.4. Only orbitals at the 'band-edges' of the studied organic semiconductors exhibit large changes in their occupation, the most important of which are shown in Fig. 3.3

The frontier orbitals of the studied systems show similar characteristics. The molecular orbitals comprising the HOMO band edge are found to be heavily delocalized along the donor backbone of the polymer, while the LUMO and LUMO+1 are localized about the acceptor units. Since the initial excitonic states are prepared via a HOMO-LUMO swap (as suggested by linear response calculations), they are immediately recognized as having significant (Donor $\rightarrow$ Acceptor) charge-transfer character. Within the first $\sim$10fs, a near complete recovery of the ground state occurs for each of the studied systems. However, the orbital pathway by which the density relaxation occurs differs drastically between polymers. In polymers containing additional π-bridges between groups, a very fast loss of HOMO occupation and correlated occupation in HOMO-2 occupation is observed, while for the unmod-

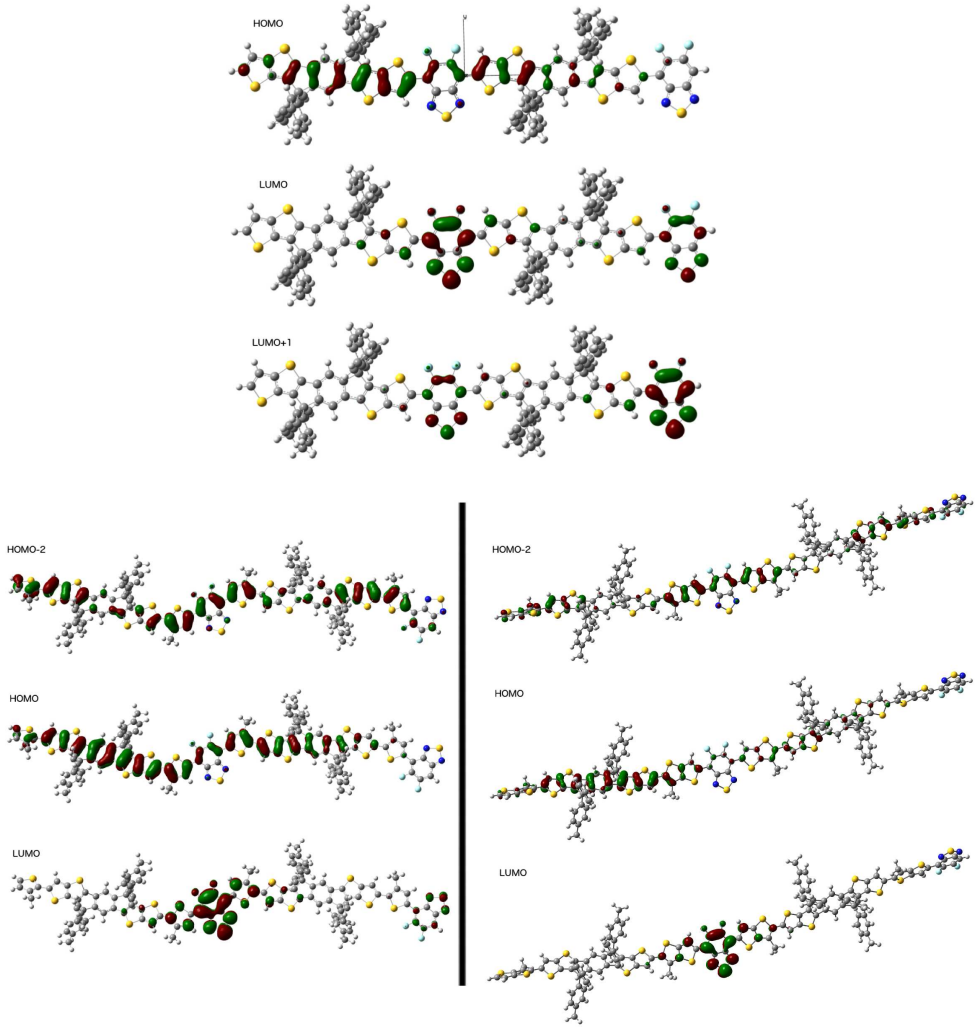

Fig. 3.3: Visualizations of the KS orbitals most relevant to the density evolution (PIDTT-DFBT top, PIDTT-DFBT-T bottom left, PIDTT-DFBT-TT bottom right).

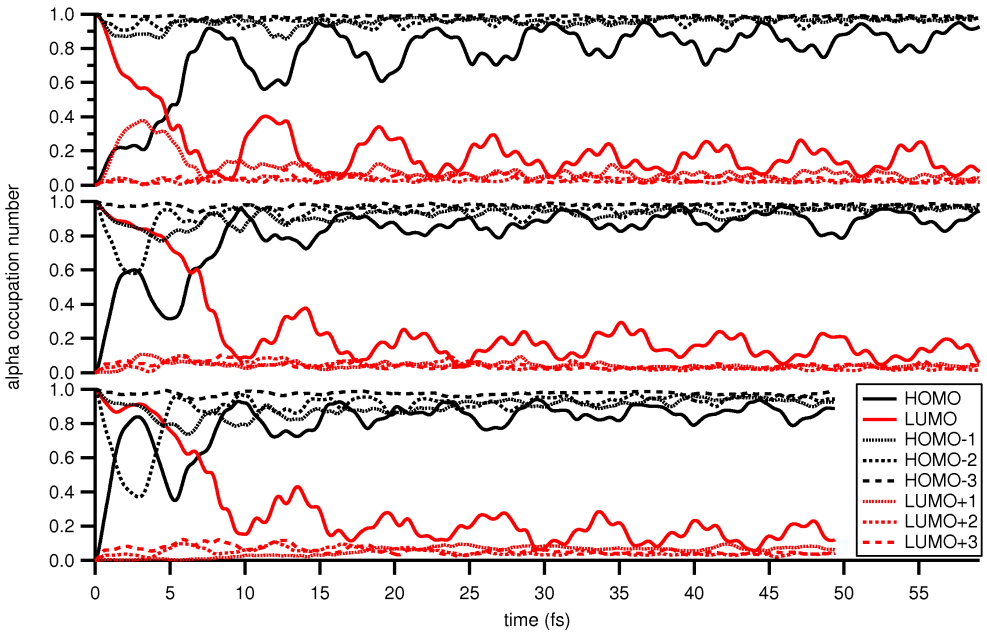

Fig. 3.4: Time evolving fractional occupation numbers of the canonical KS orbitals (PIDTT-DFBT top, PIDTT-DFBT-T bottom left, PIDTT-DFBT-TT bottom right).

ified PIDTT-DFBT a similar correlation is observed in the unoccupied manifold between the LUMO and LUMO+1 occupations. This significant result suggests different charge separation mechanisms for PIDTT-DFBT and its π-bridged analogues. For PIDTT-DFBT, the electron migrates between orbitals localized to the acceptor groups suggesting the migration of the electron following excitation, while it is the hole in PIDTT-DFBT-T and PIDTT-DFBT-TT which relaxes to lower energy states in the occupied manifold, suggesting hole migration as the predominant short-time charge separation mechanism in this system. The experimental trends for hole mobility with respect to the inclusion of π spacers show increasing hole mobility as large spacers are introduced, [162] even if the observed decreased hole mobility affecting the PIDTT-DFBT-T is likely related to the length of the its polymer chain,

and by extension, to the molecular weight. The general trend is somewhat counter-intuitive, considering the degree of planarity is reduced upon the inclusion of larger spacers, truncating the polymer's effective conjugation length. However, despite the decreased delocalization of the HOMO in PIDTT-DFBT-T, hole migration appears to be by far the dominant separation mechanism.

The electronic dynamics in the 10-50 fs regime yield information concerning the long-lived charge oscillations that follow the initial charge carrier separation and coherent recombination. In an effort to better understand the time evolution of the electronic density following excitation to the S1 states of the studied dimers, we have performed natural population analysis to determine the electronic dynamics in terms of atomic charges. To simplify the interpretation and presentation of these atomic charges, contributions from each constituent atom in a given donor\acceptor moiety were summed to illustrate the charge oscillations between donor\acceptor blocks. This partitioning of the dimer into its constituent moieties is identified in the methodology section. The time evolution of these moiety charges are given in figure 3.5. Again, in the earliest femtoseconds, we see signatures of the coherent charge carrier recombination, and the residual oscillation in these charges at longer simulation times are indicative of charge transfer between D\A blocks.

From inspection, the summed charges on the first and second donor groups (D1\D2) and the charges of the first donor and acceptor (A1\D1) appear correlated. The A1\D1 correlation in the 1-10 fs range is a consequence of the coherent recombination of the exciton, while the D1\D2 correlation accompanies hole migra-

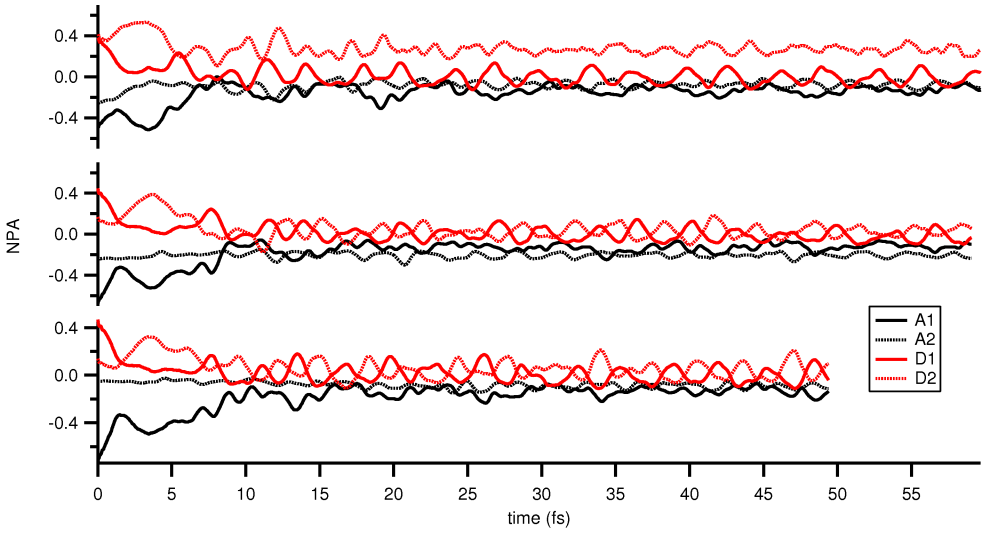

Fig. 3.5: Summed alpha NPA charges for Donor and Acceptor blocks 1 and 2 ((PIDTT-DFBT top, PIDTT-DFBT-T middle, PIDTT-DFBT-TT bottom .)

tion. A similar A1\A2 correlation would indicate the migration of the electron. To better illustrate the relationships between these groups' oscillating charges, cross correlation functions were calculated between the time-evolving D1\D2 and A1\A2 charges (see figure 3.6.)

Minima in these cross correlation functions occur for offset times that result in the charge oscillations on the relevant groups being out-of-phase with one another (i.e. peaks in one of the group's charge evolution line up with troughs in the other's) whereas maxima in the cross-correlation function signify offset times that yield a maximum coincidence of the two time-ordered series. Because charge-transfer is phenomenologically defined by the loss of charge density on one moiety and simultaneous rise in charge density on another, a correlation function corresponding to this situation would show oscillatory behavior (with a period equal to the period of the charges' oscillations between moieties) and a value at offset times near zero that

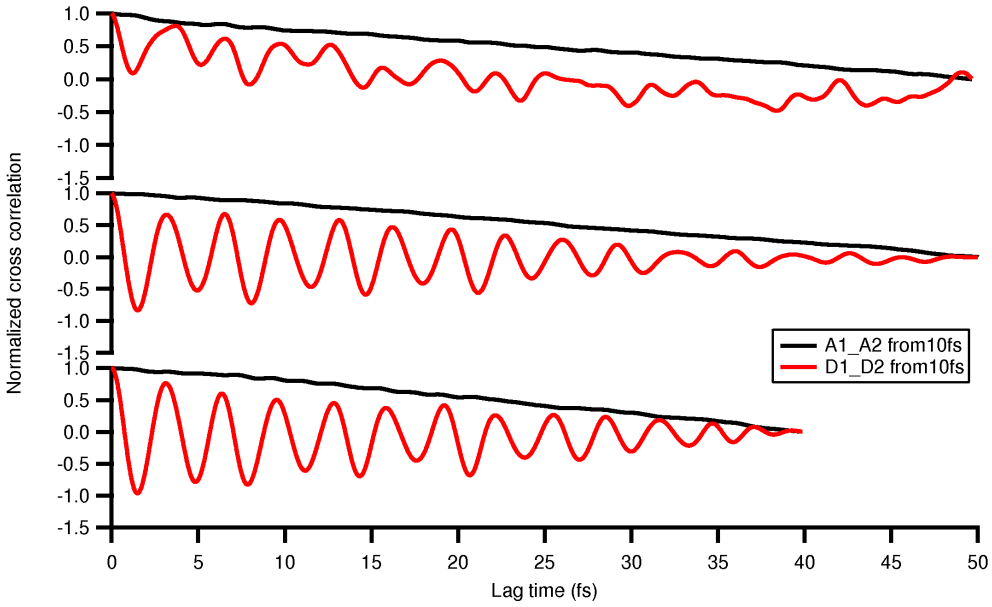

Fig. 3.6: Cross-correlation functions between the time evolving D1\D2 charges and A1\A2 charges indicative of hole and electron diffusion along the polymer backbone respectively (PIDTT-DFBT top, PIDTT-DFBT-T middle, PIDTT-DFBT-TT bottom.)

is close to a minimum. A charge cross correlation function of this type indicates the 'sloshing' of electrons back and forth between the selected moieties along the polymer backbone. The frequency of oscillations in the cross correlation functions therefore proportionate to the hole\electron mobility in these systems.

Accordingly, Fourier analysis was carried out for each of the cross correlation functions to identify the frequencies underlining the charge oscillations, and is shown in Figure 3.7. By the inspection of this figure, the different dimer units present a similar frequency contributions in the donors oscillations. As matter of fact, it is not easy two differentiate the system because the long range charge transport along the entire backbone cannot be rightly simulated by a simple dimer unit, mostly if the charge carrier mobility is directly related to the length of the polymer chain.

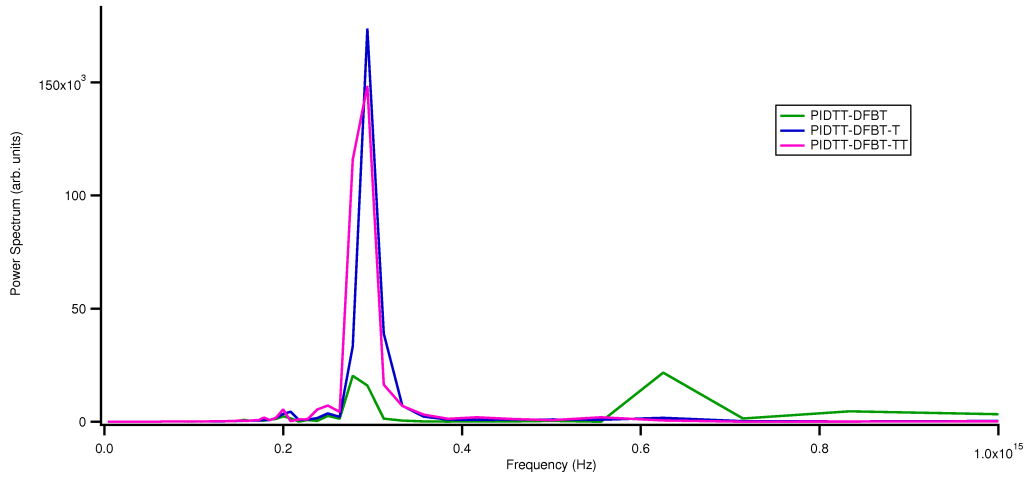

Fig. 3.7: Fourier power spectra of the charge cross-correlation functions indicating hole mobility in the studied systems (PIDTT-DFBT green, PIDTT-DFBT-T blue, PIDTT-DFBT-TT magenta).

In spite of complex features that can affect the different performances of these devices, we presented a general protocol to show the hole (or electron) mobility behavior BHJ based polymer solar cells. In fact, by preparing the excited state density as a coherent superposition of formal electronic states, we were able to observe the charge dynamics due to an electronic wave packet oscillating between electron rich (donor) and poor (acceptor) domain and to analyze the frequency and decay profiles of these oscillations. This kind of study seems to be very promising to get insights into the diffusion rate and lifetime of excitons generated upon photoexcitation of these materials.

Concluding Remarks

During this Ph.D. program we have been focusing on the development of new theoretical techniques and computational protocols to face the new challenges provided by the novel time resolved experiments. The shorter and shorter time resolution, explored by the modern time-resolved spectroscopy has provided us the chance to visualize non equilibrium phenomena ranging from picosecond to attosecond. In the recent years, chemistry has started to directly monitor the dynamical evolution of processes affecting these short time scales, such as the collective solvent motions, the excited state photo-reactivity or the exciton diffusion.

Beside, the theory has conceived new paradigms to deal with these ultra-fast phenomena. In these scientific framework, we developed several theoretical protocols to study the non-equilibrium processes and photo-reactivity affecting, the electronic excited states. For this purpose ab initio molecular dynamics have been largely employed along with other computational protocols to explore in a clever and faster way the potential energy surface of the molecular systems under study, such as the integration of the intrinsic reaction coordinates, the vibrational analysis, ad hoc conceived functions to account for the structural reorganization upon the electronic excitation. Regarding the ultra-fast atto dynamics, we also computed the explicit

electronic density evolution by integrating the time dependent Schrodinger equation.

The theoretical and computational approaches developed during this Ph.D. program provided the chance to study the solvation dynamics affecting the time-resolved Stokes shift of a solvatochromic dye. We were able to disentangle the huge number of frequency components affecting a signal evolution, finding their molecular base. In this way the solvatochromic dye appeared to be used as an infra-red probe, thanks to the collective solvent motions affecting the whole Stoke-Shift signal.

We also exploited a composite theoretical protocol to explore the molecular determinants ruling the excited state proton transfer event in the green fluorescent protein. The proton transfer reaction was studied both on a minimal model compound and on the whole protein matrix, the latter starting from the crystallographic structure. For this system, the intrinsic reaction coordinate was integrated on a minimal model compound, while a molecular dynamics study was performed on the whole protein, in both the ground and the excited state. The following structural, energetic and vibrational analysis proved the crucial role of structural re-organization of the proton wire network upon the excitation. Our developed protocol proved the accuracy of DFT in the photo-reactions studies and, on the other side, helped the scientific community to shed light on the several mechanistic hypotheses proposed for the GFP excited state proton transfer.

Finally, the attosecond time-scale phenomena allowed us to deal with electronic explicit motions and, therefore, to enforce new algorithms and protocols to model the electron-hole diffusion in polymer models, employed in BHJ solar cell devices.

Indeed, the Real-Time TD-DFT approach allowed us to simulate and observe the exciton diffusion along a minimal dimer chain for several different monomer types. Our preliminary study on these models, along with the development of several Real-Time analysis tools, gave us the chance to the hole diffusion in these model. Moreover, we also tried to extrapolate the effects of a modification at the molecular scale on the macroscopic behavior of the entire device, in a qualitative correspondence with the available experimental data.

During these years we developed new theoretical and computational approaches, validating them on still open complex scientific issues. We confirm that the synergy between theory and experiment is mandatory to face the new challenges provided by new experiments on the shorter and shorter time scales.

List of Figures

List of Tables

Bibliography

[1] J. Pérez-Lustres, S. Kovalenko, M. Mosquera, T. Senyushkina, W. Flasche, and N. Ernsting, Angew. Chem. Int. Ed. **44**, 5635 (2005).

[2] A. Zewail, J. Phys. Chem. A **104**, 5660 (2000).

[3] T. R. Jimenez, G. R. Fleming, V. Kumar, and M. Maroncelli, Nature **369**, 471 (1994).

[4] G. R. Fleming and M. Cho, Annu. Rev. Phys. Chem. **47**, 109 (1996).

[5] M. Maroncelli, J. Mol. Liq. **57**, 1 (1993).

[6] C. F. Chapman, R. S. Fee, and M. Maroncelli, J. Phys. Chem. **99**, 4811 (1995).

[7] M. Maroncelli and G. R. Fleming, J. Chem. Phys. **89**, 875 (1988).

[8] E. W. C. Jr., G. R. Fleming, and B. Bagchi, Chem. Phys. Letters **143(3)**, 270 (1988).

[9] X. Song and D. Chandler, J. Chem. Phys. **108**, 2594 (1998).

[10] M. S. Skaf and B. M. Ladanyi, J. Phys. Chem. **100**, 18258 (1996).

[11] Y. Georgievskii, C.-P. Hsu, and R. A. Marcus, J. Chem. Phys. **108**, 7356 (1998).

[12] H. L. Friedman, F. O. Raineri, and B.-C. Perng, J. Mol. Liq. **66**, 7 (1995).

[13] D. V. Matyushov, J. Chem. Phys. **122**, 044502 (2005).

[14] B. Bagchi, JCP **100**, 6658 (1994).

[15] K. E. Furse and S. A. Corcelli, J. Phys. Chem. Lett. **100**, 1813 (2010).

[16] N. Nandi, K. Bhattacharyya, and B. Bagchi, Chem. Rev. **100**, 2013 (2000).

[17] B. Bagchi, Annu. Rev. Phys. Chem. **47**, 109 (1996).

[18] S. Dapprich, I. Komaromi, K. S. Byun, K. Morokuma, and M. J. Frisch, J. Mol. Struct.(Theochem) **462**, 1 (1999).

[19] T. Vreven, K. S. Byun, I. Komaromi, S. Dapprich, J. A. M. Jr., K. Morokuma, and M. J. Frisch, J. Chem. Theory and Comput. **2**, 815 (2006).

[20] T. Vreven and K. Morokuma, *Annual Reports in Computational Chemistry* (Vol.2, pp 35-51, Ed. D. C. Spellmeyer, 2006).

[21] F. Clemente, T. Vreven, and M. J. Frish, *Quantum Biochemistry* (Ed. C. Matta (Wiley VCH), 2008).

[22] G. Brancato, N. Rega, and V. Barone, J. Chem. Phys. **125**, 164515 (2006).

[23] G. Brancato, V. Barone, and N. Rega, Theor. Chem. Acc. **117**, 1001 (2007).

[24] N. Rega, G. Brancato, and V. Barone, Chem. Phys. Lett. **422**, 367 (2006).

[25] D. F. Walnut, *An introduction to Wavelet Analysis* (Birkhäuser Boston, Department of Mathematical Sciences George Mason University Fairfax, VA 22030 USA, 2002).

[26] I. Daubechies, IEEE Transactions on Information Theory **36**, 961 (1990).

[27] M. E. Martin, F. Negri, and M. Olivucci, J. Am. Chem. Soc. **126**, 5452 (2004).

[28] T. Laino, R. Nifosi, and V. Tozzini, Chem. Phys. **298**, 17 (2004).

[29] W. Yan, L. Zhang, D. Xie, and J. Zeng, J. Comput. Chem. **26**, 1487 (2005).

[30] E. Epifanovsky, I. Polyakov, B. Grigorenko, A. Nemukhin, and A. I. Krylov, J. Chem. Theory Comput. **5**, 1895 (2009).

[31] M. Wanko, P. García-Risueño, and A. Rubio, Phys. Status Solidi B pp. 392–400 (2012).

[32] C. Filippi, M. Zaccheddu, and F. Buda, J. Chem. Theory Comput. **5**, 2074 (2009).

[33] C. Filippi, F. Buda, L. Guidoni, and A. Sinicropi, J. Chem. Theory Comput. **8**, 112 (2012).

[34] A. Petrone, P. Caruso, S. Tenuta, and N. Rega, Phys. Chem. Chem. Phys. **15**, 20536 (2013).

[35] R. Y. Tsien, Annu. Rev. Biochem. **67**, 509 (1998).

[36] H. P. Hratchian and H. B. Schlegel, The Journal of Physical Chemistry A **106** (1), 165 (2002).

[37] S. Wang and S. C. Smith, Phys. Chem. Chem. Phys. **9**, 452 (2006).

[38] S. Wang and S. C. Smith, J. Phys. Chem. B **110**, 5084 (2006).

[39] O. Vendrell, R. Gelabert, M. Moreno, and J. M. Lluch, J. Chem. Theory Comput. **4**, 1138 (2008).

[40] J. Chen and Y. Ca, Acc. Chem. Res. **42**, 1709 (2009).

[41] Y.-J. Cheng, S.-H. Yang, and C.-S. Hsu, Chem. Rev. **109**, 5868 (2009).

[42] Z. He, C. Zhong, X. Huang, W.-Y. Wong, H. Wu, L. Chen, S. Su, and Y. Cao, Adv. Mater. **23**, 4636 (2011).

[43] T. Yang, M. Wang, C. Duan, X. Hu, L. Huang, J. Peng, F. Huang, and X. Gong, Energ. Environ. Sci. **5**, 8208 (2012).

[44] C. T. Chapman, W. Liang, and X. Li, J. Phys. Chem. Lett. **2** (10), 1189 (2011).

[45] F. Ding, C. T. Chapman, W. Liang, and X. Li, J. Chem. Phys. **137**, 22A512 (2012).

[46] J. Simon, Acc. Chem. Res. **21**, 128 (1988).

[47] N. Nandi, S. Roy, and B. Bagchi, J. Chem. Phys. **102**, 1390 (1995).

[48] C. F. Chapman, R. S. Fee, and M. Maroncelli, J. Phys. Chem. **99**, 4811 (1995).

[49] M. Sajadi, T. Obernhuber, S. A. Kovalenko, M. Mosquera, B. Dick, and N. P. Ernsting, J. Phys. Chem. A **113**, 44 (2009).

[50] J. Yu and M. Berg, Chem. Phys. Lett. **208**, 315 (1993).

[51] A. J. Benigno, E. Ahmed, and M. Berg, J. Chem. Phys. **104**, 7382 (1996).

[52] O. Rioul and M. Vetterli, IEEE Signal Processing Magazine **8**, 14 (1991).

[53] C. Torrence and C. P. Compo, Bulletin of the American Meteorological Society **79**, 61 (1998).

[54] M. Pagliai, F. Muniz-Miranda, G. Cardini, R. Righini, and V. Schettino, J. Phys. Chem. Lett. **1**, 2951 (2010).

[55] M. Sajadi, Y. Ajaj, I. Loffe, H. Weingartner, and N. P. Ernisting, Angew. Chem. Int. Ed. **49**, 454 (2010).

[56] H. B. Schlegel, J. M. Millam, S. S. Iyengar, G. A. Voth, A. D. Daniels, G. E. Scuseria, and M. J. Frisch, J. Chem. Phys. **114**, 9758 (2001).

[57] S. S. Iyengar, H. B. Schlegel, J. M. Millam, G. A. Voth, G. E. Scuseria, and M. J. Frisch, J. Chem. Phys. **115**, 10291 (2001).

[58] K. Bolton, W. L. Hase, and G. H. Peslherbe, *Modern Methods for Multidimensional Dynamics Computation in Chemistry* (Edited by D. L. Thompson., World Scientific, Singapore, 1998), vol. 95, pp. 143–189.

[59] J. M. Millam, V. Bakken, W. Chen, W. L. Hase, and H. B. Schlegel, J. Chem. Phys. **111**, 3800 (1999).

[60] M. Pagliai, G. Cardini, R. Righini, and V. Schettino, J. Chem. Phys **119**, 6655 (2003).

[61] C. Dorize and L. F. Villemoes, IEEE p. 2029 (1991).

[62] R. Carmona, W.-L. Hwang, and B. Torrésani, *Practical Time-Frequency Analysis: Gabor and Wavelet Transforms, with an Implementation in S*, vol. 9 (Academic Press, San Diego, USA, 1998).

[63] T. Otsuka and H. Nakai, J. Comput. Chem. **28**, 1138 (2007).

[64] B. S. Mallik and A. Chandra, J. Mol. Liq. **143**, 31 (2008).

[65] M. Pagliai, F. Muniz-Miranda, G. Cardini, R. Righini, and V. Schettino, J. Mol. Struct. **993**, 438 (2011).

[66] S. D. Meyers, B. G. Kelly, and J. J. O'Brien, Mon. Weather Rev. **121**, 2858 (1993).

[67] T. R. Jimenez, G. R. Fleming, V. Kumar, and M. Maroncelli, Nature **369**, 471 (1994).

[68] G. Brancato, N. Rega, and V. Barone, J. Am. Chem. Soc. **129**, 15380 (2007).

[69] W. Ellison, J. Phys. Chem. Ref. Data **36** (1), 1 (2007).

[70] H. B. Schlegel, S. S. Iyengar, X. Li, J. M. Millam, G. A. Voth, G. E. Scuseria, and M. J. Frisch, J. Chem. Phys. **117**, 8694 (2002).

[71] A. D. Becke, J. Chem. Phys. **98**, 5648 (1993).

[72] W. L. Jorgensen, J. Chandrasekhar, J. D. Madura, R. W. Impey, and M. L. Klein, J. Chem. Phys. **79**, 926 (1983).

[73] G. Brancato, N. Rega, and V. Barone, J. Chem. Phys. **128**, 144501 (2008).

[74] V. Barone and M. Cossi, J. Phys. Chem. A **102**, 1995 (1998).

[75] M. Cossi, N. Rega, G. Scalmani, and V. Barone, J. Comp. Chem. **24**, 669 (2003).

[76] D. L. Bunker, Meth. Comp. Phys. **10**, 287 (1971).

[77] L. M. Raff and D. L. Thompson, *Theory of Chemical Reaction Dynamics* (CRC, Boca Raton,FL, 1985).

[78] E. W. L. Hase, ed., *Advances in Classical Trajectory Methods* (JAI, Stamford,CT, 1991).

[79] T. Helgaker, E. Uggerud, and H. J. A. Jensen, Chem. Phys. Lett. **173**, 145 (1990).

[80] E. K. U. Gross and W. Kohn, Phys. Rev. Lett. **55**, 2850 (1985).

[81] R. E. Stratmann, G. E. Scuseria, and M. J. Frisch, J. Chem. Phys. **109**, 8218 (1998).

[82] M. J. Frisch, G. W. Trucks, H. B. Schlegel, G. E. Scuseria, M. A. Robb, J. R. Cheeseman, G. Scalmani, V. Barone, B. Mennucci, G. A. Petersson, H. Nakatsuji, M. Caricato, X. Li, H. P. Hratchian, A. F. Izmaylov, J. Bloino, G. Zheng, J. L. Sonnenberg, M. Hada, M. Ehara, K. Toyota, R. Fukuda, J. Hasegawa, M. Ishida, T. Nakajima, Y. Honda, O. Kitao, H. Nakai, T. Vreven, J. A. Montgomery, Jr., J. E. Peralta, F. Ogliaro, M. Bearpark, J. J. Heyd, E. Brothers, K. N. Kudin, V. N. Staroverov, R. Kobayashi, J. Normand, K. Raghavachari, A. Rendell, J. C. Burant, S. S. Iyengar, J. Tomasi, M. Cossi, N. Rega, J. M. Millam, M. Klene, J. E. Knox, J. B. Cross, V. Bakken, C. Adamo, J. Jaramillo, R. Gomperts, R. E. Stratmann, O. Yazyev, A. J. Austin, R. Cammi, C. Pomelli, J. W. Ochterski, R. L. Martin, K. Morokuma, V. G. Zakrzewski, G. A. Voth, P. Salvador, J. J. Dannenberg, S. Dapprich, A. D. Daniels, . Farkas, J. B. Foresman, J. V. Ortiz, J. Cioslowski, and D. J. Fox, *Gaussian 09 Revision A.2*. Gaussian Inc. Wallingford CT 2009.

[83] T. M. H. Creemers, A. J. Lock, V. Subramaniam, T. M. Jovin, and S. Volker, Nat. Struct. Biol. **6**, 557 (1999).

[84] M. Kondo, I. A. Heisler, D. Stoner-Ma, P. J. Tonge, and S. R. Meech, J. Photochem. Photobiol. **234**, 21 (2012).

[85] K. Brejc, T. K. Sixma, P. A. Kitts, S. R. Kain, R. Y. Tsien, M. Ormo, and S. J. Remington, Proc. Natl. Acad. Sci. USA **94**, 2306 (1997).

[86] M. Chattoraj, B. A. King, G. U. Bublitz, and S. G. Boxer, Proc. Natl. Acad. Sci. USA **93**, 8362 (1996).

[87] G. Striker, V. Subramaniam, C. A. M. Seidel, and A. Volkmer, J. Phys. Chem. B **103**, 8612 (1999).

[88] A. Volkmer, V. Subramaniam, D. Birch, and T. Jovin, Biophysical journal **78** (3), 1589 (2000).

[89] J. van Thor, T. Gensch, K. J. Hellingwerf, and L. N. Johnson, Nat. Struct. Biol. **9**, 37 (2002).

[90] M. Ormo, A. B. Cubitt, K. Kallio, L. A. Gross, R. Y. Tsien, and S. J. Remington, Science **273**, 1392 (1996).

[91] W. Weber, V. Helms, J. A. McCammon, and P. W. Langhoff, Proc. Nat. Acad. Sci. U.S.A. **96**, 6177 (1999).

[92] A. Usman, O. F. Mohammed, E. T. J. Nibbering, J. Dong, K. M. Solntsev, and L. M. Tolber, J. Am. Chem. Soc. **127**, 11214 (2005).

[93] K. B. Bravaya, M. G. Khrenova, B. L. Grigorenko, A. V. Nemukhin, and A. I. Krylov, J. Phys. Chem. B **115**, 8296 (2011).

[94] S. B. Nielsen, A. Lapierre, J. U. Andersen, U. V. Pedersen, S. Tomita, and L. H. Andersen, Phys. Rev. Lett. **87**, 228102(4) (2001).

[95] L. H. Andersen, H. Bluhme, S. Boye, T. J. D. Jorgensen, H. Krogh, I. B. Nielsen, S. B. Nielsen, and A. Svendsen, Phys. Chem. Chem. Phys. **6**, 2617 (2004).

[96] M. W. Forbes and R. A. Jockusch, J. Am. Chem. Soc. **131**, 17038 (2009).

[97] G. H. Patterson, S. M. Knobel, W. D. Sharif, S. R. Kain, and D. W. Piston, Biophys. J. **73**, 2782 (1997).

[98] J. Dong, K. M. Solntsev, and L. M. Tolbert, J. Am. Chem. Soc. **128**, 12038 (2006).

[99] X. Li, L. W. Chung, H. Mizuno, A. Miyawaki, and K. Morokuma, J. Phys. Chem. B **114**, 1114 (2010).

[100] K. Chingin, R. M. Balaboin, V. Frankevich, K. Barylyuk, R. Nieckarz, P. Sagulenko, and R. Zenobi, Int. J. Mass Spectrom. **306**, 241 (2011).

[101] S. Olsen and S. C. Smith, J. Am. Chem. Soc. **130**, 8677 (2008).

[102] A. Sinicropi, T. Andruniow, N. Ferr, R. Basosi, and M. Olivucci, J. Am. Chem. Soc. **127**, 11534 (2005).

[103] K. B. Bravaya, B. L. Grigorenko, A. V. Nemukhin, and A. I. Krylov, Acc. Chem. Res. **45**, 265 (2012).

[104] V. R. I. Kaila, R. Send, and D. Sundholm, Phys. Chem. Chem. Phys. **15**, 4491 (2013).

[105] M. T. P. Beerepoot, A. H. Steindal, J. Kongsted, B. O. Brandsdal, L. Frediani, K. Ruud, and J. M. H. Olsen, Phys. Chem. Chem. Phys. **15**, 4735 (2013).

[106] N. M. Webber and S. R. Meech, Photochem. Photobiol. Sci. **6**, 976 (2007).

[107] A. A. Voityuk, M.-E. Michel-Beyerle, and N. Rösch, Chem. Phys. **231** (1), 13 (1998).

[108] A. V. Nemukhin, I. A. Topol, and S. K. Burt, J. Chem. Theory Comput. **2**, 292 (2006).

[109] I. Polyakov, E. Epifanovsky, B. Grigorenko, A. I. Krylov, and A. V. Nemukhin, J. Chem. Theory Comput. **5**, 1907 (2009).

[110] D. Zuev, K. B. Bravaya, M. V. Makarova, and A. I. Krylov, J. Chem. Phys. **135**, 194304 (2011).

[111] M. E. Casida, C. Jamorski, K. C. Casida, and D. R. Salahub, J. Chem. Phys. **108**, 4439 (1998).

[112] R. E. Stratmann, G. E. Scuseria, and M. J. Frisch, J. Chem. Phys. **109**, 8218 (1998).

[113] C. V. Caillie and R. D. Amos, Chem. Phys. Lett. **308**, 249 (1999).

[114] K. Burke and E. K. U. Gross, *Density functionals: theory and applications* (pp. 116-146, Springer Berlin, 1998).

[115] S. Miertus, E. Scrocco, and J. Tomasi, Chem. Phys. **55**, 117 (1981).

[116] R. Cammi, S. Corni, B. Mennucci, and J. Tommasi, J. Chem. Phys. **122**, 104513 (2005).

[117] S. Corni, R. Cammin, B. Mennucci, and J. Tommasi, J. Chem. Phys. **123**, 134512 (2005).

[118] R. Improta, V. Barone, G. Scalmani, and M. J. Frisch, J. Chem. Phys. **125**, 54103 (2006).

[119] R. Improta, G. Scalmani, M. J. Frisch, and V. Barone, J. Chem. Phys. **127**, 74504 (2007).

[120] B. Mennucci, C. Cappelli, C. A. Guido, R. Cammi, and J. Tommasi, J. Phys. Chem. A **113**, 3009 (2009).

[121] A. V. Marenich, C. J. Cramer, D. G. Truhlar, C. A. Guido, B. Mennucci, G. Scalmani, and M. J. Frisch, Chemical Science **2**, 2143 (2011).

[122] T. Yanai, D. Tew, and N. Handy, Chem. Phys. Lett. **393**, 51 (2004).

[123] S. Grimme, J. Comput. Chem. **27**, 1787 (2006).

[124] T. Vreven and K. Morokuma, Theor. Chem. Acc. **109**, 125 (2003).

[125] T. Vreven and K. Morokuma, J. Chem. Phys. **113**, 2969 (2000).

[126] T. Vreven, B. Mennucci, C. O. da Silva, K. Morokuma, and J. Tomasi, J. Chem. Phys. **115**, 62 (2001).

[127] S. J. Mo, T. Vreven, B. Mennucci, K. Morokuma, and J. Tomasi, Theor. Chem. Acc. **111**, 154 (2003).

[128] A. E. Reed, R. B. Weinstock, and F. Weinhold, J. Chem. Phys. **83**, 735 (1985).

[129] W. D. Cornell, P. Cieplak, C. I. Bayly, I. R. Gould, K. M. Merz, D. M. Ferguson, D. C. Spellmeyer, T. Fox, J. W. Caldwell, and P. A. Kollman, J. Am. Chem. Soc. **117**, 5179 (1995).

[130] N. Reuter, H. Lin, and W. Thiel, J. Phys. Chem. B **106**, 6310 (2002).

[131] T. Vreven, K. Morokuma, O. Farkas, H. B. Schlegel, and M. J. Frisch, J. Comput. Chem. **24**, 760 (2003).

[132] A. A. Voityuk, M.-E. Michel-Beyerle, and N. Rosch, Chem. Phys. Lett. **272**, 162 (1997).

[133] V. Helms, C. Winstead, and P. W. Langhoff, J. Molec. Struct. (Theochem) **506**, 179 (2000).

[134] A. K. Das, J.-Y. Hasegawa, T. Miyahara, M. Ehara, and H. Nakatsuji, J. Comput. Chem. **24**, 1421 (2003).

[135] A. Toniolo, S. Olsen, L. Manohara, and T. J. Martinez, Faraday Discuss. **127**, 149 (2004).

[136] I. Polyakov, B. G. E. M. Epifanovsky, A. I. Krylov, and A. V. Nemukhin, J. Chem. Theory Comput. **6**, 2377 (2010).

[137] W. W. Ward and S. H. Bokman, Biochemistry **21**, 4535 (1982).

[138] R. Gepshtein, D. Huppert, and N. Agmon, J. Phys. Chem. B **110** (9), 4434 (2006).

[139] D. Stoner-Ma, A. Jaye, P. Matousek, M. Towrie, S. Meech, and P. Tonge, Journal of the American Chemical Society **127** (9), 2864 (2005).

[140] D. Stoner-Ma, E. Melief, J. Nappa, K. Ronayne, P. Tonge, and S. Meech, J. Phys. Chem. B **110** (43), 22009 (2006).

[141] C. Fang, R. Frontiera, R. Tran, and R. A. Mathies, Nature **462** (7270), 200 (2009).

[142] M. Di Donato, L. J. G. W. van Wilderen, I. H. M. V. Stokkum, T. C. Stuart, J. T. M. Kennis, K. J. Hellingwerf, R. van Grondelle, and M. L. Groota, Phys. Chem. Chem. Phys. **13**, 16295 (2011).

[143] J. J. van Thor, C. N. Lincoln, B. Kellner, K. N. Bourdakosa, L. M. Thompson, M. J. Bearpark, P. M. Champion, and J. T. Sage, Vib. Spectrosc. **62**, 1 (2012).

[144] M. Guglielmi, I. Tavernelli, and U. Rothlisberger, Phys. Chem. Chem. Phys. **11**, 4549 (2009).

[145] K. Fukui, Acc. Chem. Res. **14**, 363 (1981).

[146] H. P. Hratchian and H. B. Schlegel, *Theory and Applications of Computational Chemistry: The First 40 Years* (C. E. Dykstra, G. Frenking, K. S. Kim, and G. Scuseria, Ed., Elsevier Science, Amsterdam, 2005), pp. 195–249.

[147] C. V. Caillie and R. D. Amos, Chem. Phys. Lett. **317**, 159 (2000).

[148] F. Yang, L. G. Moss, and G. N. P. Jr, Nature Biotechnology **14**, 1426 (1996).

[149] Y. Zhang, J. Zou, C.-C. Cheuh, H.-L. Yip, and A. K.-Y. Jen, Macromulecules **45**, 5427 (2012).

[150] Q. Zheng, B. J. Jung, J. Sun, and H. E. Katz, J. Am. Chem. Soc. **132**, 5394 (2010).

[151] J.-S. Wu, Y.-J. Cheng, M. Dubosc, C.-H. Hsieh, C.-Y. Chang, and C.-S. Hsu, Chem. Commun. **46**, 3259 (2010).

[152] C. Schwarz, H. Bässler, I. Bauer, J.-M. Koenen, E. Preis, U. Scherf, and A. Köhler, Adv. Mater. **24**, 922 (2012).

[153] J. Roncali, Macromul. Rapid Commun. **28**, 1761 (2007).

[154] Y.-X. Xu, C.-C. Chueh, H.-L. Yip, F.-Z. Ding, Y.-X. Li, C.-Z. Li, X. Li, W.-C. Chen, and A. K.-Y. Jen, Adv. Mater. **24**, 6356 (2012).

[155] J. J. Intemann, K. Yao, Y.-X. Li, H.-L. Yip, Y.-X. Xu, P.-W. Liang, C.-C. Chueh, F.-Z. Ding, X. Yang, X. Li, Y. Chen, and A. K.-Y. Jen, Adv. Func. Mater. p. Accepted Manuscript (2013).

[156] X. Zhang, H. Bronstein, A. J. Kronemeijer, J. Smith, Y. Kim, R. J. Kline, L. J. Richter, T. D. Anthopoulos, H. Sirringhaus, K. Song, M. Heeney, W. Zhang, I. McCulloch, and D. M. DeLongchamp, Nature communications **4**, Accepted Manuscript (2013).

[157] W. Liang, C. T. Chapman, and X. Li, J. Chem. Phys. **134** (18), 184102 (2011).

[158] C. Lee, W. Yang, and R. G. Parr, Phys. Rev. B **37** (2), 785 (1988).

[159] C. Adamo and V. Barone, J. Chem. Phys. **110**, 6158 (1999).

[160] G. Igel-Mann, H. Stoll, and H. Preuss, Mol. Phys. **65** (6), 1321 (1988).

[161] M. J. Frisch, G. W. Trucks, H. B. Schlegel, G. E. Scuseria, M. A. Robb, J. R. Cheeseman, G. Scalmani, V. Barone, B. Mennucci, G. A. Petersson, H. Nakatsuji, M. Caricato, X. Li, H. P. Hratchian, A. F. Izmaylov, J. Bloino, G. Zheng, J. L. Sonnenberg, W. Liang, M. Hada, M. Ehara, K. Toyota, R. Fukuda, J. Hasegawa, M. Ishida, T. Nakajima, Y. Honda, O. Kitao, H. Nakai, T. Vreven, J. J. A. Montgomery, J. E. Peralta, F. Ogliaro, M. Bearpark, J. J. Heyd, E. Brothers, K. N. Kudin, V. N. Staroverov, T. Keith, R. Kobayashi, J. Normand, K. Raghavachari, A. Rendell, J. C. Burant, S. S. Iyengar, J. Tomasi, M. Cossi, N. Rega, J. M. Millam, M. Klene, J. E. Knox, J. B. Cross, V. Bakken, C. Adamo, J. Jaramillo, R. Gomperts, R. E. Stratmann, O. Yazyev, A. J. Austin, R. Cammi, C. Pomelli, J. W. Ochterski, R. L. Martin, K. Morokuma, V. G. Zakrzewski, G. A. Voth, P. Salvador, J. J. Dannenberg, S. Dapprich, P. V. Parandekar, N. J. Mayhall, A. D. Daniels, O. Farkas, J. B. Foresman, J. V. Ortiz, J. Cioslowski, and D. J. Fox, *Gaussian Development Version Revision H.12+*. Gaussian Inc., Wallingford CT 2011.

[162] Y.-J. Cheng, S.-W. Cheng, C.-Y. Chang, W.-S. Kao, M.-H. Liao, and C.-S. Hsu, Chem. Commun. **48**, 3203 (2012).